2019

Landing-Gear Impact Response: A Non-linear Finite Element Approach

Tuan H. Tran
University of North Florida

LANDING-GEAR IMPACT RESPONSE: A NON-LINEAR FINITE ELEMENT APPROACH

by

Tuan H. Tran

A Thesis
Submitted to
The Graduated School of University of North Florida

In Partial Fulfillment of
the Requirements for the Degree of
Master of Science in Mechanical Engineering

August 2019

CERTIFICATE OF APPROVAL

The thesis “Landing-Gear Impact Response: A Non-linear Finite Element Approach” submitted by Tuan Tran in partial fulfillment of the requirements for the degree of Master of Science in Mechanical Engineering has been

Approved by the Thesis Committee: Date

_____ _____
Dr. Alexandra Schonning
Thesis Advisor (Committee Chair)

_____ _____
Dr. Jutima Simsiriwong
Committee Member

_____ _____
Dr. Stephen Stagon
Committee Member

Accepted for the School of Engineering:

_____ _____
Dr. Osama Jadaan
Director of School of Engineering

_____ _____
Dr. William Klostermeyer
Interim Dean of College of Computing, Engineering and Construction

Accepted for the University:

_____ _____
Dr. John Kantner
Dean of the Graduate School

Acknowledgments

First, I would like to express my sincere appreciation to my thesis committee. My graduate advisor, Dr. Alexandra Schonning, and my thesis committee members, Dr. Jutima Simsiriwong and Dr. Stephen Stagon, have each provided helpful feedback, encouragement, and support in the completion of this thesis.

Next, I would also like to thank my family. My wife, Tram has been especially supportive of me throughout this entire process and has made countless sacrifices to help me get to this point. I sincerely dedicate this work to her.

Last but not least, I would like to express my deepest appreciation to Team JAS Aviation for their invaluable assistance and for sharing their experiences along with all related technical data on Twin Otter aircraft. Without their support, this thesis would have never seen the light of day.

Table of Contents

List of Figures

List of Tables

Terms and Acronyms

a	Distance between Nose Landing Gear and Aircraft's Center of Gravity
A_a	Pneumatic Area
A_h	Hydraulic Area
A_o	Orifice's Opening Area
ATS	Automatic Time Step
b	Bead Seat Width
b (Figure 9 only)	Distance between Main Landing Gear and Aircraft's Center of Gravity
C_d	Coefficient of Discharge
CAR	Civil Air Regulations
CFACTOR1	Contact Compliance
CFNORM	Contact Force Vector
CFORCE	Contact Force
CFR	Code of Federal Regulations
CTDISP	Small Displacement Contact
d	Deflection under Impact
d (Figure 9 only)	Distance between Nose Landing Gear and Main Landing Gear
d_{Shock}	Shock Absorber Deflection
d_{Tire}	Tire Deflection
DTOL	Displacement/Rotation Convergence Tolerance
EPST	Friction Regularization Parameter
ETOL	Energy Convergence Tolerance
F_f	Internal Friction Load
FAA	Federal Aviation Administration
h	Free Drop Height
h_{limit}	Limit Drop Height
$h_{reserve}$	Reserve Energy Drop Height
h (Figure 6 only)	Tire Deflection
INIPENE/TZPENE	Gradual Removal of Initial Penetration
L	Wing Lift Ratio
LOADOPT	Deformation Independent Loading
n	Limit Load Factor
n (Section 4.10.1 only)	Effective Polytropic exponent
n_j	Developed Load Factor
N	Normal Force
P_h	Hydraulic Load
P_a	Pneumatic Load
q_{max}	Maximum point load
r	Inflate Radius of Tire
r (Figure 4 only)	Radius of Hole
r_b	Radius of Bead Seat
R_M	Static Ground Reaction Force at Main Landing Gear Location

R_N	Static Ground Reaction Force at Nose Landing Gear Location
RCTOL	Contact Force Convergence Tolerance
RTOL	Force/Moment Convergence Tolerance
S	Wing Area
S (Section 4.10.1 only)	Total Shock Absorber Stroke
s (Section 4.10.1 only)	Shock Absorber Axial Stroke
$\dot{s}$	Telescoping Velocity
STC	Supplemental Type Certificate
STOL	Line Search Convergence Tolerance
W	Applied Load
W_e	Effective Weight
W_o	Applied Pressure
W_L	Maximum Landing Weight
W_N	Static Reaction Load at Nose Landing Gear Location
XTCURVE	Extended Material Curve
V	Descent Velocity
V_d	Displacement Volume
V_f	Ground Reaction Force on Tire
α	Contact Patch Angle
μ	Coefficient of Friction
φ	Angle between Shock Strut Axis and Vertical Axis
η_s	Shock Absorber Efficiency Factor
η_t	Tire Absorber Efficiency Factor

Abstract

The primary objective of this research is to formulate a methodology of assessing the maximum impact loading condition that will incur onto an aircraft's landing gear system via Finite Element Analysis (FEA) and appropriately determining its corresponding structural and impact responses to minimize potential design failures during hard landing (abnormal impact) and shock absorption testing. Both static and dynamic loading condition were closely analyzed, compared, and derived through the Federal Aviation Administration's (FAA) airworthiness regulations and empirical testing data.

In this research, a nonlinear transient dynamic analysis is developed and established via NASTRAN advanced nonlinear finite element model (FEM) to simulate the worst-case loading condition. Under the appropriate loading analysis, the eye-bar and contact patch region theory were then utilized to simulate the tire and nose wheel interface more accurately. The open geometry of the nose landing gear was also optimized to minimize the effect of stress concentration. The result of this research is conformed to the FAA's regulations and bound to have an impact on the design and development of small and large aircraft's landing gear for both near and distant future.

1.0 Introduction

As one of the critical subsystems of an aircraft, landing gear detail design is usually taken up in the early aircraft design cycle due to its substantial influence on an aircraft structural configuration and long product development cycle time. The need to design nose landing gear with minimum weight, volume, extended life cycle, and short development cycle time often pose many challenges to designers.

With the advancing complexity of landing gear unit, the shock absorption tests at landing weight are required under the FAA regulations (14 CFR 23.723 or 25.723) to appropriately validate the analytical representation of the dynamic characteristics of the landing gear. A range of drop tests is usually conducted to ensure that the analytical model is adequate for all loading conditions, most specifically abnormal impact or hard landing condition. The objective of this research is to formulate a methodology of assessing the maximum impact loading condition that will incur onto an aircraft's landing gear system via FEA. By identifying the high stress and deformation areas, the results herein will help engineers and scientists in analyzing and optimizing the open geometry of the landing gear during the early designing stage. The required FAA shock absorbing testing can then be used for validation instead of trial and error, which will significantly reduce the cost and time of development.

For most small and large aircrafts, the oleo shock absorber is usually utilized as the landing gear design, due to the long operational lifetime and simple maintenance. An oleo shock absorber generally consists of a piston (inner metallic tube), which is attached to the tire and wheel by means of the fork and axle. The piston then telescopes up and down in a cylinder (outer

metallic tube), which is attached to the airframe. The cavity within the piston and cylinder is divided into two chambers and filled with air and hydraulic fluid that communicate through a small orifice. The design cushions the impacts of landing and dampens out vertical oscillations.

The original oleo shock absorber design was derived from the Vickers gun recuperative gear design and first applied to an aircraft by Breguet Aviation. The innovation behind the design, which is the recoil control by forcing hydraulic fluid through orifices, was later patented by Vickers Armstrong in 1915. Around 1934, Peter Thornhill devised a novel design of the oleo shock absorber by introducing a floating piston, which enabled the strut to work at an angle eliminating the problem of an oil and air mixture. [1]

This research will primarily focus on the analysis for the landing gear system on Viking Air Limited DHC-6 Twin Otter Aircraft, where an oleo shock absorber is utilized and incorporated. As a Short Takeoff and Landing (STOL) Aircraft, the arrangement and configuration of the landing gear system on the Twin Otter aircraft are designed to use on runways with severed conditions. With such arrangement and configuration, the analysis for the Twin Otter's landing gear system is expected to set forth as a primary example of an establishment for a comprehensive analysis methodology via FEA, where all subjected loading conditions to a landing gear design were closely analyzed and conformed to the FAA airworthiness regulations. This methodology will, in turn, validate and reinforce all future analysis of landing gears for both small and large aircraft.

Within the landing gear system of the Twin Otter aircraft, the shock strut assembly and nose wheel assembly acts as the main support for the nose installation of the aircraft (Figure 1, A1 and A2). It is an oleo-pneumatic design which contains MIL-H-5606 hydraulic fluid and air

pressure. During landing, the shock strut dampens the impact by compressing the shock strut piston within the cylinder compressing the air and fluid-filled chamber. After take-off, the piston tube extends slowly by means of the floating piston and the latch pin of the upper torque arm assembly locks into the lower fitting attached to the fuselage to keep the nose gear aligned in the FWD position during flight.

The shock strut assembly mounts to the front of the fuselage by two bolts and a lower fitting, which supports the lower portion of the strut. The nose wheel assembly and tire are then installed within the fork assembly and the hydraulic lines are attached to control the steering thus enabling the pilot to steer the aircraft during taxiing. The landing gear's suspension system can typically be grouped into two major categories, the upper interface of the shock strut assembly that connects to the fuselage (upper mass: mass that is supported by suspension system, Figure 1B) and the lower interface that connects to the wheel (lower mass: mass of the suspension system, Figure 1C).

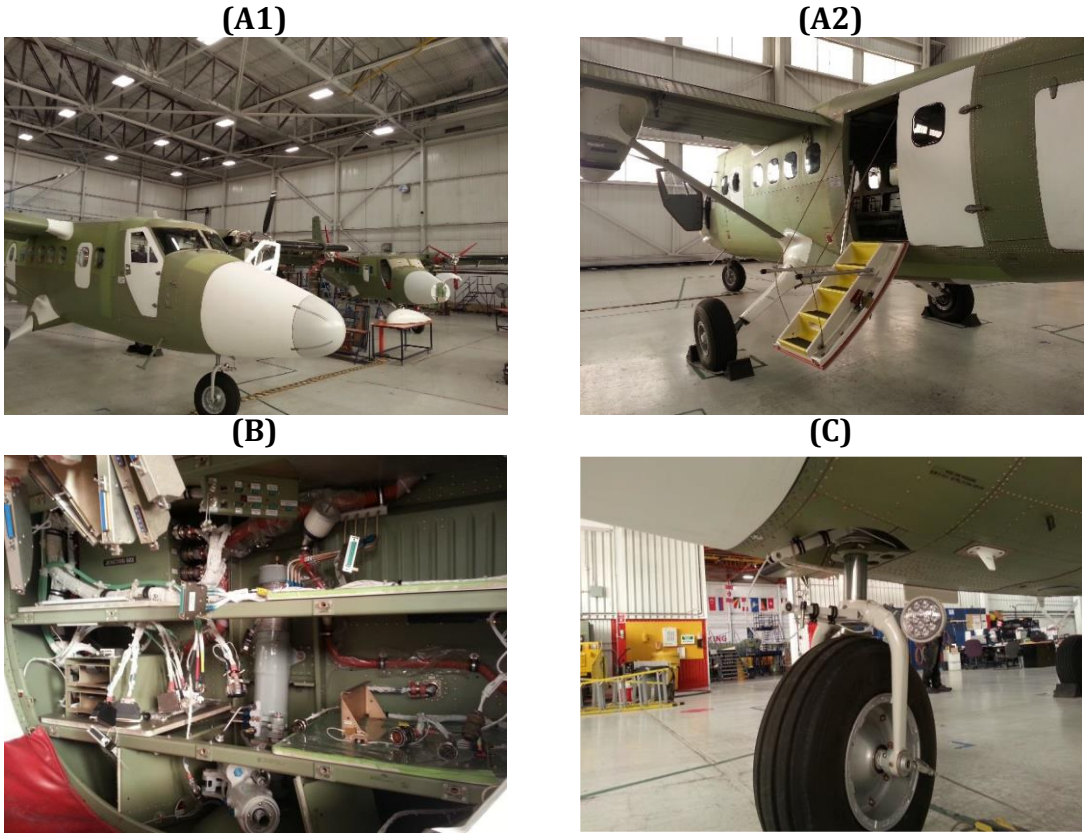

FIGURE 1: Twin Otter Aircraft Installation of Nose Gear Assembly in (A1) front and (A2) back views of aircraft nose support; (B) Sprung Weight – Upper Mass; (C) Unsprung Weight – Lower Mass

The shock strut assembly and nose wheel assembly in this research study comprise of over 140 components. However, most of these components are used during ground operation and do not have any effect on the performance of the nose gear during landing. In this simulation study, the Computer-Aided Design (CAD) model will instead focus on 14 major components, which will provide a direct load path for the ground reaction force and can be identified as a part of the shock absorbing element for the oleo landing gear system (Figure 2 and 3). Component identification, material, and function of each component are also defined in Table 1.

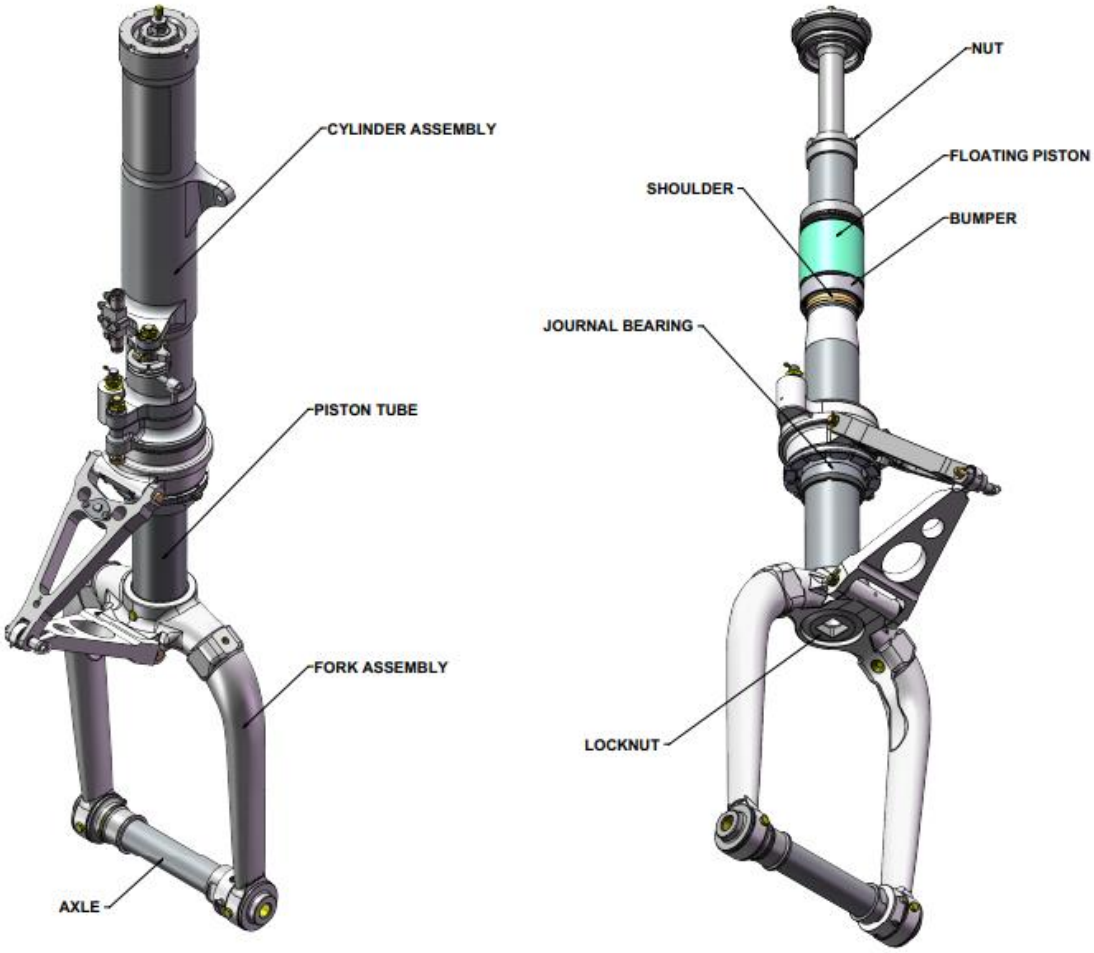

FIGURE 2: Major Shock Strut Components during Landing

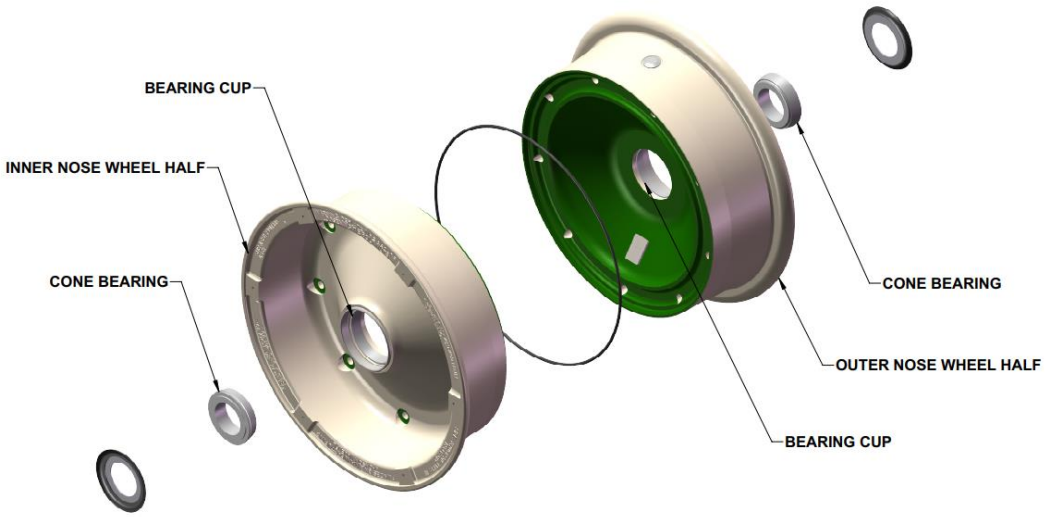

FIGURE 3: Major Nose Wheel Components during Landing

Parent Assembly	Nomenclature	Material	Function
Cylinder Assembly	Cylinder	2014-T6 Aluminum Alloy (AMS4133)	Provides the main support of the Nose Landing Gear Assembly and components. It houses all bearings and seals to allow for pressurizing the system for dampening. Externally the Cylinder provides a connection point for the Steering Actuator and Torque Arms leading to the Fork assembly, thus enabling steering.
	Sleeve	15-5PH H1075 Stainless Steel (AMS5659)	Acts as a removable lining and provides wearing and heat damage protection to the cylinder
Fork Assembly	Fork	7075-T6 Aluminum Alloy (AMS4126)	Secures the Nose Wheel Assembly (and Tire) to the Nose Landing Gear as well as provide a connection point to the Torque Arms enabling the pilot to steer the aircraft during taxiing
	Upper Bushing	Heat Treated 4340 Alloy Steel (AMS6415)	Acts as a contact surface between the Piston Tube and the Fork
	Lower Bushing	C630000-HR50 Nickel Aluminum Bronze (AMS4640)	Acts as a contact surface between the Axle and the Fork

TABLE 1: Component Identification, Material, and Function

Parent Assembly	Nomenclature	Material	Function
Bumper	Outer Ring	Heat Treated 4130 Alloy Steel (AMS6350)	Absorbs the shock of the Floating Piston inside the Cylinder housing
	Middle Ring	Heat Treated 4130 Alloy Steel (AMS6350)	
	Inner Ring	Heat Treated 4130 Alloy Steel (AMS6350)	
	Nitrile Rubber	NBR (ASTM 2000 M2BG 58 EO14)	
Nose Wheel Assembly	Outer Nose Wheel Half	AZ91C-T6 Magnesium Alloy (AMS4446)	Provides support to the Nose Landing Gear of the aircraft while on the ground and during taxiing
	Inner Nose Wheel Half	AZ91C-T6 Magnesium Alloy (AMS4446)	
	Bearing Cup	Tool Steel AISI L6 (ASTM A681)	Enable rotational movement between the Nose Wheel Assembly and the Axle
	Cone Bearing	Chrome Steel AISI E 52100 (AMS 6440)	
N/A	Piston Tube	Heat Treated 4340 Alloy Steel (AMS6415)	Acts as the main shock absorbing element for the lower mass of the Nose Gear Assembly's suspension system
	Floating Piston	7075-T73 Aluminum Alloy (AMS4617)	Provides support to the upper portion of the Nose Landing Gear. During the extended stage, the Nut rests on the Floating Piston to prevent any further extension when the aircraft is on the air. It also acts as the seal to prevent the compressed fluid from leaking.

TABLE 1 (Cont.): Component Identification, Material, and Function

Parent Assembly	Nomenclature	Material	Function
N/A	Shoulder	Heat Treated 4340 Alloy Steel (AMS6415)	Provides the surface for which the Bumper will contact to prevent further compression of the Nose Landing Gear during landing. The inside curvature of the Shoulder is contoured to match the radius of the Piston Tube to distribute the force evenly. The top of the Shoulder is flat to match the surface of the contacting Bumper
	Locknut	Heat Treated 4340 Alloy Steel (AMS6415)	Acts as the locking mechanism between the Piston Tube and the Fork Assembly
	Axle	Heat Treated 4340 Alloy Steel (AMS6415)	Provides a means to attach the Nose Wheel Assembly to the Nose Landing Gear
	Nut	7075-T6 Aluminum (AMS4126)	Provides support to the weight of the Nose Gear Assembly (except the Cylinder Assembly) while the aircraft is in the air. The bottom surface of the nut is mated with the flange inside of the Floating Piston
	Journal Bearing	304 Stainless Steel (AMS5567)	Acts as a contact surface between the Piston Tube and the Cylinder

TABLE 1 (Cont.): Component Identification, Material, and Function

2.0 Literature Review

2.1 Background

Most of the earlier work found related to this research originates from Thoai Nguyen's study on finite element analysis of the Twin Otter aircraft's original nose landing gear system [2], John C. Stearns' investigation of stress and displacement distribution in automobile wheel [3], and Benjamin Milwitzky and Francis E. Cook's report on landing gear's shock absorbing behavior [4].

In Nguyen's study, the original nose landing gear system was simplified to six major components. Static loading condition was determined and applied to the system using the eye-bar and contact patch region theories that originate from Stearns' investigation. The corresponding shock absorbing elements were then derived using similar methodology from Milwitzky and Cook's study. Finally, linear finite element analysis was performed to determine the corresponding factor of safety, static stress, and displacement distribution.

2.2 Tire and Nose Wheel Interface

Based on the previously published report of other researchers [2] [3], the tire and wheel interface has been appropriately studied and analyzed. This allows for direct analysis of the wheel without performing a nonlinear characteristic study for the tire's material and behavior.

From Stearns' investigation, the eye-bar and contact patch region theories are defined as a method to distribute the ground reaction force on to the wheel. The investigation showed a feasible correlation between the theoretical analysis and the empirical testing data. However, Stearns' report primarily focuses on the automotive wheel. Nguyen's study further expanded the applicability of this concept to the original aircraft wheel. Nguyen utilized the eye-bar and contact patch region theories that originate from Stearns to determine the pressure distribution at the contact areas of the tire bead seat and the nose wheel rim flange.

2.2.1 Eye-bar Theory

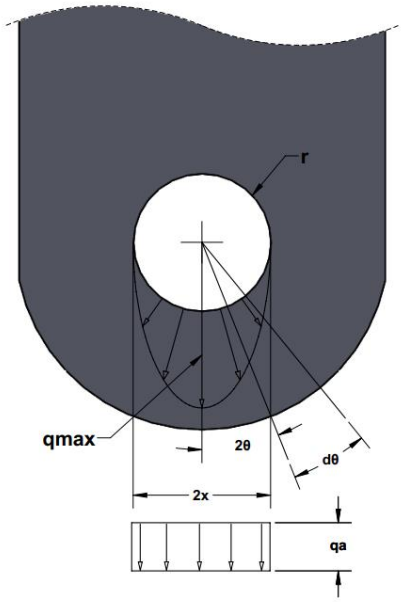

FIGURE 4: Eye-bar Loading Schematic; Adapted from Stearns [3]

Per Figure 4, the applied load W on the eye-bar can be derived as [3]

$$W = \int_0^{\frac{\pi}{2}} 2 * r * q_{max} * \cos^2 \theta * d\theta \tag{2.1}$$

Integrating and evaluating equation 2.1 yield [3]

$$W = \frac{\pi * r * q_{max}}{2} \tag{2.2}$$

With q_{max} is the maximum point load, and r is the radius of the hole. The equation 2.2 can then be applied to a tire and wheel interface per Figure 5, where the weight of the automobile is balanced with a radial load from the ground through the tire.

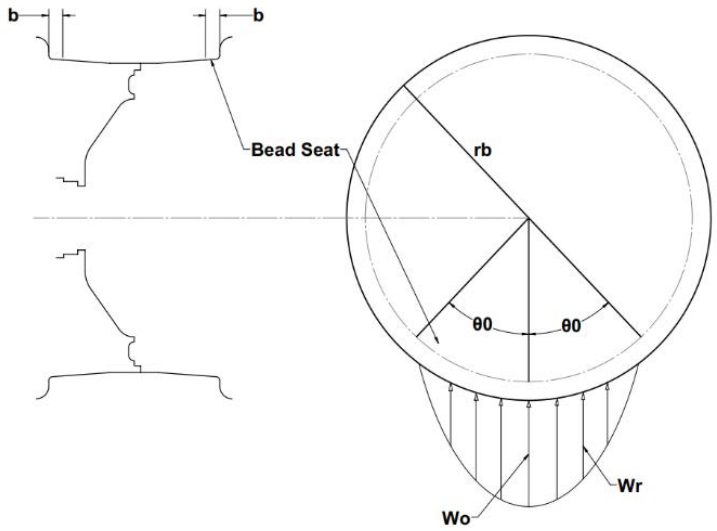

FIGURE 5: Radial Loading Schematic; Adapted from Stearns [3]

In Stearns' report, the applied pressure (W_o) can be correlated to the radial load (W) on the tire as follows [2] [3]

$$W_o = \frac{W * \pi}{b * r_b * 4 * \theta_0} \tag{2.3}$$

With b is the bead seat width, r_b is the radius of the bead seats and θ_0 is the half central angle of radial load distributions. Stearns' report also further indicated that half of the applied pressure (W_o) is applied to the rim flange, and the other half is applied to the bead seat region.

Equation 2.3 was then expanded and applied to the aircraft wheel in Nguyen's study, where the applied pressure (W_o) at the bead seat and rim flange region can then be correlated to the ground reaction force (V_f) on the tire as follows [2] [3]

$$W_o = \frac{V_f * \pi}{b * r_b * 4 * \alpha} \tag{2.4}$$

With b is the bead seat width, r_b is the radius of the bead seats and α is the contact patch angle. The applied pressure can then be evenly distributed to both half of the nose wheel.

2.2.2 Contact Patch Region Theory

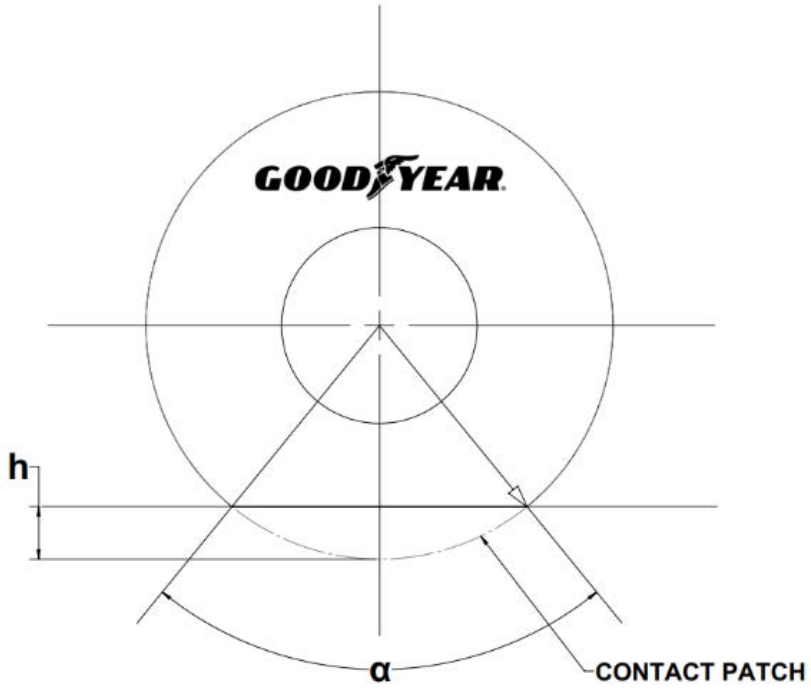

FIGURE 6: Contact Patch Region Schematic; Adapted from Stearns [3]

The contact patch region theory was implemented to derive the contact patch angle α as follows [2] [3]

$$\alpha = 2 * cos^{-1}(1 - \frac{h}{r}) \tag{2.5}$$

With h is the tire deflection, and r is the inflated radius. From the derived deflection schematic (Figure 7) of Brixius's research [5], the tire deflection can be written as a function of the inflated radius and static loaded radius. The inflated radius and static loaded radius can then be obtained from Goodyear aircraft tire databook. [6]

Refer to Section 4.9.3 for the detailed analysis of tire deflection and contact patch angle

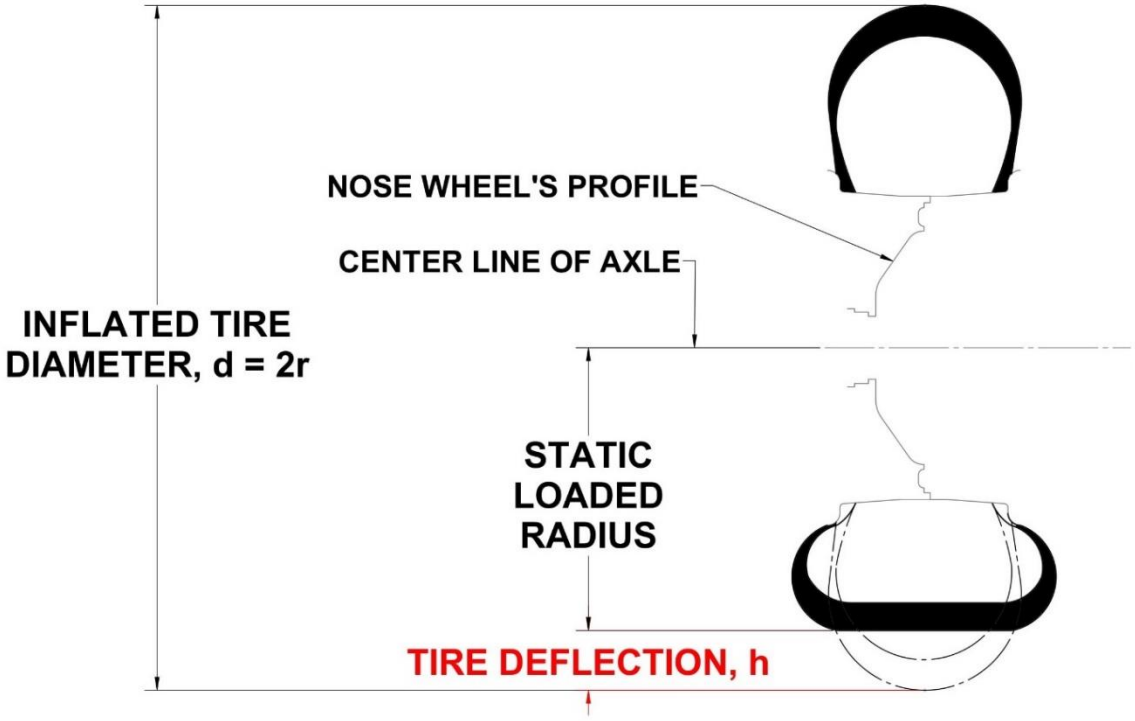

FIGURE 7: Tire Deflection Schematic; Adapted from Brixius [5]

2.3 Shock Absorption Analysis

Under CAR § 3.351 - § 3.355, all shock absorbing elements in main, nose, and tail wheel units shall be substantiated via shock absorption test. In this case, the shock absorbing elements can be identified as the 'tire' and the 'oleo' on an oleo shock absorber. These elements provide the principal means of shock absorption, hence their presence by design. Other elements of the gear such as the metallic fork can elastically deform during landing if there is sufficient offset on the loading.

Nguyen utilized the method that originates from Milwitzky and Cook's study [4] to derive and determine the applicable shock absorbing elements and their corresponding

effects onto the Twin Otter's nose landing gear system. This methodology of determining the shock absorbing forces was further elaborated and implemented in this thesis, where three major categories of shock absorbing forces (Pneumatic, Hydraulic, and Internal Friction) were appropriately identified and correlated with the empirical results in the shock absorption test at Team JAS Aviation (Appendix A). Refer to Section 4.10 for the detailed analysis of shock absorbing forces.

With the integrated design methodology in Chai and Mason's research [7], an energy absorption capability model for an oleo shock absorber was also developed in Section 4.10.1 to appropriately determine the required air volume and effective polytropic exponent to satisfy the given design states and conditions.

Per CAR § 3.245 Note (2), the maximum load factor can also be assumed to occur throughout the shock absorber stroke from 25% deflection to 100% unless demonstrated otherwise, and the load factor shall be used with whatever shock absorber extension is most critical for each element of the landing gear. For the purpose of conforming the simulation analysis to the drop testing model, the load factor gradient and shock absorber extension are established to follow the empirical results from shock absorption testing rather than the proposed methodology in CAR § 3.245 Note (2). Further details are highlighted in Section 4.8, where the load factor gradient and shock absorber extension are determined for the peak impact response of the landing gear structure.

However, it is also important to note that the established methodology in CAR § 3.245 Note (2) can be utilized for static and dynamic conditions where shock absorption

testing is not available. Section 7.0 proposes a future consideration for the continuation of research where this methodology will be utilized and validated.

2.4 Airworthiness Regulations and Requirements

Under the FAA Aircraft certification process, the studied landing gear design has been subjected to a Supplemental Type Certificate (STC) reviewing process, where the FAA validated the design's airworthiness and issued an approval of an aeronautical product's modifications with its effects to the Original Equipment Manufacturer (OEM) of the aircraft. In accordance with FAA Order 8110.42 and 14 CFR § 21.303, the basis for design approval of the STC landing gear design was based on test and computation using reversed engineering techniques and thus was designed to fit, form, and function the same as or better than the OEM counterpart.

2.4.1 Dimensional Development

To the appropriately comply with the FAA Order 8110.42 and 14 CFR § 21.303, multiple samples of each OEM component were used for dimensional analysis for each corresponding STC landing gear component. The average of the dimensions measured from each sample was used as a basis of the design. Tolerances were initially established using the minimum and maximum observed dimensions. OEM dimensions which were indicated in the OEM aircraft publications were also correlated and compared to the dimensions received from the OEM samples. Finally, a tolerance stack-up analysis was developed for each landing gear's component to ensure a proper fit for the demand of the application.

2.4.2 Materials Composition and Mechanical Properties

Previously, Nguyen utilized Curry's material guideline to assist in the design and engineering aspect of the materials selection process. This includes the inspection method and the mechanical properties of the referenced materials. [8]

In this thesis, the detailed material analysis from an accredited laboratory was instead utilized to develop the form of the landing gear's components for a more direct comparative analysis. This includes the identification of raw material, heat treatment, and coating/plating from the OEM articles. Given the demanded application of each component, the appropriate material specifications were then determined and assigned accordingly for better control over the landing gear's manufacturability. This, in term, provided a comprehensive approach to the material's determination for the FEM and appropriately complied with the FAA Order 8110.42 and 14 CFR § 21.303.

Refer to Table 1 for the detailed list of the STC landing gear components and their corresponding material specifications; Table 6 and Figure 32 for the mechanical properties for the assigned material specifications.

2.4.3 Design Function

The STC landing gear was designed as an improvement to the OEM counterpart. As discussed in Section 2.4.1 and 2.4.3, both fit and form of the OEM design were carefully and appropriately analyzed as the design basis for the STC design. Additionally, a detailed Safety Assessment of each component within the STC

design was also established for an appropriate determination of criticality level, critical features, and design aspects. Applicable design improvements were then identified and implemented accordingly. The end results are reversed engineering components that will function as good as or better than their OEM counterparts. The function of each corresponding STC components in this research are further elaborated in Table 1 and has been validated through the shock absorption test (Appendix A).

2.5 Finite Element Method

With the technological advancement in computer hardware, the utilization of FEA (Finite Element Analysis) for design and failure analysis is becoming more popular as a standard tool for engineering applications. This created a large number of engineering literature regarding the subject of FEA. The primary focus of this thesis FEA is to assess the maximum impact loading that will incur onto an aircraft's nose landing gear system and will only pertain to the relative engineering topics.

Similar to the established studies of Nguyen and Stearns [2, 3], the simulation study herein will also utilize solid elements as the discretized representation of the system's geometry. By definition, solid elements ignore all rotations and are only allowed for a three-dimensional translation (x, y, z in a cartesian coordinate). As such, usage of solid elements should usually be scrutinized due to them being computationally expensive, limited in rotational representation, and quite error prone with their complexed shape functions.

A common computational error in solid elements is due to poor aspect ratio, for example when the element is thin relative to other dimensions. The usage of solid elements in this study did not have significant aspect ratio problems. Solid elements are also known for their superiority in identifying high stress and low factor of safety areas in complex geometries, which enables the ability to make rapid design alterations during simulations prior to manufacturing and testing.

A research study was conducted by Steven Benzley, Ernest Perry, Karl Merkley, and Brett Clark to compare the accuracy of different solid elements type, most specifically between tetrahedral and hexahedral meshing [9]. From the research, the eigenvalues from the stiffness matrix of linear tetrahedrons were reported to be generally larger than those of linear hexahedrons. As such, hexahedral elements can be expected to generally deform in a lower strain energy state, thus making them more accurate than tetrahedral elements in numerous structural loading conditions. Per the research's suggestion, only quadratic solid elements are utilized in this study to help ensure numerical accuracy (Refer to Section 5.6 for further details).

As previously mentioned, both Nguyen and Stearns utilized a linear finite element model in their studies to analyze the stress and displacement distribution [2, 3]. However, to appropriately account for the reserved energy loading condition (abnormal impact), where material yielding is permitted per CAR 3.352, a nonlinear FEA is required to account for the nonlinear relationship between stress and strain. Additionally, a nonlinear geometric model is also needed to appropriately simulate the kinematic constraints and

contact behavior between the landing gear's components, where small strain and displacement are expected.

Lastly, a hyper-elasticity material model must be applied to simulate the material behavior of the bumper's nitrile rubber backing during the compression state. Based on in Hassan, Abouel-Kasem and Mahmoud evaluation [10], Ogden's material model with a fourth-term series (N = 4) was chosen to appropriately represent the constitutive behavior of nitrile rubber. From Shahzad, Kamran, Siddiqui, and Farhan research on hyperplastic material [11], the constitutive equation can be established as follows

$$\Psi = \sum_{r=1}^{N} \frac{\mu_r}{\alpha_r}\left(\lambda_1^{\alpha_r} + \lambda_2^{\alpha_r} + \lambda_3^{\alpha_r} - 3\right) + \sum_{r=1}^{N} \frac{1}{D_r}(J-1)^{2r} \tag{2.6}$$

With D_r is the bulk compressibility material constant. Due to the nature stiffness of the nitrile rubber in this research (Durometer stiffness is approximately at 50 Shore A), the material characteristic can be assumed to be incompressible without severe impact to the numerical accuracy of the study. The constitutive equation for incompressible nitrile rubber can then be simplified as

$$\Psi = \sum_{r=1}^{N} \frac{\mu_r}{\alpha_r}\left(\lambda_1^{\alpha_r} + \lambda_2^{\alpha_r} + \lambda_3^{\alpha_r} - 3\right) \tag{2.7}$$

These nonlinear areas were then derived carefully in this thesis and validated through empirical testing (Appendix A and B) to establish a finite model that practically and accurately simulates the response of the nose landing gear upon impact.

A dynamic analysis is also required to appropriately simulate the load factor gradient of the landing gear during impact or shock absorption testing as discussed in Section 2.3. However, the shock absorbing extension is set at the peak impact response configuration within the load period, or more specifically 3.89”. Refer to Section 5.1 for further details.

3.0 Airworthiness Regulations Checklist

The following checklist will highlight all FAA applicable requirements and constraints for the finite element analysis. It is not inclusive of all CAR 3 (amendment 3-1 through 3-8) and Title 14 CFR Part 23 (amendments 23-1 through 23-64) airworthiness regulations applicable to the Nose Landing Gear, only the regulations pertaining to this simulation study are included in this section [12].

CAR § 3.171 (Corollate to CFR 23.301) Loads [12]

"a) Strength requirements are specified in terms of limit and ultimate loads. Limit loads are the maximum loads anticipated in service. Ultimate loads are equal to the limit loads multiplied by the factor of safety. Unless otherwise described, loads specified are limit loads.
b) Unless otherwise provided, the specified air, ground, and water loads shall be placed in equilibrium with inertia forces, considering all items of mass in the airplane. All such loads shall be distributed in a manner conservatively approximating or closely representing actual conditions. If deflections under load would change significantly the distribution of external or internal or internal loads, such redistribution shall be taken into account.
c) Simplified structural design criteria shall be acceptable if the Administrator finds that they result in design loads not less than those prescribed in 3.181 through 3.265."

To adhear to this regulation,

a) Definitions of limit and ultimate loads are applied.

b) Specified air, ground, and water loads are placed in equilibrium with inertia forces. All loads are distributed in a manner as described to the applicable CAR 3 regulations.

c) Design loads not less than those prescribed in 3.181 through 3.265 are used.

CAR § 3.172 (Corollate to CFR 23.303) Factor of Safety [12]

"The factor of safety shall be 1.5 unless otherwise specified."

To adhear to this regulation, 1.5 will be used as a minimum factor of safety for this simulation study.

CAR § 3.173 (Corollate to CFR 23.305) Strength and Deformations [12]

"The structure shall be capable of supporting limit loads without suffering detrimental permanent deformations. At all loads up to limit loads, the deformation shall be such as not to interfere with safe operations of the airplane. The structure shall be capable of supporting ultimate loads without failure for at least 3 seconds, except that when proof of strength is demonstrated by dynamic tests simulating actual conditions of load application, the 3-second limit does not apply."

See CAR 3.352 (b) for the dynamic testing. To adhere to this regulation, no permanent deformation will be permissible for the limit load testing.

CAR § 3.174 (Corollate to CFR 23.307) Proof of Structure [12]

"Proof of compliance of the structure with the strength and deformation requirements of 3.173 shall be made for all critical loading conditions. Proof of compliance by means of structural analysis will be accepted only when the structure conforms with types for which experience has shown such methods to be reliable. In all other cases substantiating load tests are required. Dynamic tests including structural flight tests shall be acceptable, provided that it is demonstrated that the design load conditions have been simulated. In all cases certain portions of the structure must be subjected to tests as specified in Subpart D of this part."

Proof of compliance for strength and deformation is demonstrated by experimental test in Section 4.7. The empirical result were re-evaluated through finite element analysis, as described in Section 6.0.

CAR § 3.241 (Corollate to CFR 23.471) Ground Loads [12]

"The loads specified in the following conditions shall be considered as the external loads and the inertia forces which occur in an airplane structure. In each of the ground load conditions specified the external reaction shall be placed in equilibrium with the linear and angular inertia forces in a rational or conservative manner."

The loads specified in the following conditions shall be considered as the external loads and the inertia forces which occur in an airplane structure. In each of the ground load conditions, the specified reaction shall be placed in equilibrium in a conservative manner.

CAR § 3.242 (Corollate to CFR 23.473) Design Weight [12]

"The design landing weight shall not be less than the maximum weight for which the airplane is to be certificated, except as provided in paragraph (a) or (b) of this section.
(a) A design landing weight equal to not less than 95 percent of the maximum weight shall be acceptable if it is demonstrated that the structural limit load values at the maximum weight are not exceeded when the airplane is operated over terrain having the degree of roughness to be expected in service at all speeds up to the take-off speed. In addition, the following shall apply."

To adhere to this regulation, the maximum certified design weights will be used for this simulation study.

CAR § 3.243 (Corollate to CFR 23.473) Load Factor for Landing Conditions [12]

"In the following landing conditions, the limit vertical inertia load factor at the center of gravity of the airplane shall be chosen by the designer but shall not be less than the value

which would be obtained when landing the airplane with a descent velocity, in feet per second, equal to the following value:

$$V = 4.4 * \left(\frac{W}{S}\right)^{\frac{1}{4}}$$

Except that the descent velocity need not exceed 10 feet per second and shall not be less than 7 feet per second. Wing lift not exceeding two-thirds of the weight of the airplane may be assumed to exist throughout the landing impact and may be assumed to act through the airplane center of gravity. When such wing lift is assumed the ground reaction load factor may be taken equal to the inertia load factor minus the ratio of the assumed wing lift to the airplane weight. In no case, however, shall the inertia load factor used for design purposes be less than 2.67, nor shall the limit ground reaction load factor be less than 2.0, unless it is demonstrated that lower values of limit load factor will not be exceeded in taxying the airplane over terrain having the maximum degree of roughness to be expected under intended service use at all speeds up to take-off speed."

To adhere to this regulation, a minimum inertia load factor of 2.67 is used for this simulation study

CAR § 3.244 (Corollate to CFR 23.477) Landing Cases and Attitudes [12]

"For conventional arrangements of main and nose, or main and tail wheels, the airplane shall be assumed to contact the ground at the specified limit vertical velocity in the attitudes described in 3.245-3.247."

Airplane shall be assumed to contact the ground at the specified limit vertical velocity in the attitudes described in CAR 3.245-3.247.

CAR § 3.245 (Corollate to CFR 23.479) Level Landing [12]

"(b) Nose Wheel Type. Two cases shall be considered:

1) Nose and main wheels contacting the ground simultaneously

2) Main wheels contacting the ground, nose wheel just clear of the ground.

(c) Drag Components. In this condition, drag components simulating the forces required to accelerate the tires and wheels up to the landing speed shall be properly combined with the corresponding instantaneous vertical ground reactions. The wheel spin-up drag loads may be based on vertical ground reactions, assuming wing lift and a tire-sliding coefficient of friction of 0.8, but in any case, the drag loads shall not be less than 25 percent of the maximum vertical ground reactions neglecting wing lift."

Both cases are considered; see Section 4.1 for load analysis.

CAR § 3.253 (Corollate to CFR 23.499) Supplementary Conditions for Nose Wheels [12]

"The conditions set forth in 3.254-3.256 apply to nose wheels and affected supporting structure. The shock absorbers and tires shall be assumed deflected to their static positions."

Conditions set forth in 3.254-3.256 apply to nose wheels and affected supporting structure. See Sections 4.1.3 in this document.

CAR § 3.254 (Corollate to CFR 23.499) Aft Load [12]

"Limit force components at axle:
Vertical, 2.25 times static load on wheel,
Drag, 0.8 times vertical load."

Condition is considered for load analysis. See Sections 4.1.3 in this document.

CAR § 3.255 (Corollate to CFR 23.499) Forward Load [12]

"Limit force components at axle:
Vertical, 2.25 times static load on wheel,
Forward, 0.4 times vertical load."

Condition is considered for load analysis. See Sections 4.1.3 in this document.

CAR § 3.256 (Corollate to CFR 23.499) Side Load [12]

"Limit force components at ground contact:
Vertical, 2.25 times static load on wheel,
Side, 0.7 times vertical load."

Condition is considered for load analysis. See Sections 4.1.3 in this document.

CAR § 3.352 (Corollate to CFR 23.723) Shock Absorption Tests [12]

"a) It shall be demonstrated by energy absorption tests that the limit load factors selected for design in accordance with 3.243 will not be exceeded in landings with the limit descent velocity specified in that section.
b) In addition, a reserve of energy absorption shall be demonstrated by a test in which the descent velocity is at least 1.2 times the limit descent velocity. In this test there shall be no failure of the shock absorbing unit, although yielding of the unit will be permitted. Wing lift equal to the weight of the airplane may be assumed for purposes of this test."

The chosen limit load factors selected for design in accordance with CAR 3.243 will not be exceeded in landings. See CAR 3.355 below for compliance with section (b) by means of reserve energy absorption drop tests.

CAR § 3.353 (Corollate to CFR 23.725) Limit Drop Tests [12]

"(a) Compliance with the specified limit landing conditions will be demonstrated by simulation study. This will be conducted on units consisting of wheel, tire, and shock absorber in their proper relations, from free drop heights not less than:

$$\boldsymbol{h = 3.6 * \left(\frac{W}{S}\right)^{\frac{1}{2}} in}$$

(b) In simulating the permissible wing lift in free drop tests, the landing gear unit shall be dropped with an effective weight equal to:

$$W_e = W_N * \left(\frac{h + (1 - L) * d}{h + d}\right)$$

W = W_N for nose wheel units, and shall be equal to the static reaction which will exist at the nose wheel when the mass of the airplane is concentrated at the center of gravity and exerts a force of 1.0g downward and 0.33g forward."

Both requirements are applicable to the simulation study. See Sections 4.4, 4.5, 4.6, and 4.7 in this document.

CAR § 3.354 (Corollate to CFR 23.725) Limit Load Factor Determination [12]

"In determining the limit airplane inertia load factor n from the free drop tests described above, the following formula shall be used:

$$n = n_j * \left(\frac{W_e}{W}\right) + L$$

nj = the developed load factor during drop test

The value of *n* so determined shall not be greater than the limit inertia load factor used in the landing conditions CAR 3.243."

In determining the airplane inertia load factor n for the simulation study, the following formula shall be used:

$$n = n_j * \left(\frac{W_e}{W_N}\right) + L$$

CAR § 3.355 (Corollate to CFR 23.727) Reserve Energy Absorption Drop Tests [12]

"If compliance with the reserve energy absorption condition specified in 3.352 (b) is demonstrated by free drop tests, the drop height shall be not less than 1.44 times the drop height specified in 3.353. In simulating wing lift equal to the airplane weight, the units shall be dropped with an effective mass equal to:

$$W_e = W \frac{h}{h + d}$$

where the symbols and other details are the same as in 3.353”

Condition is considered for load analysis. See Sections 4.4, 4.5, 4.6, and 4.7 in this document.

4.0 Load Determination

The following section will derive the loads and conditions considered for the simulation study. The comprehensive methodology of analysis provided herein should be reproducible and applicable to all oleo landing gear systems for both small and large aircrafts.

4.1 Gear Static Loads

The following aircraft specific information is provided in the Type Certificate Data Sheet (TCDS #A9EA) and the aircraft Ground Support Manual (PSM 1-6-2T). For the purposes of this analysis, the weight and balance conditions for the DHC-6-400 series aircraft will be used as it has the highest maximum weights [13]. From the provided data, the landing gear stations (Figure 8) and maximum landing weights (Figure 9) can be determined.

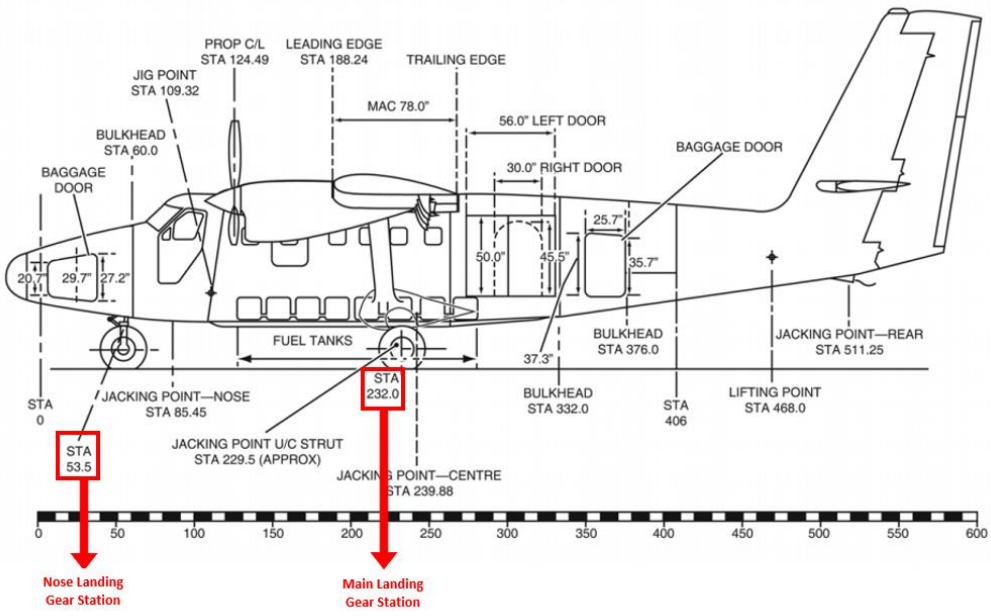

FIGURE 8: Location of Landing Gears [14]

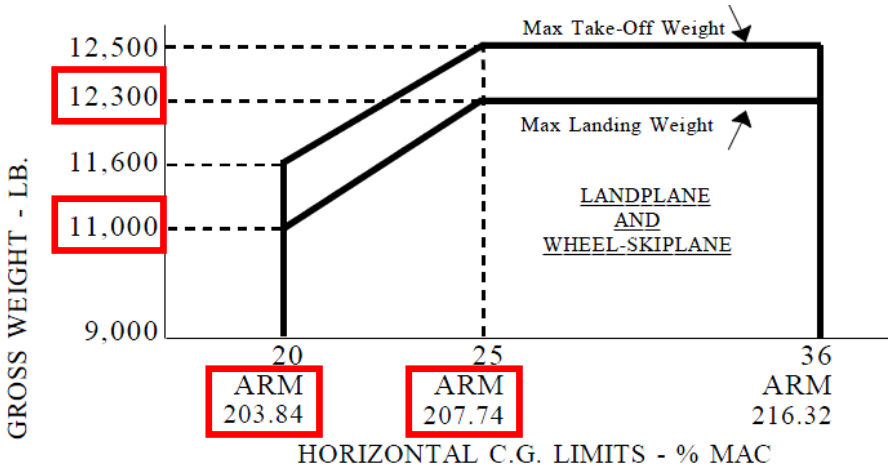

FIGURE 9: C.G. Range with Fixed Landing Gear [13]

Maximum Landing Weights:

$$W_L = 12{,}300\ lbs\ at\ station\ 207.74$$

$$W_L = 11{,}000\ lbs\ at\ station\ 203.84$$

With the given wing area in the Aircraft Weight and Balance Manual, the wing loadings at landing can also be approximated from the maximum landing weights.

Wing Area:

$$S = 420\ ft^2\ [14]$$

Wing Loadings at Landing:

C.G. Station 203. 84: $\frac{W_L}{S} = \frac{11000}{420} = 26.2\ lb/ft^2$ (4.1)

C.G. Station 207.74: $\frac{W_L}{S} = \frac{12300}{420} = 29.3\ lb/ft^2$ (4.2)

The static reaction loads on nose landing gear from each applicable landing cases per CAR § 3.245 can then be assessed as shown in Section 4.1.1 and 4.1.2.

4.1.1 Vertical Static Condition:

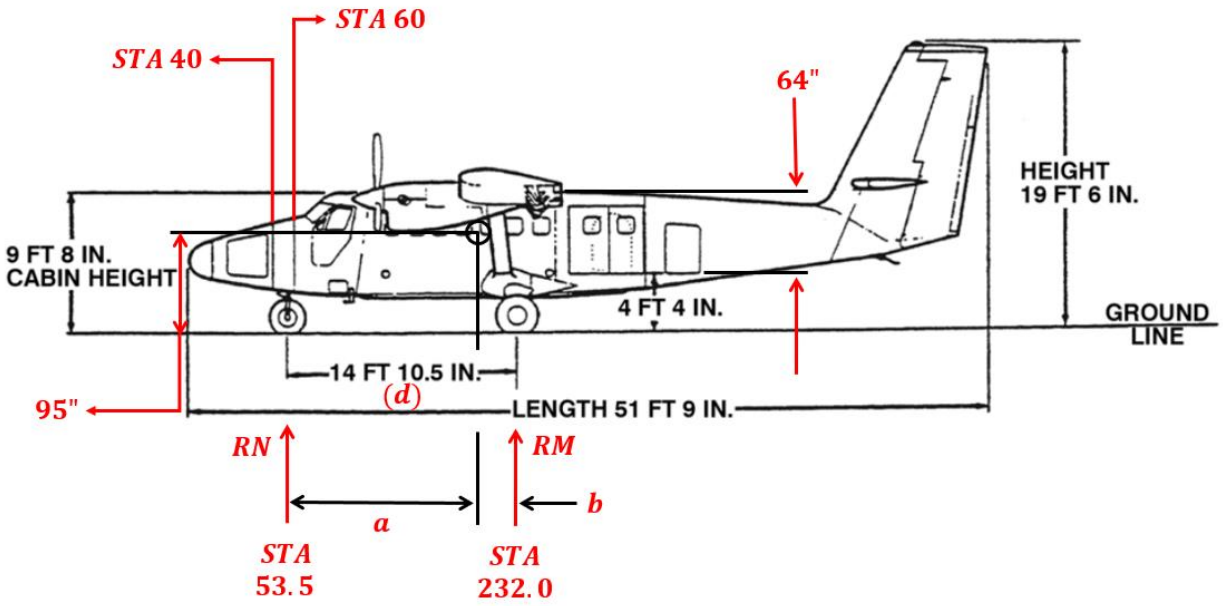

FIGURE 10: Level Landing with Vertical Reactions [12, 14]

A Free Body Diagram (FBD) can be established with R_N and R_M as the ground reaction loads at the nose and main gear stations as shown in Figure 10.

Mid C.G. at Sta 207.74: $W_L = 12{,}300\ lbs$

a = 154.24 in b = 24.26 in d = 178.5 in

$$R_N = \frac{W_L * b}{d} = \frac{12300 * 24.26}{178.5} = 1{,}672\ lbs \quad (4.3)$$

$$R_M = W_L - R_N = 12300 - 1672 = 10{,}628\ lbs \quad (4.4)$$

Forward C.G. at Sta 203.84: $W_L = 11{,}000\ lbs$

a = 150.34 in b = 28.16 in d = 178.5 in

$$R_N = \frac{W_L * b}{d} = \frac{11000 * 28.16}{178.5} = 1{,}735\ lbs \quad (4.5)$$

$$R_M = W_L - R_N = 11000 - 1735 = 9{,}265\ lbs \quad (4.6)$$

4.1.2 Combined Static Condition:

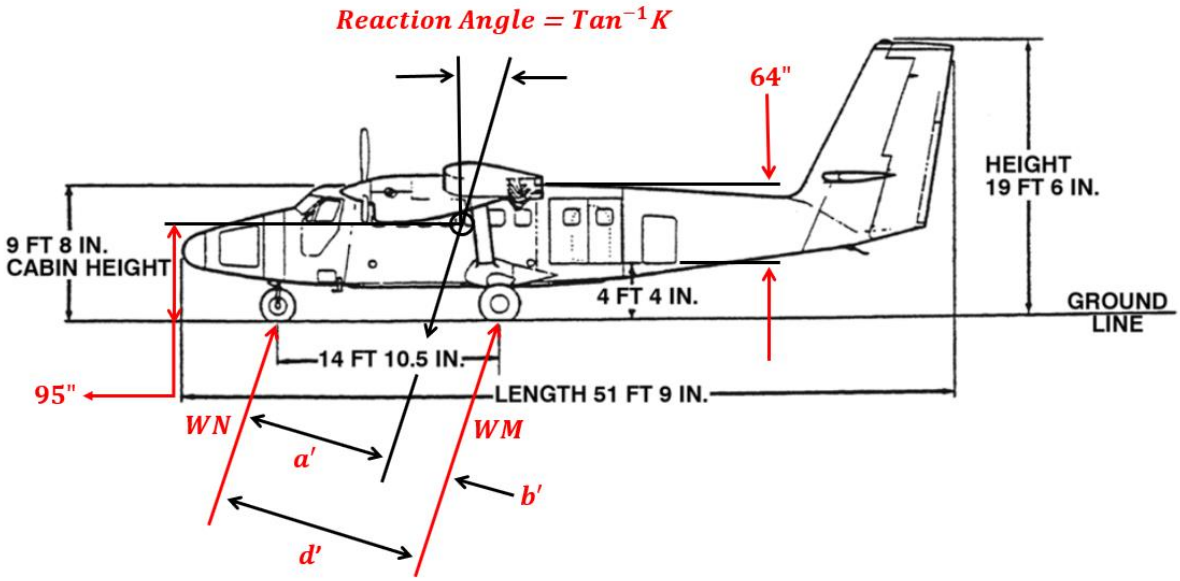

FIGURE 11: Level Landing with Inclined Reactions [12, 14]

The correction (W_N) of nose gear reaction load (R_N) are determined for the combined condition with a 0.33g forward load factor per CAR § 3.353 (b) and K = 0.33 for W_L ≥ 6000 lbs per CAR § 3.245 (b) (1) Note 1. The angle of the reaction is $Tan^{-1}(.33) = 18.3°$,

$$W_N = \frac{R_N}{cos(18.3)} = \frac{R_N}{.949} \tag{4.7}$$

Mid C.G. at Sta 207.74: $W_L =$ 12,300 lbs

$R_N =$ 1,672 lbs

$W_N = \frac{1672}{.949} =$ 1,762 lbs

Forward C.G. at Sta 203.84: $W_L =$ 11,000 lbs

$R_N =$ 1,735 lbs

$W_N = \frac{1735}{.949} =$ 1,828 lbs

4.1.3 Reaction Loads:

The highest reaction load on the nose landing gear occurs when assuming inclined reactions (CAR § 3.353) with 11,000 lbs landing weight at the forward C.G. Sta 203.84. Per CAR § 3.253, the below conditions shall be applied to the nose wheel and affected the supporting structure.

Aft Load per CAR § 3.254:
Vertical: 1828lbs x 2.25 = 4113 lbs; Drag: 4113lbs x 0.8 = 3290.4 lbs.

Forward Load per CAR § 3.255:
Vertical: 1828lbs x 2.25 = 4113 lbs; Forward: 4113lbs x 0.4 = 1645.2 lbs.

Side Load per CAR § 3.256:
Vertical: 1828lbs x 2.25 = 4113 lbs; Side: 4113lbs x 0.7 = 2879.1 lbs.

4.2 Descent Velocity

Per CAR § 3.243, the load factor to be compared shall not be less than the value which would be obtained when landing the aircraft with a descent velocity equal to:

$$v = 4.4 * \left(\frac{W_L}{S}\right)^{\frac{1}{4}} \tag{4.8}$$

Except that it need not exceed 10 feet per second.

Forward C.G.: $\frac{W}{S} = 26.2\ lb/ft^2$

$$v = 4.4 * (26.2)^{\frac{1}{4}} = 9.95\ ft/s$$

Mid C.G.: $\frac{W}{S} = 29.3\ lb/ft^2$

$$v = 4.4 * (29.3)^{\frac{1}{4}} = \ 10.2\ ft/s$$

Since descent velocity need not exceed 10 feet per second (CAR 3.243), $v = 10\ ft/s$

4.3 Minimum Design Load Factor

In aerospace application, the load factor or limit load factor is usually referring to the ratio of a specified load to the total weight of the aircraft. In this research, it is used to represent the overall ground reaction load to which the structure of the aircraft, more specifically the nose portion of the aircraft and the supporting interface (landing gears), is subjected.

Per CAR § 3.243, the inertia load factor for design purposes shall not be less than 2.67 g's. The minimum design load factor can then be theoretically determined to be 4.01 g's by considering for the factor of safety at 1.5 (Ultimate load factor, refer to CAR 3.172).

4.4 Limit Drop Height

The limit drop height will be specified as follows per CAR § 3.353:

$$h = 3.6 * \left(\frac{W_L}{S}\right)^{\frac{1}{2}} in \tag{4.9}$$

However, the free drop height (h) may not be less than 9.2 inches and need not be more than 18.7 inches.

$$h = 3.6 * (29.3)^{\frac{1}{2}} = \ 19.5 \ in$$

Since limit drop height need not exceed 18.7 in, $h_{limit} = 18.7 \ in$

4.5 Reserve Energy Drop Height

The reserve energy drop height is specified as follows per CAR § 3.355:

$$h_{reserve} = 1.44 * h_{limit} = 1.44 * 18.7 = 26.9 \ in \tag{4.10}$$

4.6 Effective Weight

For the limit load absorption, the effective weight per CAR § 3.353(b) is equal to:

$$W_e = W_N * \left(\frac{h + (1 - L) * d}{h + d} \right) \tag{4.11}$$

Where:

$W_e =$ The effective weight to be used in the simulation

$h =$ Specified height of drop in inches

$d =$ Deflection under the impact of the tire plus the vertical component of the axle travel relative to the drop mass. The value of *d* used in the computation of W_e shall not exceed the obtained value in the drop tests.

$W_N =$ Shall be equal to the static reaction which will exist at the nose wheel when the mass of the airplane is concentrated at the center of gravity and exerts a force of 1.0*g* downward and .33*g* forward.

$L =$ The ratio of assumed wing lift to airplane weight, not greater than 0.667.

$\eta_s =$ Shock absorber efficiency factor = 0.80

$\eta_t =$ Tire absorber efficiency factor = 0.75

h = 18.7 in per CAR 3.353(a) and Section 4.4

d = 13.11 in to be confirmed/adjusted prior to limit drop test, see equation 4.12

$W_N = 1828$ lbs per CAR 3.245 (combined loading) & L = 0.667 (Assumed)

Deflection of the tire and shock strut under limit load can be taken as:

$$d_{Tire} = \eta_t * (Inflated\ radius\ [6] - flat\ radius\ [6])$$

$$= 0.75 * (13.75\ in - 8\ in\ ) = \ 4.31\ in$$

$$d_{Shock} = \eta_s * (Total\ deflection\ of\ shock) = 0.80 * 11\ in = 8.8\ in$$

A preliminary estimation of the total deflection and effective weight can then be calculated as follows:

$$d_{Total} = \ d_{Tire} + \ d_{Shock} = 4.31\ in + 8.8\ in = 13.11\ in \qquad (4.12)$$

$$W_e = (1828\ lbs) * \frac{18.7\ in + (1 - .667) * 13.11\ in}{18.7\ in + 13.11\ in} = 1326\ lbs$$

However, this is just a preliminary estimation under limit loading. A series of pre-drop tests was conducted to adjust the preliminary estimates of d and W_e (Refer to Section 4.7 for readjustment). After d has been found, an initial value for W_e may be calculated using equation 4.11.

For reserve energy absorption, the preliminary estimation of effective weight per CAR § 3.355 is equal to:

$$W_e = W_N * \frac{h}{h + d} \qquad (4.13)$$

$$W_e = (1828\ lbs) * \frac{26.9\ in}{26.9\ in + 13.11\ in} = \ 1229\ lbs$$

CAR 3 Regulation	Description	Parameter
3.352 (a)	Minimum Design Load Factor	n_{min} = 4.01 (See CAR 3.243 and Section 4.3)
3.352 (b)	Reserve of Energy Absorption Descent Velocity	Limit Descent Velocity: V = 10 ft/s Limit x 1.2 = 12 ft/s
3.353 (a)	Free Drop Height	h = 18.7 in
3.353 (b)	Effective Mass	W_e = 1326 lbs
3.355	Free Drop Height (Reserve Energy Absorption)	h = 26.9 in
3.355	Effective Mass (Reserve Energy Absorption)	W_e = 1229 lbs

TABLE 2: Summary of Regulations and Preliminary Estimations for Dynamic Load

4.7 Corrections from Empirical Testing Data

Test Number	Description	Required Minimum Load Based on Calculations (lbs)	Readjustment Based on Empirical Testing Data (lbs)	Results
1	Static Load Test – Vertical and Fwd Load	4113 Vertical 1645 Fwd	4190 Vertical 1676 Fwd	No permanent set during a loading period of 5s
2	Static Load Test – Vertical and Side Load	4113 Vertical 2879 Side	4216 Vertical 2951 Side	No permanent set during a loading period of 5s
3	Static Load Test – Vertical and Drag Load	4113 Vertical 3290 Drag	4209 Vertical 3367 Drag	No permanent set during a loading period of 5s
4	Limit Dynamic Drop Test – 18.7” Vertical Drop	1326 Effective Mass w/ the deflection of 13.11”	1486 Effective Mass w/ the deflection of 8.95”	No permanent set with n_{jmax} = 4.04 g's
5	Reserve Energy Dynamic Drop Test – 26.9” Vertical Drop	1229 Effective Mass	1376 Effective Mass	No catastrophic failure with n_{jmax} = 5.29 g's

TABLE 3: Results and Readjustments from Empirical Testing (Appendix A)

Free drop tests were performed to show compliance with the free drop height and corresponding effective weight for each testing condition (see CAR § 3.353 and § 3.355). The free drop test fixture (Figure 11A) consists of a drop carriage (mounting location of nose gear sample), which is freely moving in the vertical direction with respect to the drop frame (station to the ground). A 48" position transducer was then mounted between the drop frame and carriage to record the carriage distance from the prescribed height of drop test (refer to Section 4.4 and 4.5). An accelerometer was also mounted to the side of the drop carriage to record the acceleration (load factor).

All resulted data for dynamic drop tests is recorded at 1000 samples per second as seen in Figure 11B. The reported acceleration is measured in g's unit and represented as the magenta data points while the reported carriage displacement is measured in inches and represented with the blue data points. With the maximum reported load factor during the dynamic drop tests, the limit load factor of each respective loading condition per CAR § 3.354 can be derived as:

Limit Drop Condition:

$$n = n_{jmax} * \left(\frac{W_e}{W_N}\right) + L = 4.04 * \left(\frac{1486}{1828}\right) + 0.667 = 3.95 \text{ g's}$$

Reserve Energy Condition:

$$n = n_{jmax} * \left(\frac{W_e}{W_N}\right) + L = 5.29 * \left(\frac{1376}{1828}\right) + 1 = 4.98 \text{ g's}$$

The resulted load factors also indicate a negligible difference (9%) in theoretical determination ($n_{theoratical\ min}$ = 4.01) and empirical testing ($n_{empirical\ min}$ = 3.95) for the limit drop condition. This further validates the design consideration in Section 4.3.

(A)

FIGURE 12: (A) Free Drop Test Fixture
(B) Impact Response Graphs from Empirical Testing (Appendix A)

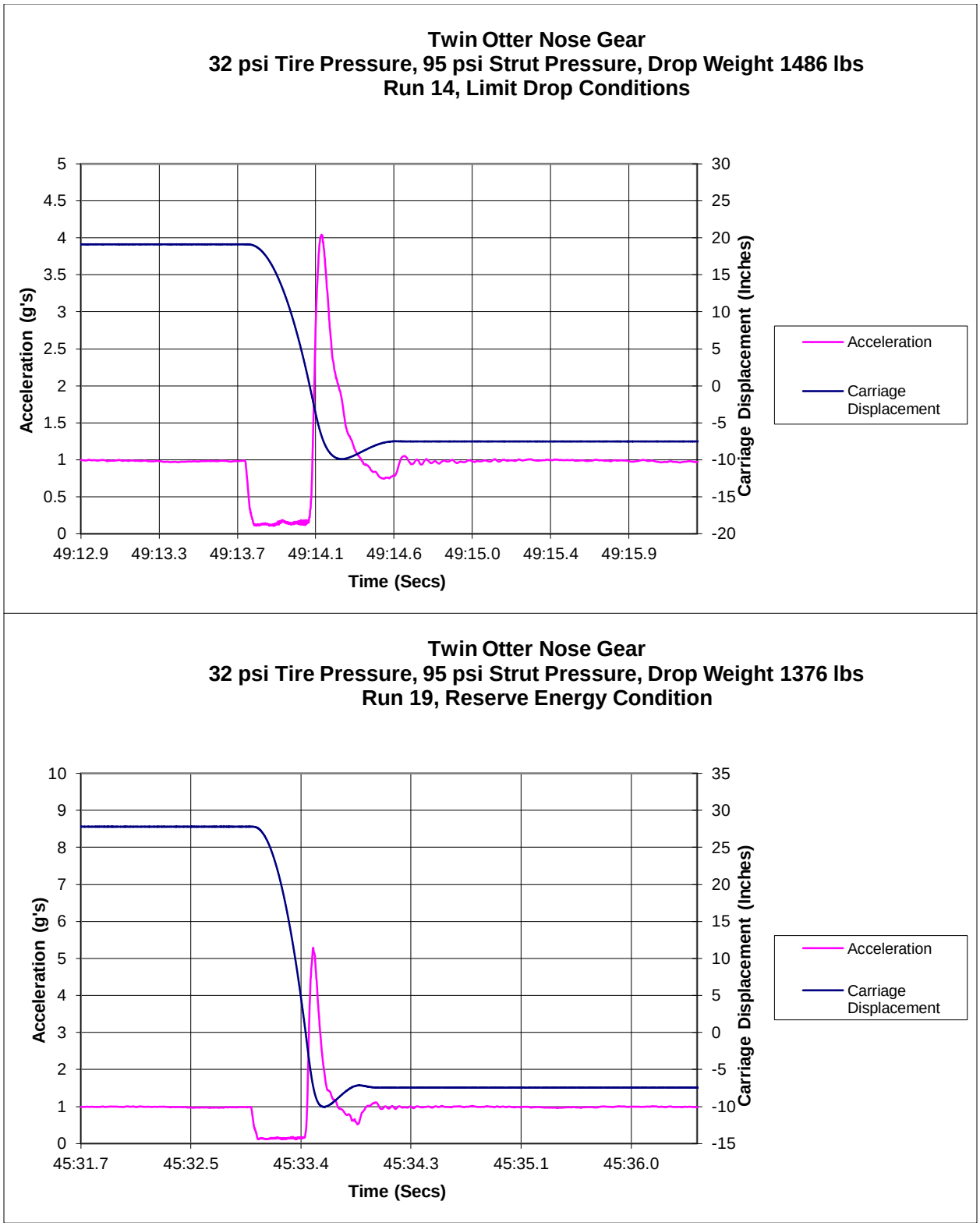

(B)

FIGURE 12 (Cont.): (A) Free Drop Test Fixture
(B) Impact Response Graphs from Empirical Testing (Appendix A)

4.8 Gear Dynamic Loads

When a large force applied to a system for a short time interval, it is often referred to as shock or impact. This shock or impact can produce correspondingly large accelerations, which can be related through Newton's second law:

$$F = m * a \tag{4.14}$$

Where:

F = The force applied to the system

m = Mass of the system

a = Acceleration of the system

By incorporating Newton's third law with Equation 4.14, the vertical ground reaction can then be derived as a function of the effective weight and the limit load factor as follows:

$$V_f = W_e * n \tag{4.15}$$

Where:

V_f = Ground reaction force on the tire

W_e = The effective weight

n = The limit load factor

Based on the empirical results in Section 4.7, the limit load factors (accelerations) were converted from the reported load factors and defined as a function of time. With a constant effective weight (mass), the vertical force of impact can also be derived as such.

Since the focus of this simulation study is about the peak response of the nose

landing gear structure upon shock or impact, a section of each respective graph in Section 4.7 was extracted for analyzing. All oscillated movements of the load factor's amplitude after the initial ramp-up period is then gradually decreased from the initial peak response (Figure 12B), hence the principal mean of shock absorption by design. Each section details the corresponding vertical forces and the inertia load factors at the peak impact response (Figure 13 and Figure 14).

Limit Drop Condition (68ms period):

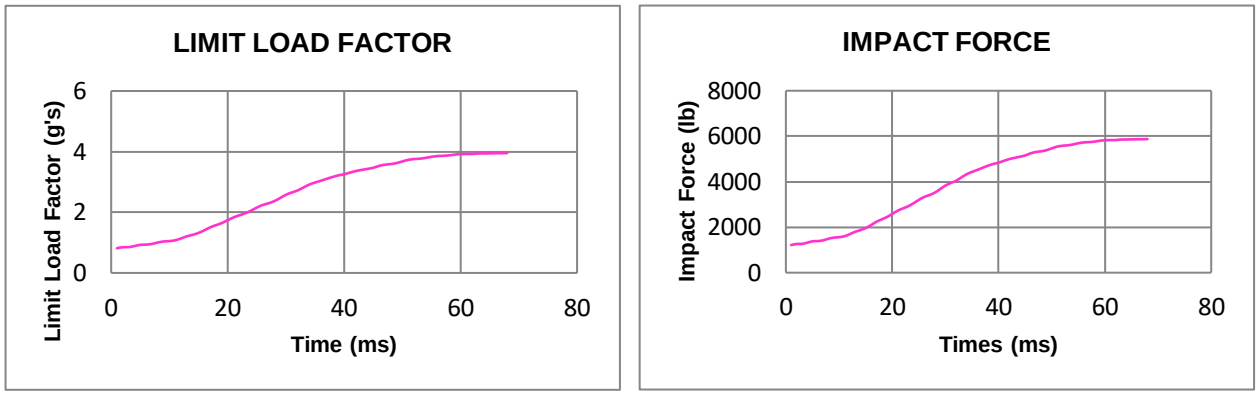

FIGURE 13: Peak Impact Response in Limit Drop Condition

Reserve Energy Condition (60ms period):

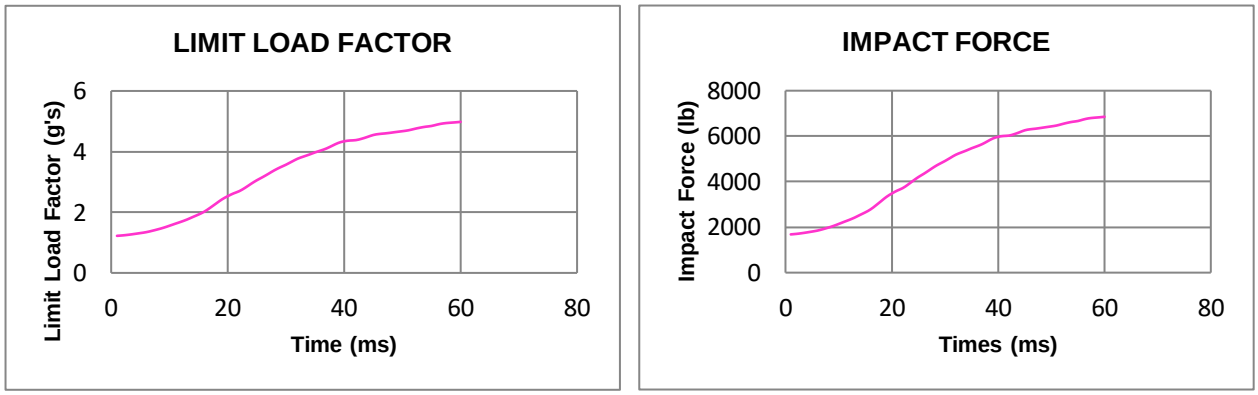

FIGURE 14: Peak Impact Response in Reserve Energy Condition

4.9 Loading Conditions

In this section, two primary loading conditions (static and dynamic) can then be

summarized and assessed for the simulation study as follows

4.9.1 Static Loading Condition:

Based on Sections 4.1, three different static loading conditions were applied to the nose gear and held constant for a period of 5s.

a) Aft Load:

- Vertical: 4209 lbs.
- Drag: 3367.2 lbs.
- Resultant: 5390.15 lbs.

b) Forward Load:

- Vertical: 4190 lbs.
- Forward: 1676 lbs.
- Resultant: 4512.77 lbs.

c) Side Load:

- Vertical: 4216 lbs.
- Side: 2951.2 lbs.
- Resultant: 5146.28 lbs.

4.9.2 Dynamic Loading Condition:

Based on Sections 4.7 and 4.8, two different dynamic loading conditions (limit drop and reserve energy) were applied to the nose gear within their respective loading period.

a) Estimated Limit Drop Condition

IAW Regulations (Refer to Table 2):

- Peak Limit Load Factor: 4.01 g's.
- Peak Vertical Impact Force: 5317.26 lbs.

b) Limit Drop Condition IAW Testing (68ms period – Refer to Figure 13):

- Peak Limit Load Factor: 3.95 g's.
- Peak Vertical Impact Force: 5874.8 lbs.

c) Reserve Energy Condition IAW Testing (60ms period – Refer to Figure 14):

- Peak Limit Load Factor: 4.98 g's.
- Peak Vertical Impact Force: 6853.7 lbs.

4.9.3 Loading Region:

Based on the contact patch region theory, the contact patch angle is derived using equation 2.4.

$$\alpha = 2 * cos^{-1}(1 - \frac{h}{r})$$

Where:

$\alpha =$ Contact patch angle

$h =$ Tire deflection

$r =$ Inflated radius

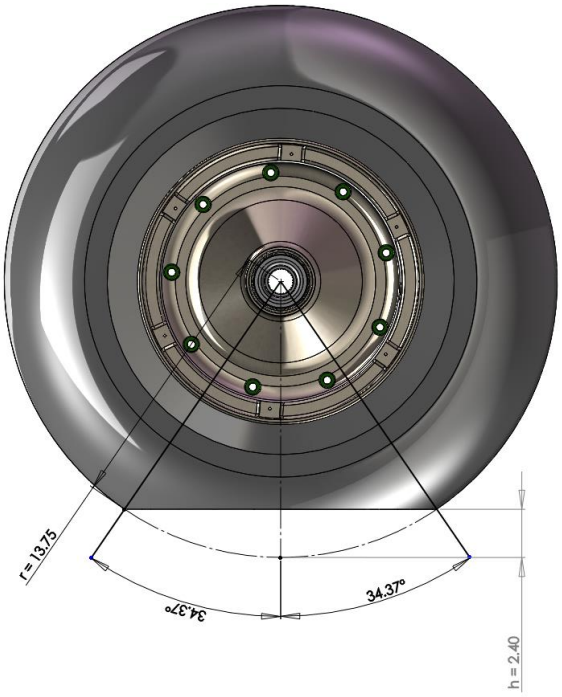

FIGURE 15: Contact Patch Region

With $Tire\ deflection = Inflated\ radius\ [6] - Static\ loaded\ radius\ [6]$ (4.16)

$$\text{or } h = 13.75" - 11.35" = 2.4"$$

$$\alpha = 2 * cos^{-1}\left(1 - \frac{h}{r}\right) = 2 * cos^{-1}\left(1 - \frac{2.4}{13.75}\right) = 68.73°$$

The bead seat and rim flange region of the nose wheel that will experience the highest-pressure during impact can then be determined based on the calculated contact patch angle as shown in Figure 15.

The center line of the central angle was set to be parallel with the cylinder mounting plane to realistically simulate the alignment of the shock strut assembly to the fuselage (Figure 16). The angle φ was then determined to be 7.18°.

From the fully extended extension of 11.24”, the piston extension was then derived using equation 4.17.

$$piston\ extension = 11.24" - \frac{|carriage\ displacement\ (Figure\ 10)|}{\varphi} \quad (4.17)$$

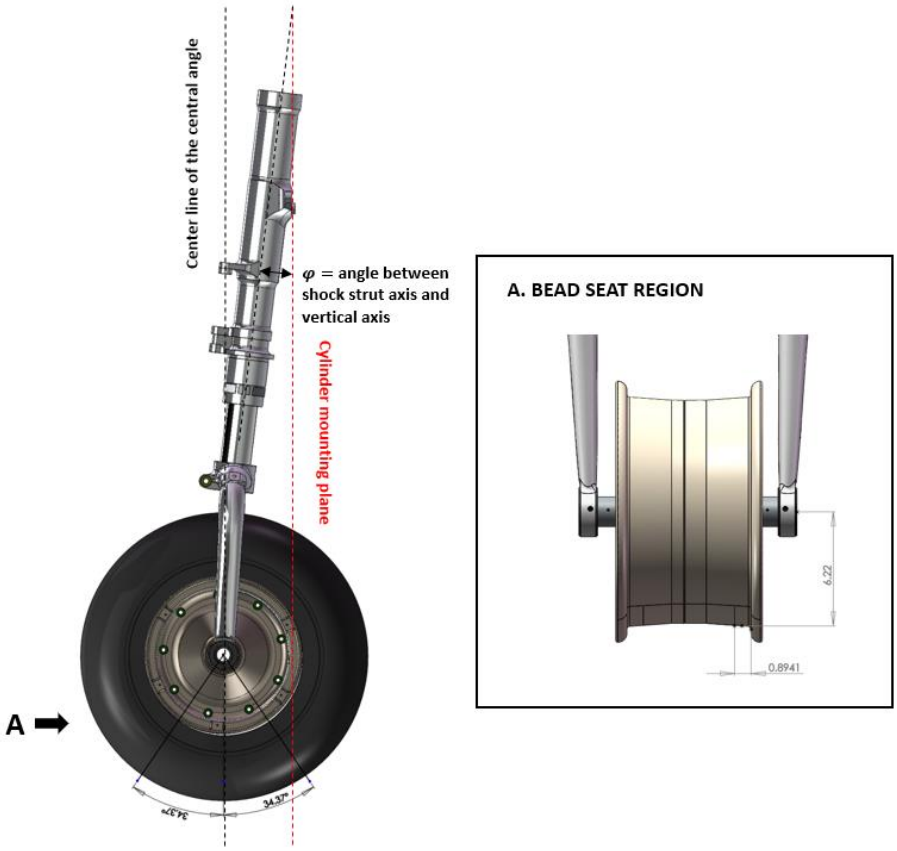

FIGURE 16: Contact Patch Region Alignment and Bead Seat Region Parameters

4.9.4 Eye-bar Loading Condition:

A conservative loading condition is formulated from the reserve energy loading condition, which yields the highest limit load factor under the shortest amount of time, can be referred to as a heavy landing or other abnormal impact condition. Piston extension is also correlated to the limit load factor and impact force to simulate the dampening response of the nose gear.

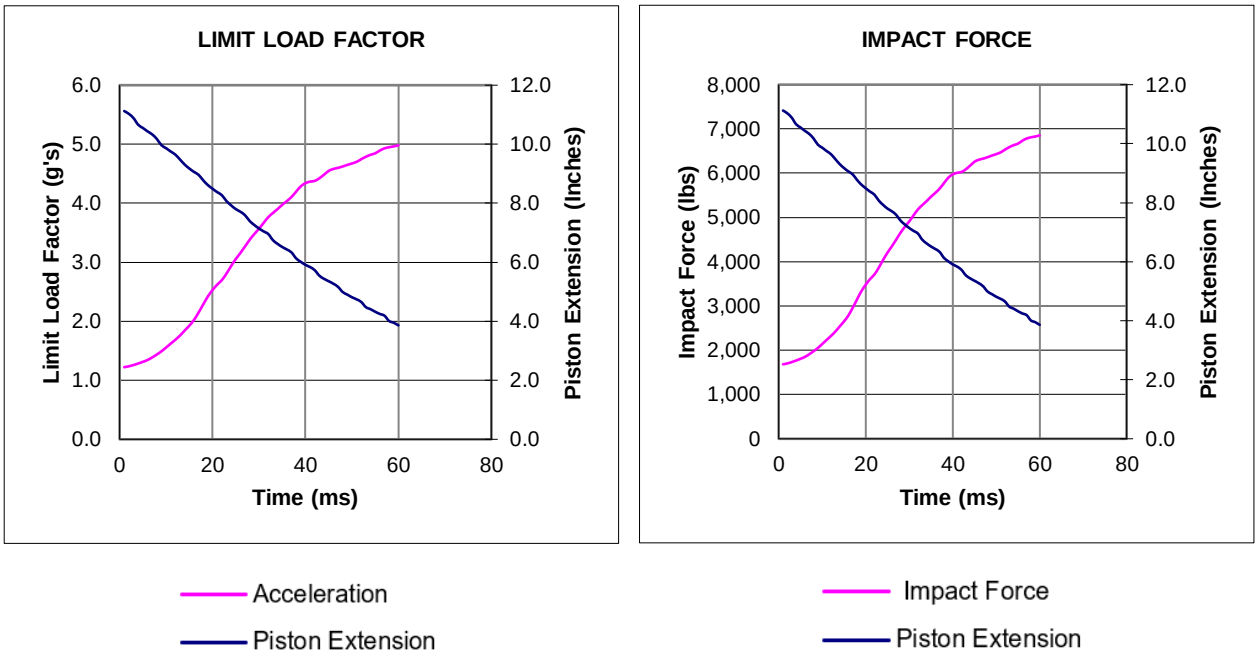

FIGURE 17: Dampening Response of Nose Gear

During the early designing stage of most landing gear systems, the estimated limit loading condition in Section 4.9.2 shall instead be utilized for the simulation study since the shock absorption testing is not yet performed. However, this is just a preliminary estimation under limit loading condition. Once shock absorbing testing data has been obtained, the loading condition for the simulation study must then be

correlated and adjusted as detailed in Section 4.7. The simulation study herein will instead proceed with the conservation loading condition (Figure 17) as a proof of concept to validate and establish this determination methodology of impact loading. The corresponding time curve of the limit load factor and impact force (Figure 17) is then converted to the time curve of the bead seat and rim flange pressures (Figure 18) using equation 2.4.

$$W_o = \frac{V_f * \pi}{b * r_b * 4 * \alpha}$$

Where:

$W_o =$ Bead seat and rim flange pressure

$V_f =$ Vertical impact force

$b =$ Bead seat width = 0.8941 in (Figure 16)

$r_b =$ The radius of the bead seats = 6.22 in (Figure 16)

$\alpha =$ Contact patch region = $68.73°$ (Figure 16)

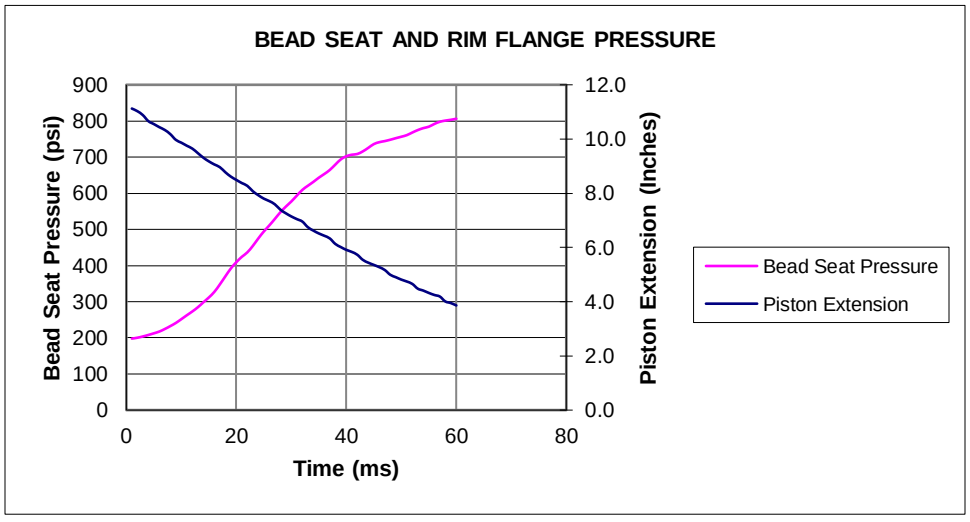

FIGURE 18: Bead Seat and Rim Flange Pressure Time Curve

Subsequently, a corresponding 4^{th} order polynomial equation can be developed from the given time curve of impact pressure (Figure 19). Five calculation points (with 15ms time steps) are also established during the 60ms impact period to simplify the simulation analysis while still achieve the necessary accuracy. From a technical perspective, the polynomial equation herein can be utilized as a starting point for research and development of other landing gear systems.

Polynomial Equation: $y1 = [2.157 * 10^{-4}] * x^4 + [-3.16372 * 10^{-4}] * x^3 + [1.4187278] * x^2 + [-7.8903827] * x + 214.6200635$			
x (Time-ms)	y1 (Bead Seat and Rim Flange Pressure-psi)	y1 prediction (psi)	y2 (Piston Extension - in)
0 through 1	197.80	208.17	11.24
15	311.57	319.62	9.25
30	577.20	575.27	7.20
45	735.93	734.04	5.40
60	806.04	810.45	3.89

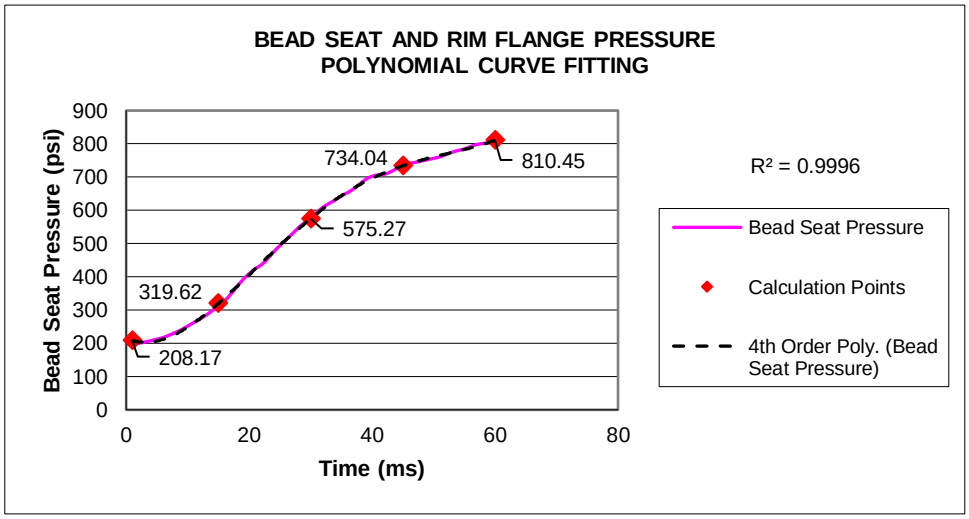

FIGURE 19: Bead Seat and Rim Flange Pressure Time Curve – Polynomial Curve Fitting

4.10 Shock Absorbing Loads

During the compressed stage, the oleo shock absorber load consists of hydraulic,

pneumatic, and the internal friction load. At the moment of impact, the shock absorber load starts to increase until 100% compression is reached. During this period, the spring rate increase dramatically due to the air being compressed while the viscosity of the fluid dampens the rebound movement. As the piston telescopes inward and causes the hydraulic fluid to flow through the orifice, the volume inside the cylinder reduces. Because of the reduction in volume, the internal pressure increases to create pneumatic, hydraulic, and internal frictional loads within the cylinder. These loads were subsequently analyzed during the period of impact for this simulation study. [2] [4]

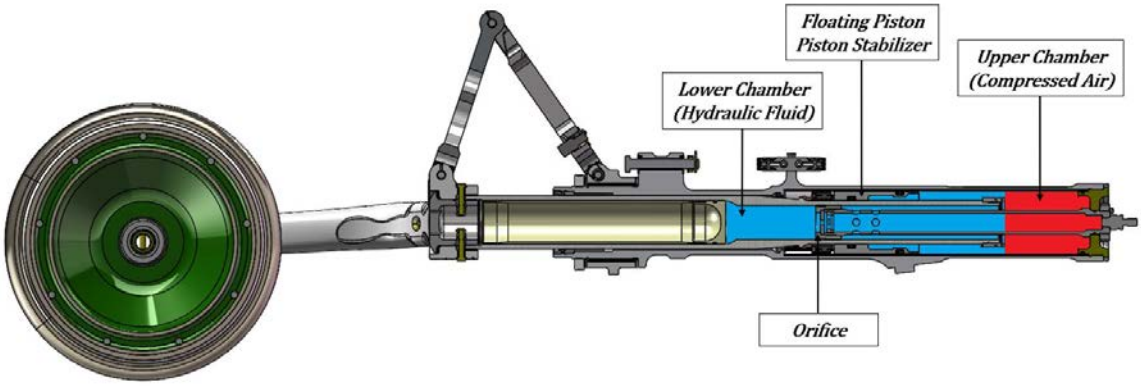

FIGURE 20: Shock Absorber Cross Section

4.10.1 Pneumatic Load:

The pneumatic load provides cushioning during ground operation and is created when air is compressed under a closed volume. In accordance with the required value from the Twin Otter Aircraft Overhaul Manual, the pneumatic load is prescribed to be 145 psi at 5.5” extension (static state) with an initial pressure of 95 psi at 11.24” piston extension (fully extended state). A standard notation for shock

absorbing sizing is then used to denote the fully extended state (1), static state (2), and compressed state (3). [7]

With the pneumatic area (A_a) of 3.96 in^2 and a total shock absorber stroke (S) of 11.24 in, the displacement volume (V_d) is approximated using equation 4.17.

$$V_d = S * A_a = 44.6 \text{ in}^3 \text{ [7]} \tag{4.17}$$

The reserved air volume at the fully compressed state (V_3) is assumed to be 10% of the displacement volume (V_d) to accommodate for the excess energy produced in a heavy or semi-crash landing. [7] The air volume at the fully extended position is then approximated as:

$$V_1 = V_3 + V_d = 49.01 \text{ in}^3 \text{ [7]} \tag{4.18}$$

The air volume between the extended and compressed states can then be determined as a function of fully extended air volume (V_1), the oleo shock absorber axial stroke (s), and the pneumatic area (A_a)

$$V_x = V_1 - A_a * s \text{ [4] [7]} \tag{4.19}$$

(With Axial Stroke = Fully Extended Piston - Piston Extension)

By using equation 4.19, the static air volume (V_2) can be calculated as

$$V_2 = V_1 - A_a * s_2 = 26.25 \text{ in}^3 \tag{4.20}$$

(With s_2 = Fully Extended Piston, 11.24" – Static Piston Extension, 5.5")

The effective polytropic exponent between the extended and static states (n_{1-2}) can then be determined from the corresponding pressures and volumes at the given conditions

$$P_2 = P_1 * (\frac{V_1}{V_2})^{n_{1-2}} \text{ [2] [4]} \quad (4.21)$$

thus n_{1-2} = 0.657

The evaluated result of n_{1-2} = 0.657 is also assumed to be constant throughout the extended and static states. The pressures between the extended and static states can then be derived using equation 4.22.

$$P_a = P_1 * (\frac{V_1}{V_1 - A_a * x})^{n_{1-2}} \quad (4.22)$$

$$s_{extend} < x < s_{static}$$

Where:

$P_a =$ Air pressure in the upper chamber of shock strut (Pneumatic Load)

$P_1 =$ Air pressure in the upper chamber for fully extended strut = 95 psi

$V_1 =$ The air volume of fully extended strut = 49.01 in^3

$A_a =$ Pneumatic area = Piston's external cross sectional area = 3.96 in^2

$s =$ Shock strut axial stroke = Fully Extended Piston - Piston Extension

$n_{1-2} =$ The effective polytropic exponent between the extended and static states

The effective polytropic exponent between the static and compressed states (n_{2-3}) are assumed to be 1.3 and constant throughout the static and compressed states to appropriately correspond to a very rapid compression in which an adiabatic process is almost attained. [4] The pressures between the static and compressed states can be derived using equation 4.23.

$$P_a = P_2 * (\frac{V_2}{V_1 - A_a * x})^{n_{2-3}} \quad (4.23)$$

$$s_{static} < x < s_{compressed}$$

Where:

$P_a =$ Air pressure in the upper chamber of shock strut (Pneumatic Load)

$P_1 =$ Air pressure in the upper chamber for fully extended strut = 95 psi

$V_1 =$ The air volume of fully extended strut = 49.01 in^3

$V_2 =$ Static air volume = 26.25 in^3

$A_a =$ Pneumatic area = Piston's external cross sectional area = 3.96 in^2

$s =$ Shock strut axial stroke = Fully Extended Piston - Piston Extension

$n_{2-3} =$ The effective polytropic exponent between the static and compressed states

The piston extension is then correlated to the pneumatic pressure as seen in Figure 21 to establish a graphical representation of the nose gear's dampening response.

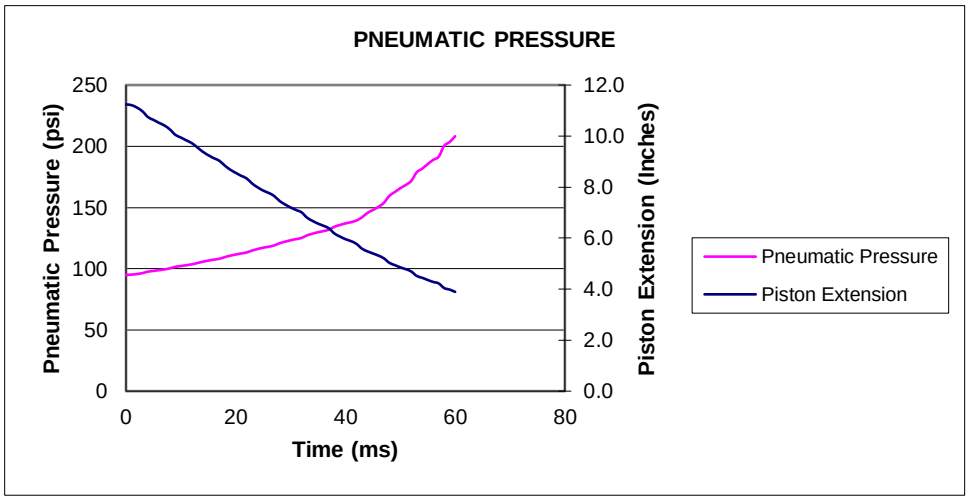

FIGURE 21: Pneumatic Load Time Curve

Similar to the impact pressure, a corresponding 4th order polynomial equation can also be developed (with 5 calculation points) from the given time curve of pneumatic pressure (Figure 22). The pneumatic pressure is then calculated at each

corresponding time step from the established polynomial equation to simulate the pressure change within the oleo shock absorber's upper chamber during the compressed state at the instant of impact.

Polynomial Equation: $y1 = [0.116 * 10^{-4}] * x^4 + [-6.316 * 10^{-4}] * x^3 + [0.0169406] * x^2 + [0.6783120] * x + 94.3568866$			
x (Time-ms)	y1 (Pneumatic Load-psi)	y1 prediction (psi)	y2 (Piston Extension - in)
0	95	94.36	11.24
15	106.63	106.80	9.25
30	123.21	122.30	7.20
45	147.94	149.20	5.40
60	208.18	209.95	3.89

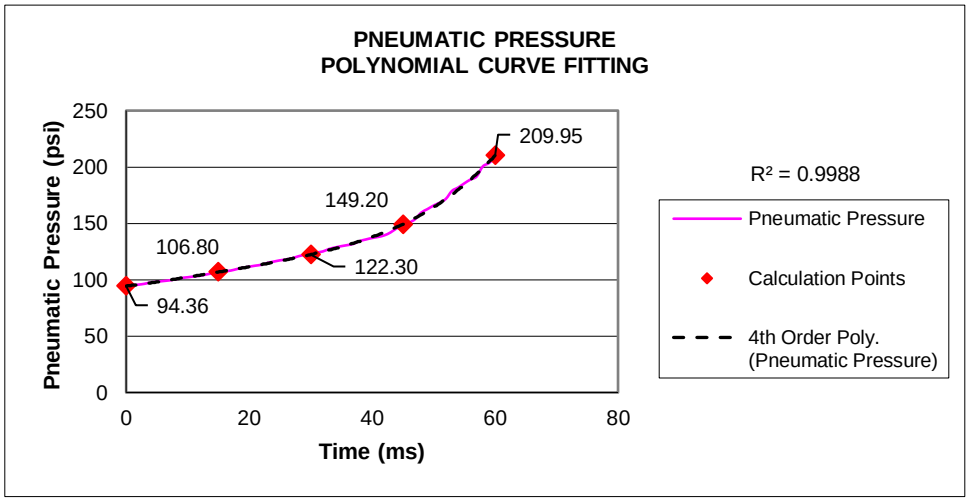

FIGURE 22: Pneumatic Load Time Curve – Polynomial Curve Fitting

As previously mentioned in Section 4.9, the pneumatic loading condition (Figure 22) herein shall be implemented as a proof of concept. Under the general circumstance where testing data is not available, the maximum value of pneumatic loading shall instead be assessed at the reserved air volume (V_d). This results in a maximum pneumatic load of 1454.60 psi for the estimated semi-crash landing condition per the established methodology in Chai and Mason's research. [7]

4.10.2 Hydraulic Load:

As the piston tube telescoping inward, the fluid is forced to flow through the orifice under compressed air and creates a hydraulic resistance load. During this period, the orifice area is small enough in relation to the diameter of the strut so that the jet velocities and Reynolds numbers are sufficiently large. This results in a fully turbulent flow and the energy dissipation during the compressed state.

Per the consideration of the shape of the orifice and the research data in previous nose landing gear behavior study for impact with tire bottoming, the orifice discharge coefficient (C_d) is assumed to be 0.9 and constant throughout the compression stroke. [4]

The differential pressure ($P_h - P_a$) between the lower and upper chamber can be determined as:

$$P_h - P_a = \frac{\rho * {A_h}^2 * \dot{s}^2}{2 * (C_d * A_n)^2} \text{ [4]} \qquad (4.24)$$

Where:

$P_h =$ Hydraulic fluid pressure in lower chamber of shock strut (Hydraulic Load)

$P_a =$ Air pressure in upper chamber of shock strut (Pneumatic Load)

$\rho =$ Fluid density = 0.0315 $\frac{lb}{in^3}$ = 54.432 $\frac{lbm}{ft^3}$

$A_h =$ Hydraulic area = Piston's – End Cap Tube's internal cross sectional area = 2.40 in^2 - 0.69 in^2 = 1.71 in^2 = 0.0119 ft^2

$A_n =$ $A_o =$ Orifice's opening area = 0.04 in^2 = 0.0003 ft^2

$C_d =$ Coefficient of discharge = 0.9

$\dot{s}$ = telescoping velocity

$$= \left| \frac{\text{Peak Load Piston Extension} - \text{Fully Extended Piston}}{coresponding\ time\ curve} \right|$$

$$= 122.5\ \frac{in}{s} = 10.21\ \frac{ft}{s}$$

With a constant differential pressure of 1195.53 psi and the pneumatic pressure in Section 4.10.1, the hydraulic load can then be appropriately correlated to the piston extension and calculated at each corresponding time step. This allows for the simulation of the pressure change within the oleo shock absorber's lower chamber during the compressed state at the instant of impact.

Similar to the pneumatic load in Section 4.10.1, a corresponding 4th order polynomial equation can also be developed for the hydraulic loading condition as a proof of concept (Figure 23). For study where testing data is not yet available, the maximum hydraulic load of 2650.13 psi shall instead be incorporated.

Polynomial Equation: $y1 = [0.116 * 10^{-4}] * x^4 + [-6.316 * 10^{-4}] * x^3 + [0.0169406] * x^2 + [0.6783120] * x + 94.3568866$			
x (Time-ms)	y1 (Pneumatic Load-psi)	y1 prediction (psi)	y2 (Piston Extension - in)
0	1290.53	1289.89	11.24
15	1302.16	1302.33	9.25
30	1318.74	1317.83	7.20
45	1343.47	1344.73	5.40
60	1403.71	1405.48	3.89

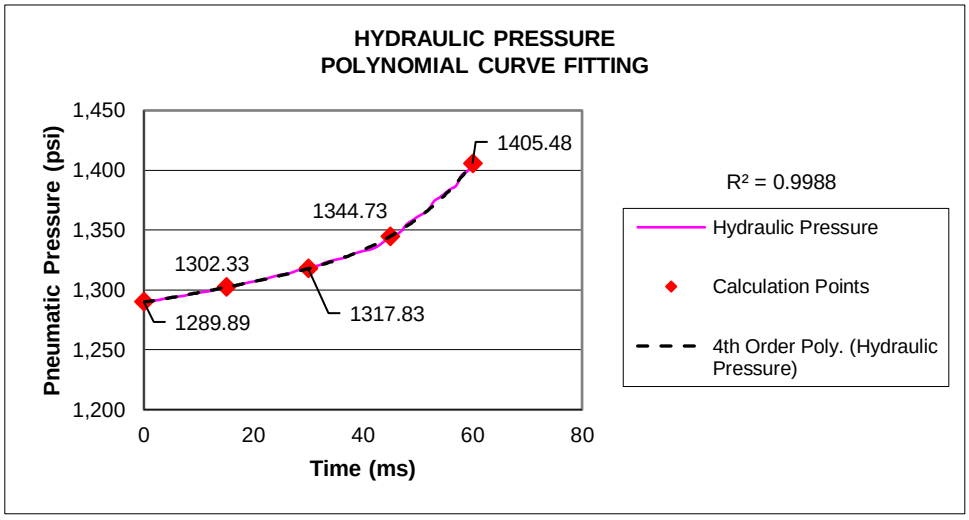

FIGURE 23: Hydraulic Load Time Curve – Polynomial Curve Fitting

4.10.3 Internal Friction Load:

The piston tube is supported by the Journal Bearing and Floating piston within the cylinder. During landing operation, the piston tube transverse axially from fully extended to fully compressed position. Frictional forces were created at two primary locations (Figure 24): the contact surfaces of the Journal Bearing/Piston Tube (N_1, Lower Normal Forces – attached to outer piston tube) and the Floating Piston/Cylinder's Sleeve (N_2, Upper Normal Forces – attached to inner cylinder). [2] [4] To provide these contact surfaces with unequaled load capacity, low friction, and

greatly extended service life, KAron self-lubricating liners were utilized. [15] Each corresponding coefficient of friction for the KAron liners was obtained for further understanding of the mechanical interaction at the Floating Piston/ Cylinder's Sleeve and Journal Bearing/Piston Tube locations.

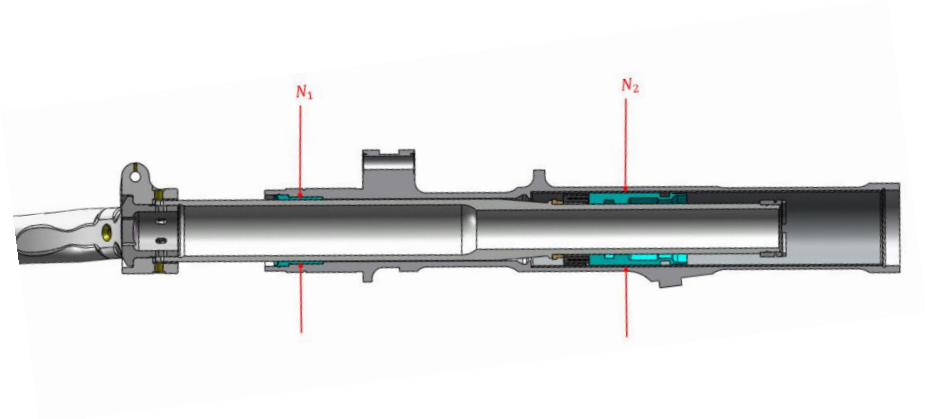

FIGURE 24: Normal Forces Location

For this research, both lower and upper normal forces are modeled using the contact surfaces condition in Section 5.4. Using equation 4.25, the internal friction load can then be determined to be the summation of two major frictional forces caused by the normal forces at contact surfaces of the Journal Bearing and the Floating Piston. With the low coefficient of friction provided from the Karon liners, the frictional effect at both contact interfaces is expected to be significantly small in comparison to the other loads. As such, they are determined to yield minimal impact on the overall loading analysis and therefore not included in the FEA.

$$F_f = \mu_1 * |N_1| + \mu_2 * |N_2| \text{ [2] [4]} \tag{4.25}$$

Where:

$F_f =$ Overall Internal Friction Load

$\mu_1 =$ Coefficient of friction at Journal Bearing/Piston Tube = Karon B's coefficient of friction = 0.065 [15]

$\mu_2 =$ Coefficient of friction at Floating Piston/Cylinder's Sleeve = Karon V's coefficient of friction = 0.055 [15]

$N_1 =$ Lower Normal Forces – attached to the outer surface of the piston tube

$N_2 =$ Upper Normal Forces – attached to the inner surface of the cylinder

5.0 Finite Element Analysis

The following section will derive the developing process for the required simulation study. NX Nastran Advanced Nonlinear – SOL601 simulation study is utilized to calculate the stresses and deformations of the shock strut and the nose wheel system. Initial assumptions, simulation model, fixture conditions, contact conditions, material properties, meshing method, and loads will be established and defined respectively.

5.1 Initial Assumptions

To appropriately simplify the simulation study without affecting its numerical accuracy, assumptions were made as follows:

The axial movement of the Floating Piston and Piston Tube during impact:

At the moment of maximum impact loading (highest reported load factor) per Figure 17, the Floating Piston and Piston Tube are assumed to be stationary at their top end to appropriately simulate the equilibrium period during the compressed stage. The equilibrium period is essentially a snapshot in time, where the compressive acceleration of the lower mass is completely resisted by the shock absorbing element. The compressed air and hydraulic fluid are also assumed to be a stationary interfacing medium during the equilibrium period. This allows for a direct load path from the top end of the Floating Piston and Piston Tube to the surrounding structures, most specifically the top mounting location of the Cylinder (Figure 28).

It is also important to note that the load factor per Figure 11B is also subjected to an exponential decay after the peak response. The load factor will then drastically approach 1 g's or the equilibrium condition, where the lower mass and shock absorbing elements will continuously support the effective weight of the aircraft's nose portion or resist the corresponding gravitational acceleration of 1 g's.

As the load factor gradually decreases from its peak response, the energy from the impact is gradually converted into heat and flowing fluid. The energy will then dissipate via the hydraulic fluid, compressed air, and structures within the internal chambers. The pneumatic and hydraulic loads in Section 4.10.1 and 4.10.2 also further validate this conservation of energy process, where the shock absorbing loads report an exponential increment in magnitude.

The pre-traveled distance of Piston Tube and Floating Piston prior to the impact between shoulder and bumper is also assumed to yield a negligible effect on the impact response. This assumption is also satisfied the established methodology in CAR § 3.245 Note (2), where the load factor shall be used with whatever shock absorber extension is most critical for shock absorbing element of the landing gear. Piston tube extension is then set at 3.89" to simulate the shock strut semi-dynamic configuration that will experience the highest impact response. Subsequently, this is also correlated to the negligible effect of friction in Section 4.10.3.

Constant inflation pressure:

The inflation pressure that acts on the nose wheel assembly is assumed to remain constant at 32 psi during the period of impact since the change of the tire volume is minimal during landing.

Tire and Wheel interface and impact point:

Eye-bar theory and contact patch region theory are utilized to define the regions of the wheel that will experience the highest pressure during the impact. Therefore, accurately simulate the tire and wheel behavior at the instant of impact. [2] [3]

Per CAR § 3.245, the tire shall be assumed to deflect to its static position during the period of impact. From that perspective, the tire can also be reasonably assumed to provide enough friction and stiffness to prevent the nose wheel from sliding forward and shifting sideways at their contact interfaces (fixed in both x and y direction).

The rotational movement and structural integrity of the Cone Bearing:

The rotational movement of the Cone Bearing is assumed to be negligible due to the very rapid compression period (60ms during the shock absorption test). Therefore, the Cone Bearing's configuration is also assumed to be one solid mechanical structure (Figure 25) to simplify the Wheel and Axle support interface.

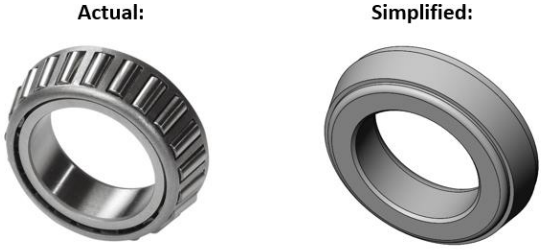

FIGURE 25: Structure integrity comparison of Cone Bearing

Bumper's material and geometric features:

The Bumper is composed of a nitrile rubber filler and three 4130 steel rings (Figure 26). In order to simulate a consistent loading condition, the adhesive bonding interfaces between the rubber filler and steel rings are assumed to yield the perfect quality.

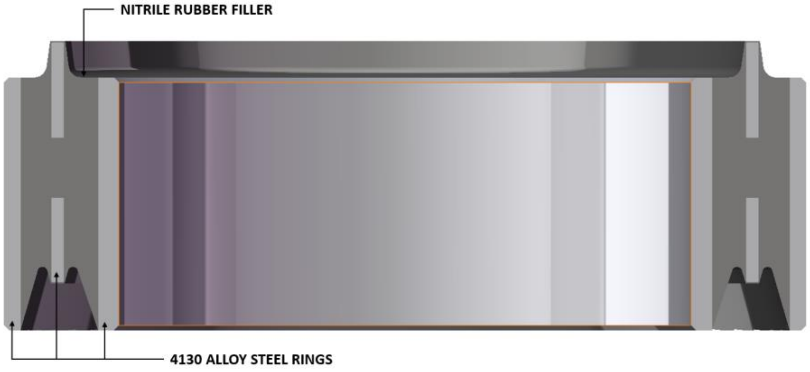

FIGURE 26: Bumper Cross-sectional View

The Bumper's geometric features are also simplified as shown in Figure 27 to ensure a uniform and non-distorted mesh. This, in term, will not affect the fit, form, and function of this article.

FIGURE 27: Geometric Features of the Bumper

5.2 Simulation Model

Direct Sparse Solver is utilized to calculate the stresses and deformations of the shock strut and the nose wheel system. For a proper convergence of forces and contacts, the nonlinearity parameters are defined as follows:

- **Geometric nonlinearity:** Small strain and displacement
- **Material nonlinearity:** Extend material curves to avoid element rupture (XTCURVE)
- **Load nonlinearity:** Deformation independent loading (LOADOPT)
- **Contact nonlinearity:** Small displacement contact (CTDISP)

  Add contact compliance (CFACTOR1)

  Increase friction regularization parameter (EPST)

  Gradually remove initial penetrations (INIPENE/TZPENE)

Automatic Time Stepping (ATS) is also activated to ensure a proper convergence rate.

5.3 Fixture Conditions

Fixture constraint is utilized to apply the boundary conditions to model at the following locations:

- Cylindrical fixture (Figure 28) is applied at top protrusion (radial direction), top bolt holes (radial and axial directions), and bottom outer bore (radial direction) of the Cylinder to appropriately simulate the interconnection with the airplane's fuselage

FIGURE 28: Boundary Condition at Cylinder

- Per Section 5.1 assumption, the stationary effect at the top end (and other minor areas) of Floating Piston and Piston Tube is applied via rigid connections to the top enclosing interface of cylinder (Figure 29). This appropriately provides a direct load path to the upper mass. Refer to Section 5.6 for further discussion

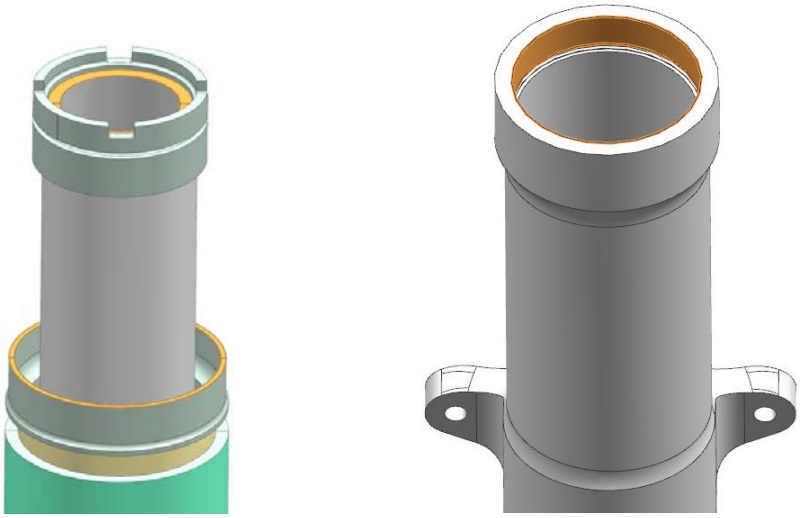

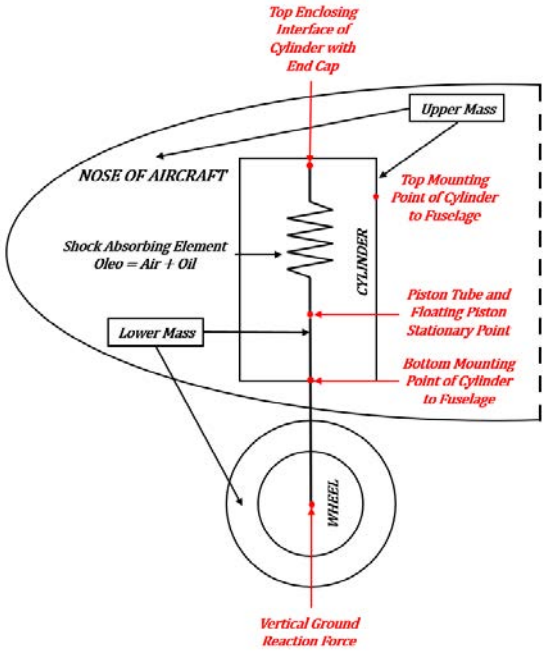

FIGURE 29: Boundary Condition at Piston Tube and Floating Piston

- Per Section 5.1 assumption, sliding translation fixture (x and y directions) is applied at the Nose Wheel's bead seat and rim flange areas to appropriately simulate their connection interfaces with tire (Figure 30). Additionally, rigid connections are also utilized to simulate the preloading effect to Cone Bearings from the Fork Assembly and Spacers

FIGURE 30: Boundary Condition at Nose Wheel

5.4 Contact Conditions

In NX Nastran, contact defines how each component interacts with one another within an assembly. Using the connector command between the source and target connector regions, contact connections can be created for component surfaces, thin-body, or sheet metal faces. Table 4 highlights the two most commonly used contact connectors between faces and surfaces.

Type of Contact	Description [16]
No Penetration (Surface/Surface)	Prevents interference between two entities but allows the gap to form.
Glued (Surface/Surface)	Bonds two entities together. The entities may be touching or be within a small distance from each other.

TABLE 4: Contact Descriptions

To simulate the proper Surface/Surface contact elements, both source and target regions must be determined correctly. The solver projects normal vectors for each of the faces of the elements located in the source region to the target region. When the contact regions do not have meshes with elements facing per one-on-one basis, the number of contact elements that the solver creates can vary depending on which region has been selected as source and which region as target. Therefore, the source region is chosen to be the one with the most refined mesh and the largest number of elements. This maximizes the number of contact elements between two contact surfaces, which will produce a more accurate solution. [17]

In this simulation study, only “Glued” Surface/Surface contacts is utilized (Table 5) to simulate two major categories of the nose landing gear’s suspension system: the upper (Figure 1B) and lower mass (Figure 1C). All connections between each article are also modeled to have coincident fit with their mating components.

Surfaces	Contact	Description
Fork Assembly/Axle	Glued (Surface/Surface)	The axle is bolted and pressed fit to the fork assembly to prevent rotational movement.
Locknut/Fork Assembly/Piston Tube/Nut	Glued (Surface/Surface)	The locknut is used to fix the piston tube to the Fork Assembly. The nut is threaded onto the Piston Tube’s top end.
Piston Tube/Shoulder/Bumper/Floating Piston	Glued (Surface/Surface)	The shoulder is mounted on the piston tube as the contact point to other components under the impact. At impact, the shoulder will be in contact with the bumper (absorbing the shock from the impact) and translate the impact response to the Floating Piston. Floating Piston is also used to center the top portion of the Piston Tube within the cylinder assembly.
Cone bearing/Axle	Glued (Surface/Surface)	Axle’s outer surface is pressed fit into Cone Bearing.
Nose wheel half/Bearing Cup	Glued (Surface/Surface)	Bearing Cup is pressed fit into Wheel Half’s center hub.
Cone bearing/Bearing Cup	Glued (Surface/Surface)	Cone Bearing is pressed fit into the Bearing Cup with the rotational movement of Wheel on Axle was determined to be negligible (See Section 5.1)
Floating piston/Sleeve	Glue (Surface/Surface)	Under impact, the Floating Piston will transverse axially and slide against the Sleeve. The internal friction effect is however assumed to be negligible (See Section 4.10.3)
Piston Tube/Floating Piston	Glue (Surface/Surface)	Under impact, the Piston Tube will transverse axially and slide against the inner wall of the Floating Piston. The internal friction effect is however assumed to be negligible (See Section 4.10.3)
Piston Tube/Journal Bearing	Glue (Surface/Surface)	Under impact, the Piston Tube will transverse axially and slide against the Journal Bearing. The internal friction effect is however assumed to be negligible (See Section 4.10.3)
Piston Tube/Bumper	Glue (Surface/Surface)	Under impact, the Piston Tube will transverse axially and may slightly slide against the Bumper's inner ring surface
Cylinder/Sleeve/Journal Bearing	Glued (Surface/Surface)	The Sleeve is slide fit into the Cylinder as a removable lining. The Journal Bearing is pressed fit into the Cylinder to center the bottom portion of the Piston Tube within the Cylinder Assembly, thus enable its axial movements.

TABLE 5: Contact Surfaces

5.5 Material Properties

The material properties for the components in Figure 1 and 2 will be defined in accordance with their manufacturing specifications. These properties will also be used to determine the factor of safety during the peak impact response.

5.5.1 Linear Isotropic Material:

Material	7075-T6 Aluminum Alloy (AMS4126)	7075-T73 Aluminum Alloy (AMS4617)	Heat Treated 4130 Alloy Steel (AMS6350)	Heat Treated 4340 Alloy Steel (AMS6415)
UTS (psi)	73,000	68,000	138,000	180,000
Yield Strength (psi)	62,000	57,000	63,000	103,000
Elastic Modulus (psi)	10,400,000	10,400,000	29,700,000	29,700,000
Poisson's Ratio	0.33	0.33	0.29	0.29
Density (lb/in^3)	0.102	0.102	0.284	0.284

TABLE 6: Linear Isotropic Material Properties

Material	304 Stainless Steel (AMS5567)	15-5PH H1075 Stainless Steel (AMS5659)	Tool Steel AISI L6 (ASTM A681)	Chrome Steel AISI E 52100 (AMS6440)
UTS (psi)	110,000	145,000	283,000	325,000
Yield Strength (psi)	30,000	125,000	277,000	295,000
Elastic Modulus (psi)	28,500,000	28,500,000	30,000,000	30,500,000
Poisson's Ratio	0.29	0.272	0.3	0.3
Density (lb/in^3)	0.289	0.283	0.284	0.282

TABLE 6 (Cont.): Linear Isotropic Material Properties

Material	AZ91C-T6 Magnesium Alloy (AMS4446)	C630000-HR50 Nickel Aluminum Bronze (AMS4640)	2014-T6 Aluminum Alloy (AMS4133)
UTS (psi)	34,000	110,000	64,000
Yield Strength (psi)	16,000	68,000	55,000
Elastic Modulus (psi)	6,500,000	16,700,000	10,600,000
Poisson's Ratio	0.35	0.328	0.33
Density (lb/in^3)	0.0654	0.274	0.101

TABLE 6 (Cont.): Linear Isotropic Material Properties

5.5.2 Ogden - Hyperelastic Material:

To appropriately determine the material constitutive behavior of the Bumper's rubber filler (Figure 25), the Ogden - Hyperelastic Material model is utilized [10]. A tensile test was performed on the five testing specimens (Figure 31) at a uniform rate of grip separation of 500 ± 50 mm/in (20 ± 2 in/min) IAW ASTM D412. [18]

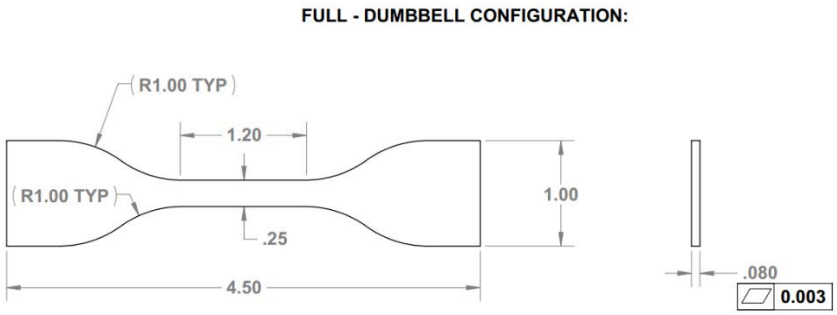

FIGURE 31: Nitrile Rubber Testing Specimens

Four resulted stress-strain curves (Figure 32) were then obtained and averaged.

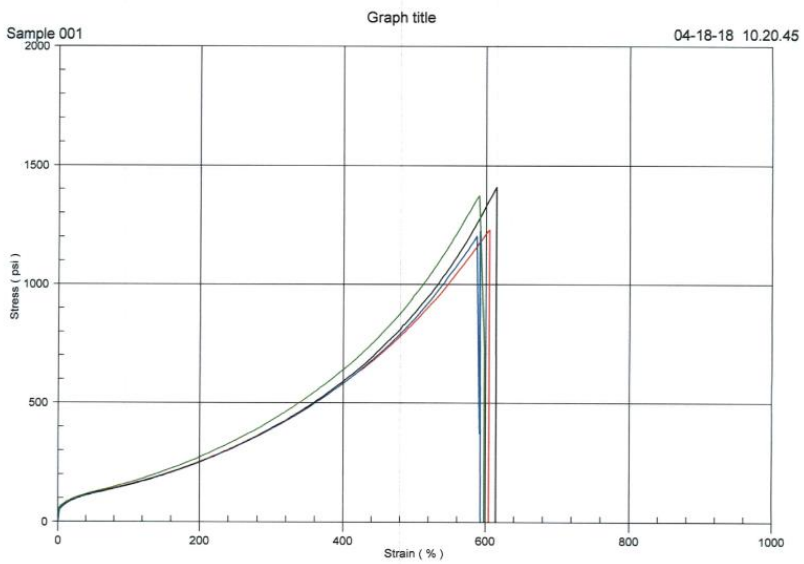

FIGURE 32: Resulted Stress-Strain Curve (Appendix B)

The resulted stress-strain data was then converted to Ogden's material constants and coefficients (Figure 33) using the average simple tension curve fitting method via Hyperfit, a software developed under Matlab's computational environment. With no volumetric testing data, incompressibility with a Poisson's ratio of 0.495 was also assumed. [11]

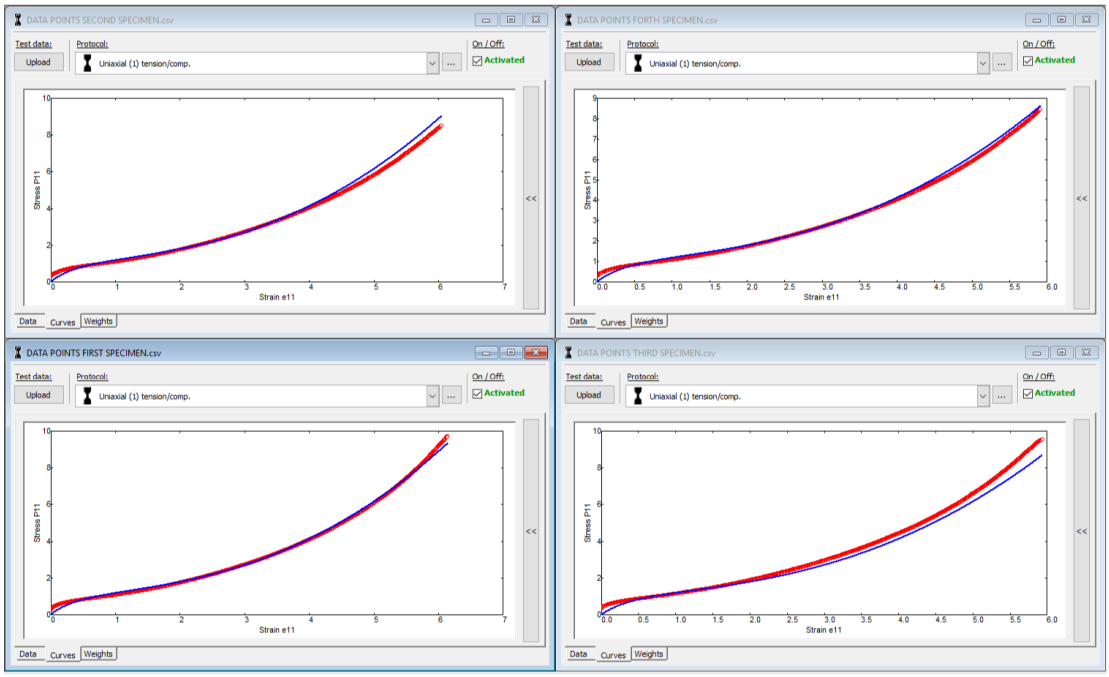

Constitutive Equation: $\Psi = \sum_{r=1}^{N} \frac{\mu_r}{\alpha_r}(\lambda_1^{\alpha_r} + \lambda_2^{\alpha_r} + \lambda_3^{\alpha_r} - 3)$

Material	NBR (ASTM 2000 M2BG 58 EO14)
μ_1	0.041
α_1	3.718
μ_2	-0.192
α_2	0.218
μ_3	7.184
α_3	0.126
μ_4	258.318
α_4	0.003
Poisson's Ratio	0.495
Density (lb/in^3)	0.0361

FIGURE 33: Ogden - Hyperelastic Material Properties

5.6 Meshing Method

In NX, meshing is the process of subdividing the model into a network of interconnected elements. Based on the geometry features of the model, the appropriate element type and quantity shall be assigned accordingly to the bodies as shown in Table 7.

Major Element Type	Description [17]
Scalar Elements (0-D)	Lack geometric definition and do not have an element coordinate system Use in conjunction with structural elements where details of the physical structure are not known or required
Line Elements (1-D)	Represent structural members that have stiffness along a line or curve (rod and beam behavior) Use as beam type structures, stiffeners, tie-down members, supports, mesh transitions, etc.
Surface Elements (2-D)	Represent structure whose thickness is small compared to its other dimensions (thin plate behavior) Use to model flat plates, single curvature (e.g. cylinder) and double curvature (e.g. sphere) shells
Solid Elements (3-D)	Represent structures that can't be modeled using beam or plate elements due to their three-dimensional nature Use to model an isotropic continuum for structural and thermal analysis
Rigid Elements (R-Type)	Use to impose fixed constraints between components of motion

TABLE 7: Elements Descriptions

Mesh Parameters

In this simulation study, the following rigid and quadratic solid elements are utilized in this research based on the geometric nonlinearity and dynamic condition of components within the landing gear and their contact interfaces:

- CHEXA20: Six-sided solid (brick/hexahedral) element with 20 grid points and widely recommended for general/simple geometry [17]

- CTETRA10 is a four-sided solid (tetrahedral) element with 10 grid points and widely used to model complicated geometry [17]
- CPENTA15 is a five-sided solid (wedge) element with 15 grid points and commonly used to model transitions between solids to plates or shells elements [17]
- CPYRAM13: Five-sided solid (pyramid) element with 13 grid points and commonly used to model transitions between tetrahedral to brick/hexahedral elements [17]
- RBE3: R-type element with interpolation constraints and can also produce constraint equations. This element defines the motion of a reference node as a weighted average of the motion of a set of other nodes, which is a useful tool for distributing applied load and mass in a model [17]

A combination of CHEXA20, WEDGE15, and CTETRA10 elements are utilized to ensure the most effective balance between numerical accuracy and computational time for all solid models. Since the complex shapes in nature are not support for direct hexahedral meshing, each of the models is manipulated by dividing into several interconnected regions. Hexahedral and tetrahedral elements are then mapped to these regions with the appropriate mesh mating conditions.

Per the NX meshing methodology's recommendation, a network of pyramid elements (CPYRAM13) is also formulated in each interconnection region to create a smooth and compatible transition between two different types of element. A detailed

meshing process is then established for the nose wheel half to significantly reduce to the total size of elements (Figure 34). Using this methodology, all remaining components also meshed with the same approach (Refer to Table 8).

From Section 5.1 and 5.3, the stationary effect at the top end (and other minor areas) of the Floating Piston and Piston Tube to Cylinder can be appropriately simulated by utilizing RBE 3 elements. With a proper setup of master (Floating Piston and Piston Tube) and slave surfaces (Cylinder), the applied load can then be evenly distributed to the top enclosing interface of the Cylinder with End Cap. Subsequently, the same methodology can be utilized for the Cone Bearings (master) and Fork Assembly (slave) to simulate the preloading effect for wheel and bearings.

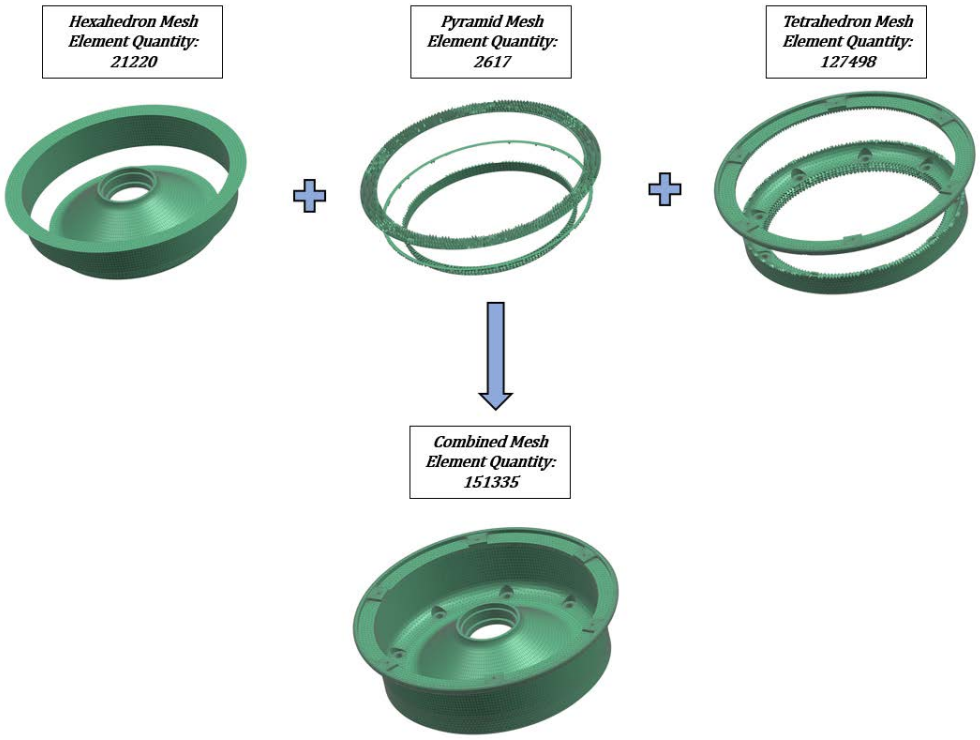

FIGURE 34: Element Type and Quantity for Inner Nose Wheel Half

Parent Assembly	Nomenclature	Tetrahedral (TETRA10)	Pyramids (PYR13)	Wedges (WEDGE15)	Bricks (HEX20)	Total Number of Elements
Cylinder Assembly	Cylinder	159287	0	0	0	159287
	Sleeve	0	0	45	5985	6030
Fork Assembly	Fork	132678	0	0	0	132678
	Bushing	34907	0	0	0	34907
	Bushing	6728	0	0	0	6728
Nose Wheel Assembly	Inner Nose Wheel Half	127498	2617	1897	19323	151335
	Outer Nose Wheel Half	140784	2728	1938	19834	165284
	Bearing Cup	0	0	180	1260	1440
	Cone Bearing	0	0	0	5180	5180
N/A	Axle	66387	164	0	4920	71471
	Piston Tube	25620	94	2538	8742	36994
	Shoulder	0	0	108	1620	1728
	Locknut	69234	0	0	0	69234
	Nut	4286	0	0	0	4286
	Floating Piston	0	0	378	1998	2376
	Journal Bearing	0	0	600	2900	3500
	Bumper	0	0	1830	9882	11712

TABLE 8: Components Elements Type and Quantity

Per the FEMAP and NX tutorial on solid elements [19], Element Conversion (ELCV=1) is also enabled. This effectively converts CHEXA20, CTETRA10, and CPYRAM13 to CHEXA27, CTETRA11, and CPYRAM14 respectively (Figure 35). The number of field variables, shape functions, and DOFs of each element is also altered by inserting the additional nodes to each type of solid elements. This provides the best approach to achieve the numerical accuracy for Hyperelastic material model and contact conditions.

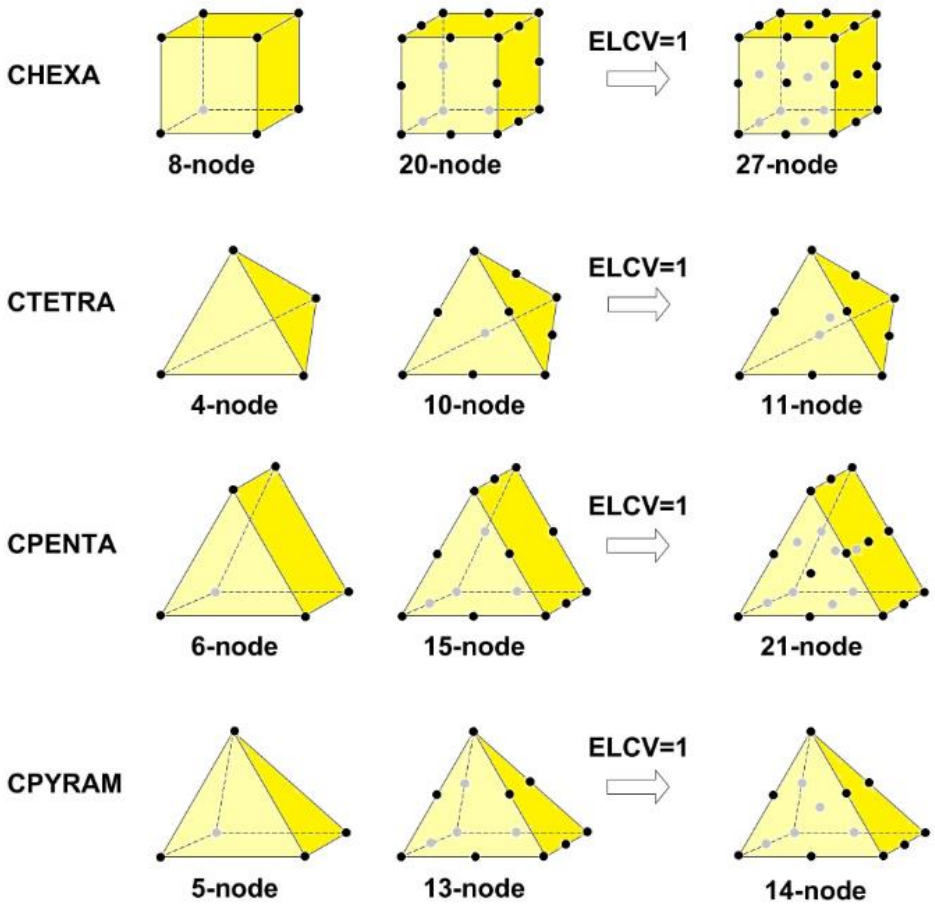

FIGURE 35: Conversion of 3D Solid Elements by ELCV = 1; Adapted from Iberisa [19]

Aspect Ratio [20]

For a solid mesh, numerical accuracy is best achieved by a mesh with uniform perfect elements whose edges are equal in length. However, it is impossible to create a mesh of perfect elements for a general geometry. The generated elements can have some of their edges much longer than others due to small edges, curved geometry, thin features, and sharp corners. When the edges of an element become much different in length, the accuracy of the results deteriorates.

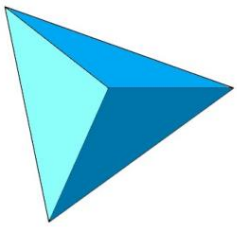

FIGURE 36: Tetrahedral Element with Aspect Ratio Close to 1.0, Adapted from Solidworks [20]

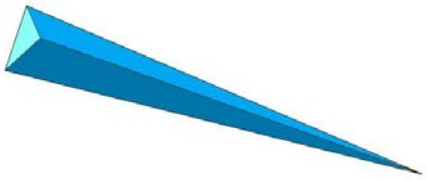

FIGURE 37: Tetrahedral Element with Large Aspect Ratio, Adapted from Solidworks [20]

The aspect ratio of an element is defined as the ratio between the longest edge and the shortest normal dropped from a vertex to the opposite face normalized with respect to perfect geometry. By definition, the aspect ratio of a perfect element is 1.0 and is used as the basis for calculating aspect ratios of other elements. To ensure numerical accuracy for complex geometry, the maximum percentage of elements with an aspect ratio > 10 is usually 5%. [21] This criterion is satisfied for this simulation study by utilizing the Element Quality inspect function (at 0.001%).

Jacobian Zero [22]

The Jacobian of an element is defined as a measurement of the deviation of one element's faces from its ideal shape. To obtain a physically realistic solution, the Jacobian of the deformation must be positive at all points of the domain. The Jacobian ranges from 1, a perfect element, to zero or even negative. When an element inverts, the Jacobian of certain areas of the element becomes so distorted in which indicates the presence of a zero or negative Jacobian. This results in the crossing of one element's relative face to another and causes the element quality to get worse.

In NX Nastran, the Jacobian Zero measures the minimum value for the determinant of the Jacobian at all integration points for each element. As an element vertex angle approaches 180°, the Jacobian Zero gradually approaches zero. Consequently, a positive Jacobian Zero is needed to generate a well-formed element. Per the industry and NX recommendations, a Jacobian Zero check of 0.1 was selected for the Element Quality inspect function to achieve numerical accuracy for this simulation study without scarifying too many computational resources.

Mesh Control [23]

Mesh Control is the method of defining different element sizes at specified regions in the model. Mesh control can be applied to vertices, points, edges, faces, and components to improve the accuracy results at the specified regions. In this simulation study, mesh control is applied at various areas to refine the rate of convergence and obtained results.

Final Mesh

By satisfying all meshing requirements, the final mesh of the FEM can be established as shown in Figure 38.

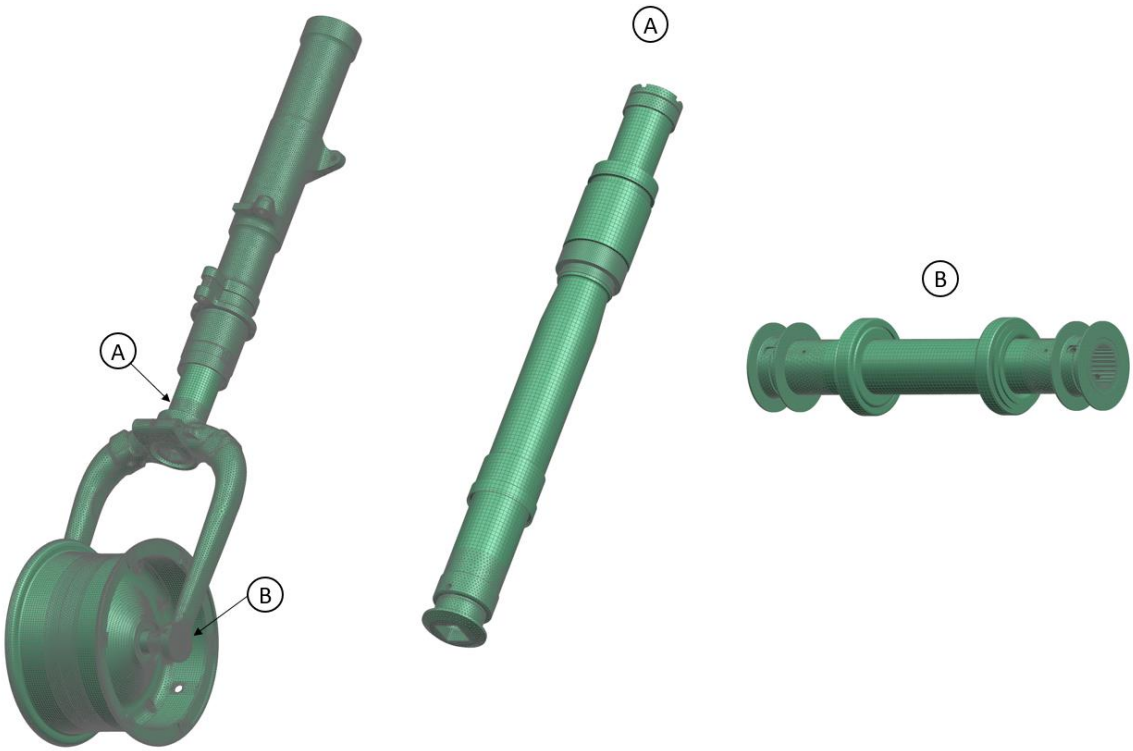

Total Solid Elements	864170(100%)
Total CHEXA	81644 (9.45%)
Total CPENTA	9514 (1.10%)
Total CTETRA	767409 (88.80%)
Total CPYRAM	5603 (0.65%)
Total Rigid Elements (RBE3)	3
% of Elements with Aspect Ratio > 10	0.001% (13 Elements)
Jacobian Zero	0.1

FIGURE 38: Final Mesh Parameters

5.7 Applied Loads

This following section details all applicable loads and their corresponding applied areas. All boundary conditions herein are consistent with previous assumptions and load determination.

Inflation Pressure

Per Section 5.1, a constant inflation pressure of 32 psi is distributed 360 degrees around the nose wheel (Figure 39).

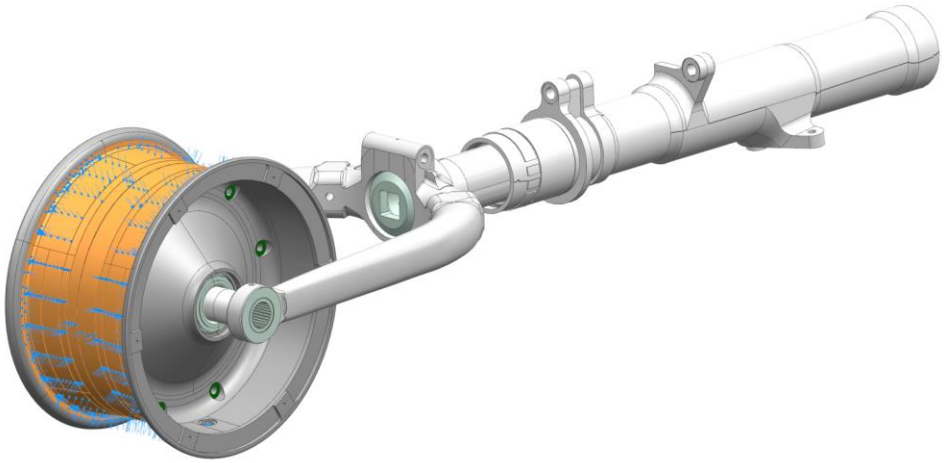

FIGURE 39: Inflation Pressure Distribution around the Wheel

Bead Seat and Rim Flange Pressure

Per Section 4.9.3 and 4.9.4, the bead seat and rim flange pressure is directly applied to the bead seat and rim flange regions (Figure 40).

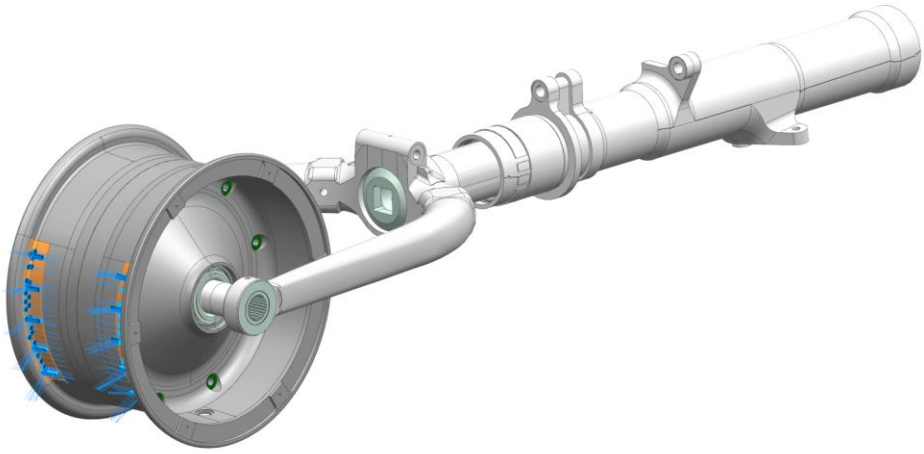

FIGURE 40: Bead Seat and Rim Flange Pressure Distribution around the Wheel

Pneumatic Load

Per Section 4.10.1 and 5.1, the pneumatic load was applied onto the top surfaces of the cylinder, top and external surfaces of the piston tube, floating piston, and the top region of the sleeve to accurately simulate the shock strut upper chamber's response during the impact period (Figure 41 and 42).

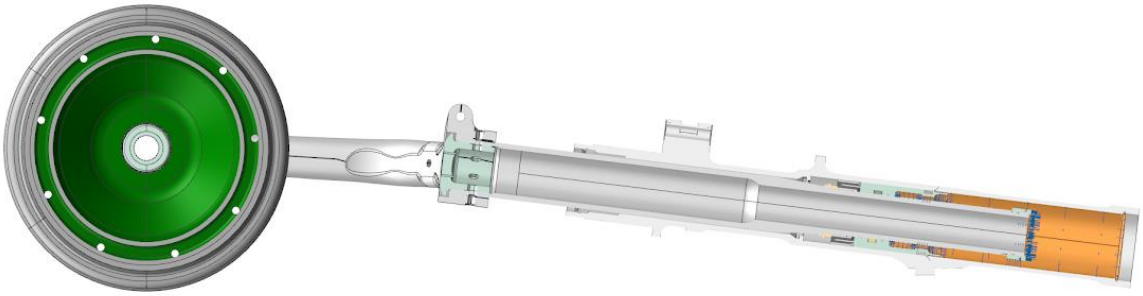

FIGURE 41: Side View of Pneumatic Loading Regions

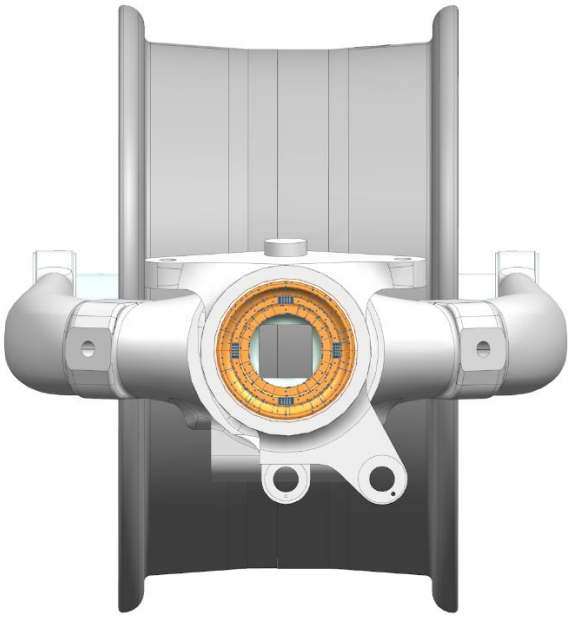

FIGURE 42: Top View of Pneumatic Loading Regions

Hydraulic Load

Per Section 4.10.2 and 5.1, the hydraulic load was applied onto the internal surfaces of the piston tube to accurately simulate the shock strut lower chamber's response during the impact period (Figure 43).

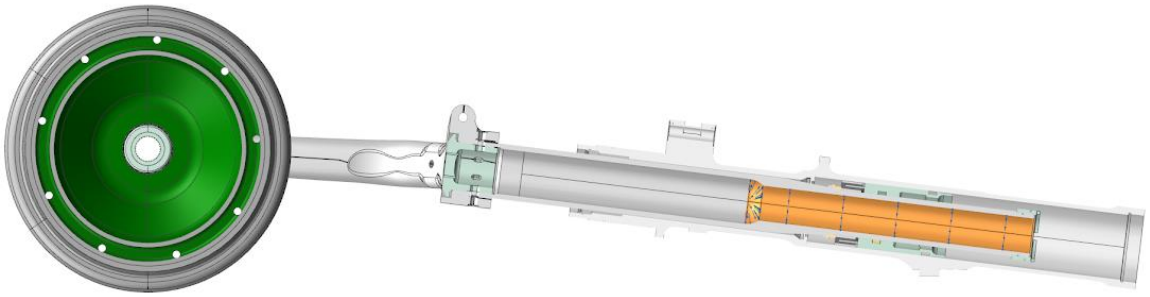

FIGURE 43: Side View of Hydraulic Loading Regions

Internal Friction Load

Per Section 4.10.3 and Table 5, the internal friction load was modeled as normal contact force using glued surface/surface contact with no frictional effect (Figure 44).

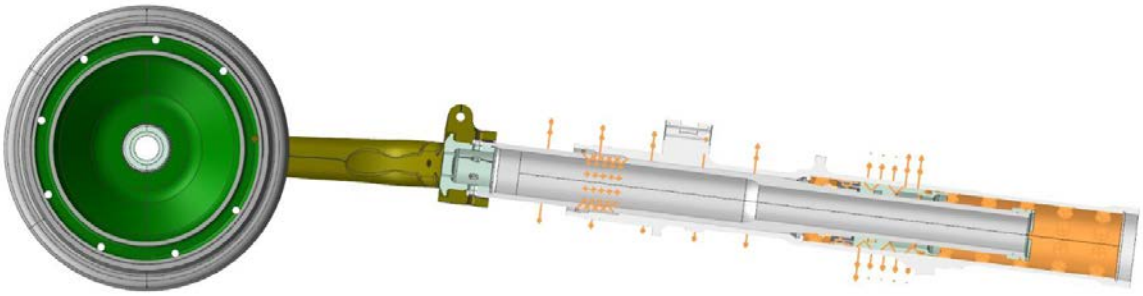

FIGURE 44: Frictional Contact Regions

6.0 FEA Results

The following section will discuss and elaborate on the obtained FEA results of the described simulation study in Section 5.0. Per Figure 45, the overall simulation runtime is approximately seven hours with eight total equilibrium iterations.

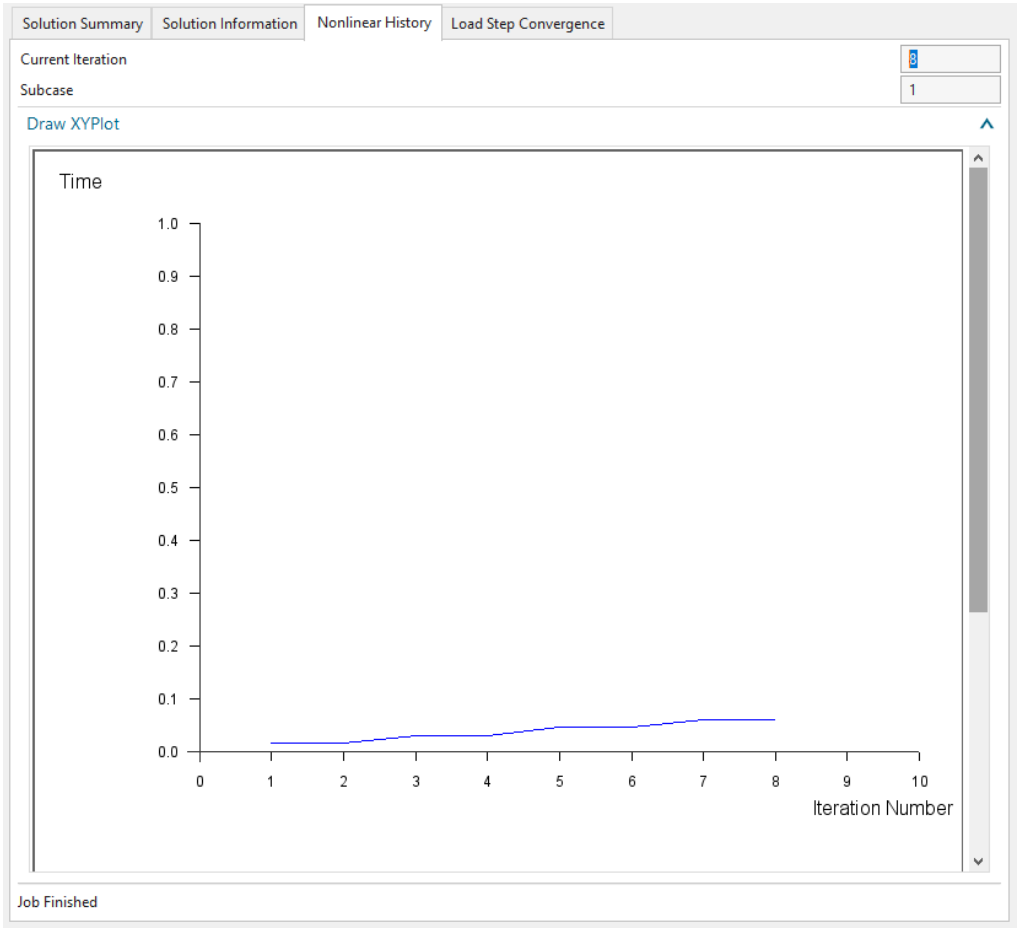

Time Step (ms)	0.015	0.03	0.045	0.06	**Total**
Number of Equilibrium Iteration	2	2	2	2	8

FIGURE 45: Nonlinear History

6.1 Convergence Considerations

For this simulation study's solution (NX Nastran Advanced Nonlinear – SOL601), four primary equilibrium iterative processes were performed, evaluated, and converged during the incremental analysis:

- **Energy equilibrium iteration**, which is corresponded to one non-contact related norm: Energy Convergence Tolerance criterion (ETOL). For all degrees of freedom, this criterion is a user-specified tolerance [16]
- **Force equilibrium iteration**, which is corresponded to one non-contact related norm: Force Convergence Tolerance criterion (RTOL). For translational degrees of freedom, this criterion is a user-specified tolerance and is formulated from the Reference Force (RNORM), which is automatically determined by the program during execution [16]
- **Contact equilibrium iteration**, which is corresponded to one contact related norm: Contact Force Convergence Tolerance criterion (RCTOL). This criterion is used when contact is present and formulated from Contact Forces parameter (CFORCE) and Contact Force Vector parameter (CFNORM) [16]
- **Line search iteration**, which is corresponded to the Line Search Convergence Tolerance (STOL). This criterion is a user-input tolerance and is used for plasticity, large displacement, and contact problems [16]

6.2 Convergence Parameters

To ensure a stable incremental solution for this simulation study, the convergence parameters are defined in accordance with the NX recommendation for standard Newton method [16] as follows:

- Energy Convergence Tolerance criterion (ETOL) = $1\ x\ 10^{-6}$
- Force Convergence Tolerance criterion (RTOL) = $1\ x\ 10^{-2}$
- Contact Force Convergence Tolerance criterion (RCTOL) = $1\ x\ 10^{-3}$
- Line Search Convergence Tolerance (STOL) = $1\ x\ 10^{-2}$

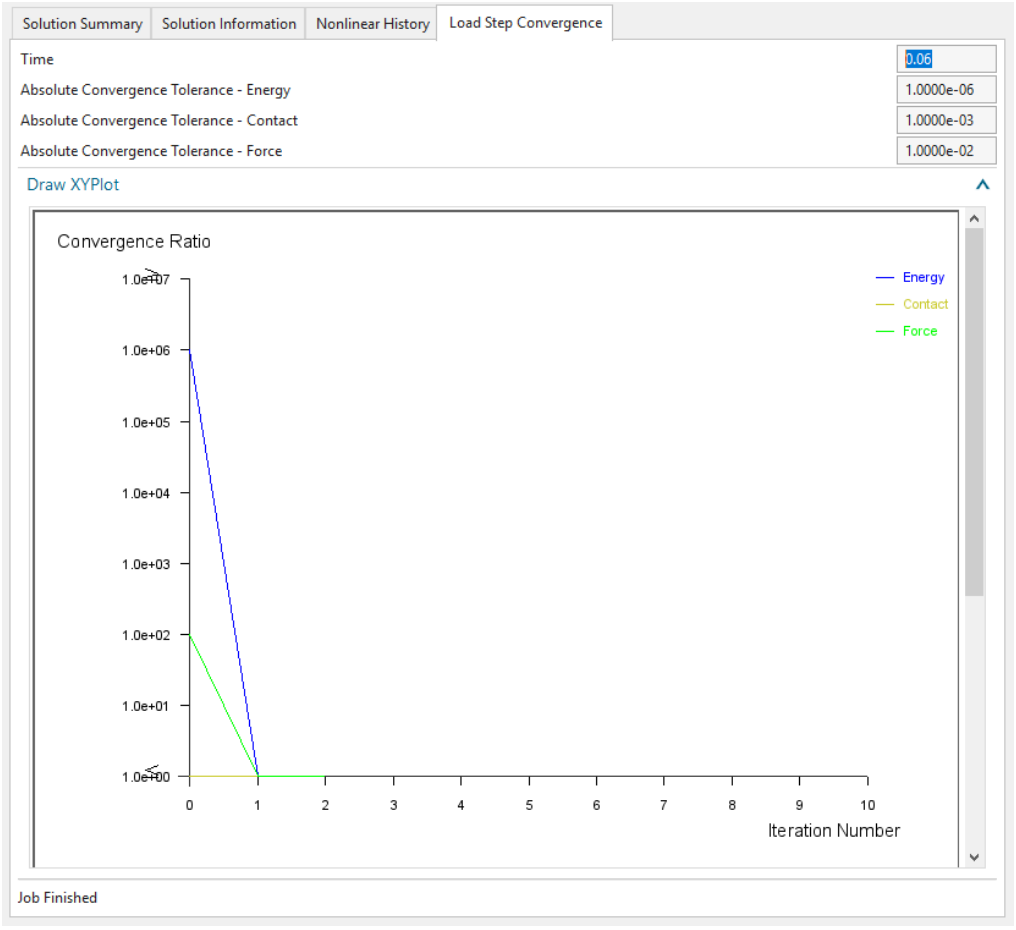

FIGURE 46: Load Step Convergence

6.3 Post-Processing Validation

In accordance with CFR 23.301 (b), all method used to determine load intensities and distributions must be validated to show reliability or conservativeness. From that perspective, this following section will detail and set forth the necessary validation for this simulation study.

Free Body Diagram:

For a proper understanding of the structural behavior and a reasonable idea of the FEA result, a Free Body Diagram (FBD) must be developed and utilized as a validation method in accordance with the FAA requirements on finite element modeling and analysis validation [24]. As such, an FBD for the static loading condition per CAR 3.253 at the nose landing gear was formulated and compared against the result of this simulation study.

The boundary condition is however only pertained to a conservative loading system of the nose landing gear, where the effect of the shock absorbing elements was not included and the cylinder interconnections with the airplane's fuselage (Figure 27) were the only fixed support.

Minor alteration of the above FBD was also required for the appropriate correlation to the shock absorption testing per CAR 3.243 and 3.353. The vertical load was subsequently adjusted from 4113 lbs (static condition) to 5317.26 lbs (dynamic condition) with the exclusion of side, forward, and aft loading conditions. The vertical component of the limit force was then applied at the axle per CAR 3.254 to 3.256, as seen in Figure 47.

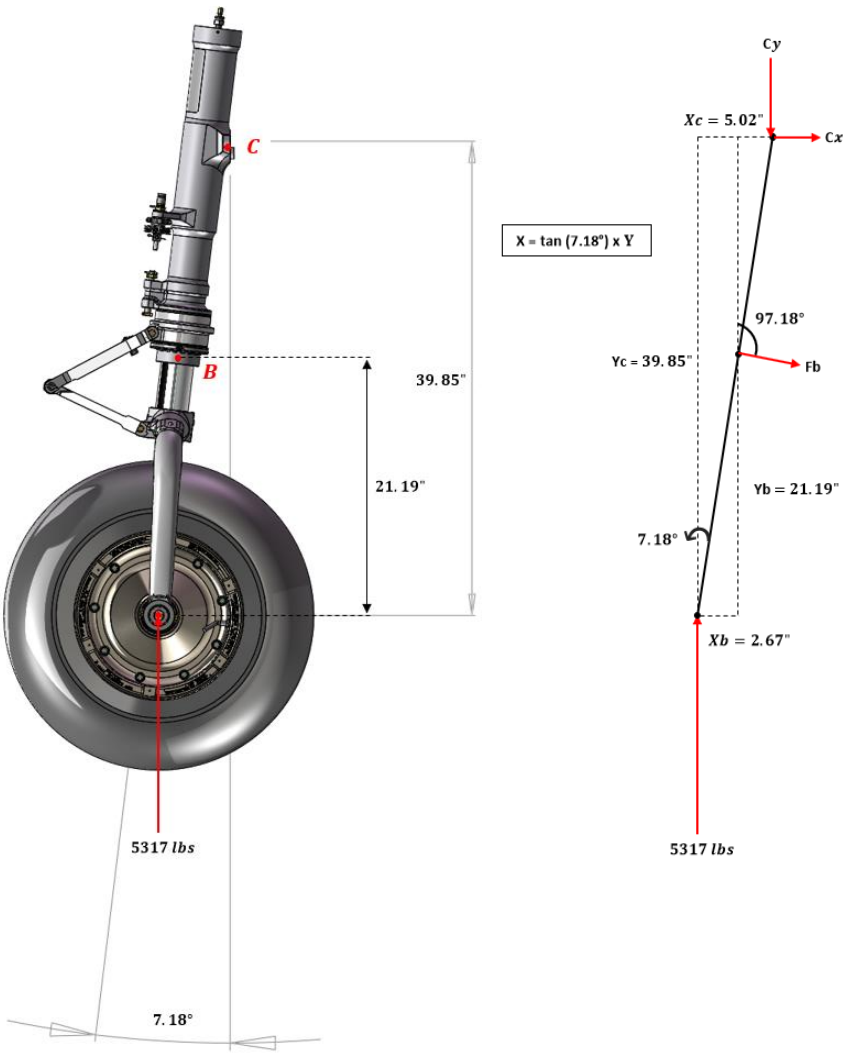

FIGURE 47: Free Body Diagram of The Conservative Loading System for The Nose Landing Gear

The reaction forces (Cx, Cy, Fb) in Figure 46 can then be derived as follows:

$$\overset{\curvearrowleft}{+} \Sigma M_C = -5317\ lbs * Xc + Fb * \sin(82.82°) * (Yc - Yb) + Fb * \cos(82.82°) * (Xc - Xb) = 0$$

$$Fb = 282.7\ lbs$$

$$\overset{+}{\rightarrow} \Sigma F_X = Cx + Fb * \sin(82.82°) = 0$$

$$Cx + Fb * sin(82.82°) = 0\ lbs$$

$$Cx = -280.5\ lbs$$

$$+\uparrow \Sigma F_Y = 5317\ lbs - Cy - Fb * \cos(97.18°) = 0$$

$$Cy + Fb * cos(82.82°) = 5317\ lbs$$

$$Cy = 5281.7\ lbs$$

Model Validation Procedure:

Generally, the applied forces and reaction forces of a study can be requested in the NASTRAN simulation environment via two diagnostics:

- **OLOAD Resultant**, which represents the resultant of all applied loads with respect to the basic coordinate system of a simulation study. The diagnostic is automatically calculated for each applied load vector
- **SPCFORCE Resultant**, which represents the summation of all reaction forces with respect to the boundary conditions of a simulation study

For most static analysis in NASTRAN, a quantitative validation process can usually be performed by verifying that equilibrium in forces has been obtained. This will ensure that the simulation model has reached its static equilibrium, where the summation of all applied and reaction forces must be approximately zero. However, this validation process is not yet available for dynamic analysis in NX and thus is not implemented for this simulation study. Refer to Section 7.0 for further discussion about the future implementation of this quantitative methodology.

At the FAA recommendation for post-processing validation of the FEA [24], the summation of reaction forces from SPCFORCE Resultant (Figure 48) was instead compared with the formulated FBD (Figure 47). This provides a means to assess the sensitivity of the reaction forces from the simulation and the expected static loading condition.

For a proper comparative analysis, the summation of reaction forces in Z-Direction from SPCFORCE was also divided by two to account for the evenly distributed ground reaction loads on both wheel half. The result indicates a negligible difference in structural loading characteristics, more specifically the sensitivity of reaction forces as follows

- Vertical Component (10% difference): 5282 lbs (FBD) vs 5914 lbs (SPCFORCE)
- In-plane Horizontal Component (8% difference): 281 lbs (FBD) vs 256 lbs (SPCFORCE)
- Out-of-plane Horizontal Component (negligible difference): 0 lbs (FBD) vs 44 lbs (SPCFORCE)

A 5% model's deformation on displacement was also developed to check for the rationality of the Nose Landing Gear's deflected shape. The resulted animation in Figure 49 indicates a sufficiently accurate deformation behavior with no unexpected rigid body motion.

Since the solid elements do not have any rotational degree of freedoms (DOFs), there shall be no moment resistance at the boundary condition. As such, the reaction moments are not reported within the SPCFORCE calculation environment. Although there will still be an effect of moment and it can still be detected per the estimated deformation in Figure 49.

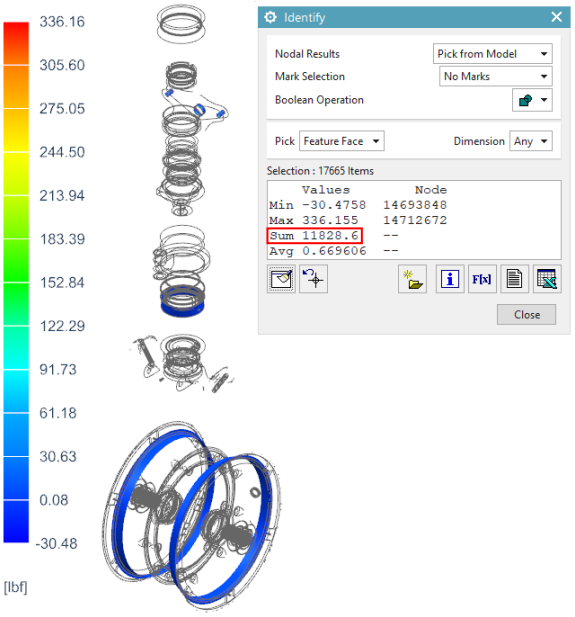

(A)

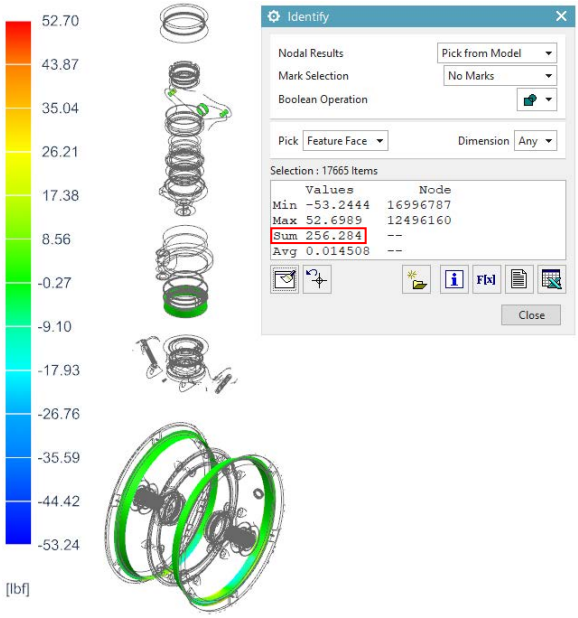

(B)

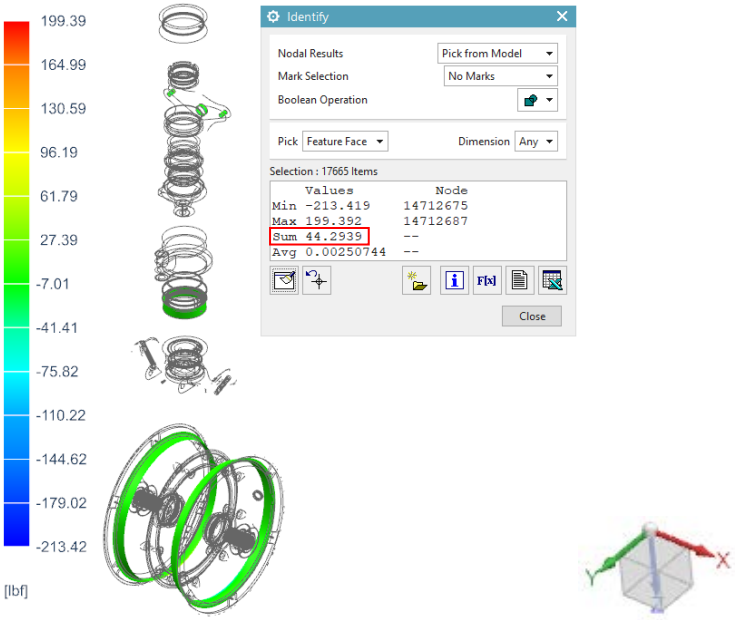

(C)

FIGURE 48: Reaction Forces Assessment of Z-Direction (A); Y-Direction (B); X-Direction (C)

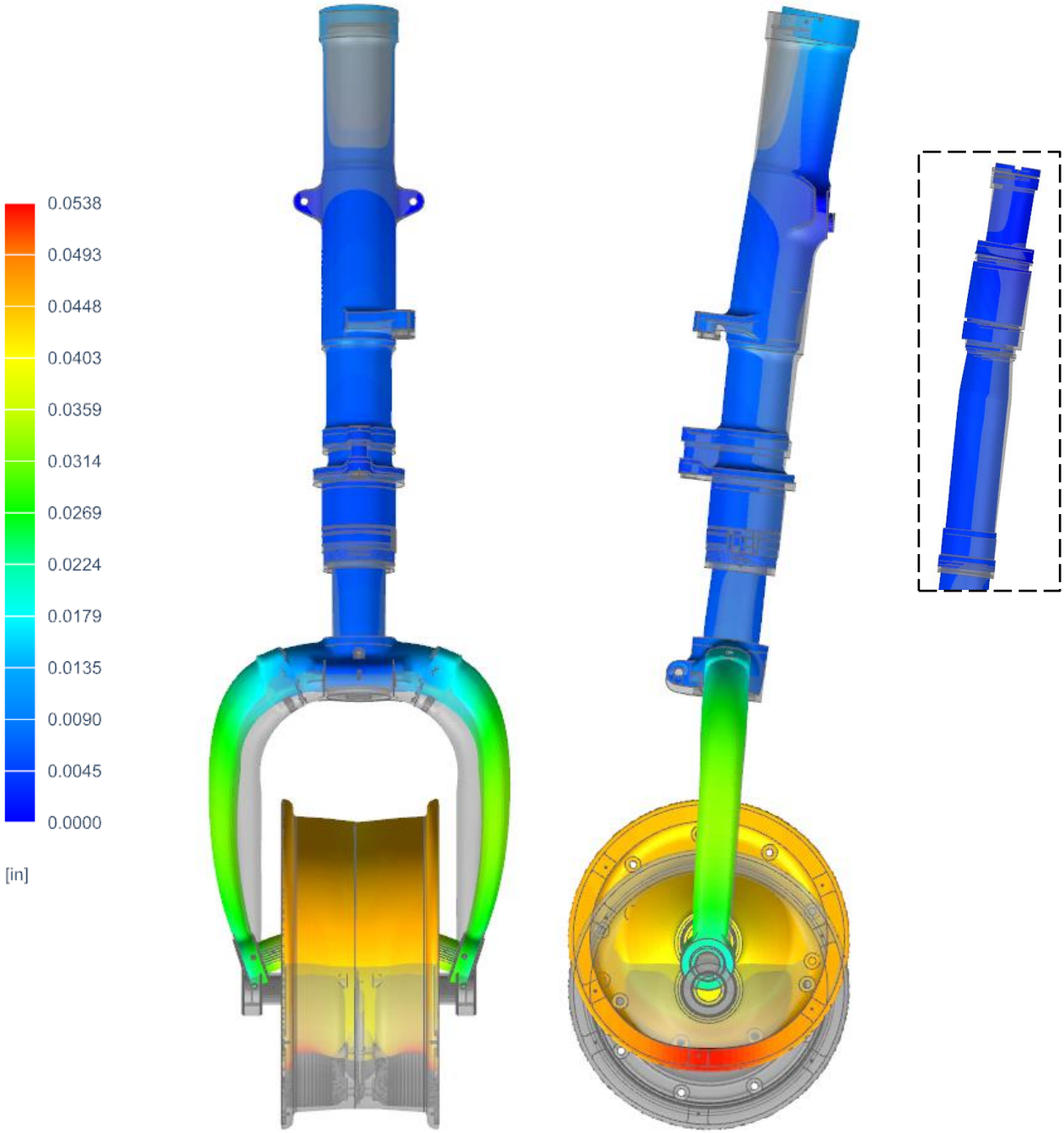

(A) **(B)**

FIGURE 49: Front View (A) and Side View (B) of 5% Model's Deformation on Displacement

6.4 Results

In NX Nastran's solution process, the calculated stress and deformation can be reported into two major categories: Element and Nodal-Element. Element values is typically the calculated result for the element at the gauss points. The Element values are then extrapolated out to the nodes and then averaged to give Nodal-Element values. As the mesh at high-stress regions is refined, the ratio between Element and Nodal-Element values can be utilized as a convergence criterion. Per NX and industrial standard, a ratio of successive mesh refinements should only reflect a maximum difference in stress and deformation values of 10% for simple structures and 20% for complexed structures.

Utilizing the convergence criterion above, the report for minimum and maximum values of stress and deformation will follow the Element result with the display option property of the resulted object set to "Nodal Averaged". They can be then compared to the Nodal-Element values with the display option property of the resulted object set to "Element Averaged". With no violation of the maximum difference between the stress and deformation values, a successive mesh refinement is achieved, and the corresponding convergence criterion can be then assessed as "converged" for this simulation study.

Overall Result:

The overall result (Figure 50) indicates that the maximum stress occurs near the bearing areas on Axle while the maximum deformation happens at the upper mounting interface of the cylinder assembly. Concurrently, another high-stress location can be

detected at the Fork Assembly/Piston Tube/Lock Nut contact interface while the high-deformation happens at the contact patch regions of the nose wheel assembly.

Each component stress and deformation values are calculated and documented in Table 9. The stress values are compared with each respective ultimate tensile strength (UTS) for the estimated factor of safety. Per CAR 3.353, yielding or plastic deformation of each component will be permitted.

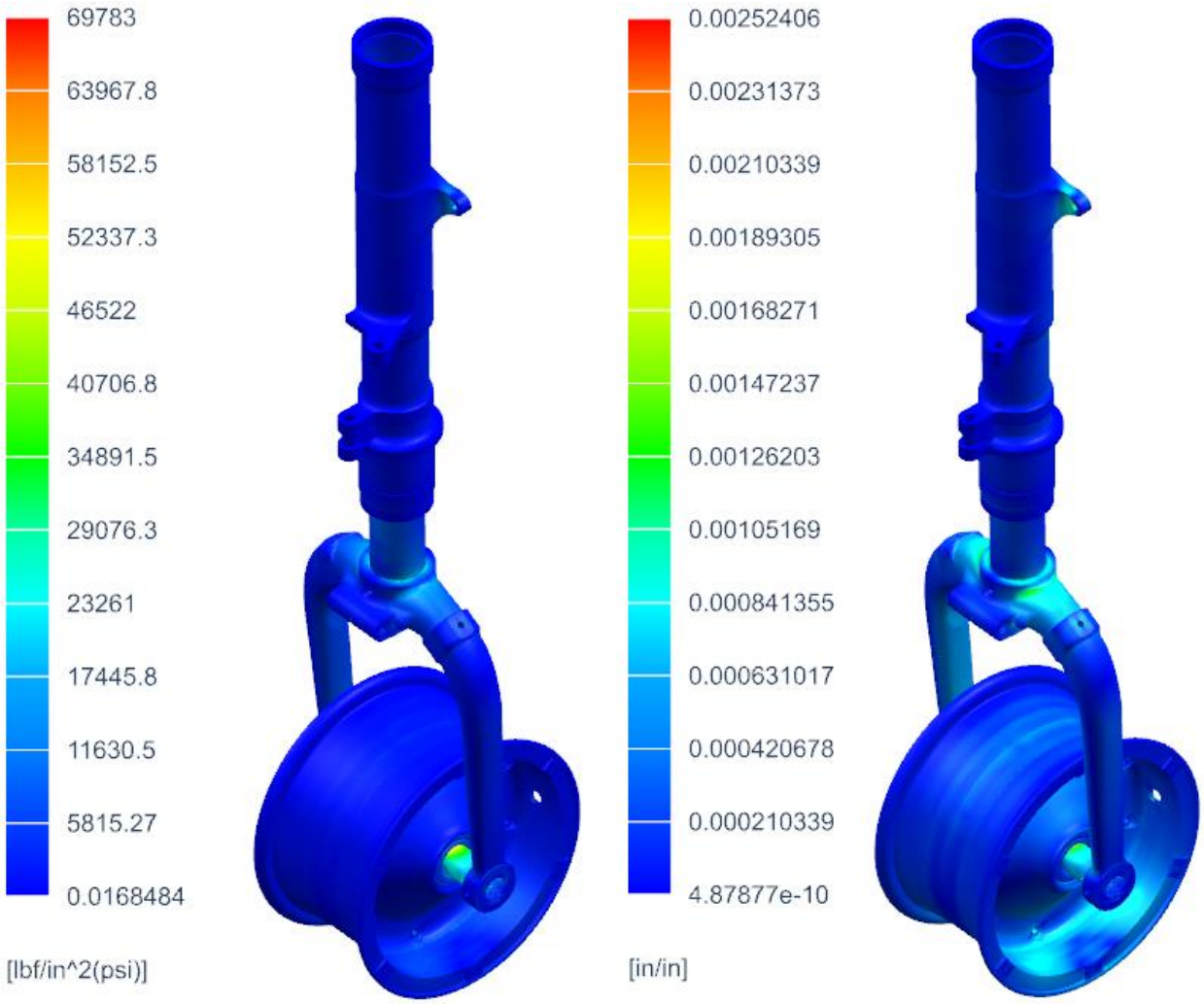

(A) **(B)**

FIGURE 50: Stress (A) and Deformation (B) of Shock Strut Assembly

Parent Assembly	Nomenclature	Calculated Von Mises Stress (psi)	Calculated Strain (in/in)	Yield Strength (psi)	UTS (psi)	Factor of Safety
Cylinder Assembly	Cylinder	30175	**0.0025 (MAX)**	55000	64000	2.12
	**Sleeve	16447	0.0005	125000	145000	8.82
Fork Assembly	Fork	22334	0.0019	62000	73000	3.27
	Bushing	56491	0.0016	103000	161000	2.85
	Bushing	29840	0.0016	68000	110000	3.69
Nose Wheel Assembly	*Inner Nose Wheel Half	17475	**0.0024 (MAX)**	16000	34000	1.95
	Outer Nose Wheel Half	15176	0.0021	16000	34000	2.23
	**Bearing Cup	8421	0.0002	277000	283000	33.61
	**Cone Bearing	21067	0.0006	295000	325000	15.43
N/A	Axle	**69787 (MAX)**	0.0020	103000	161000	2.31
	Piston Tube	24989	0.0007	103000	161000	6.44
	**Shoulder	8768	0.0003	103000	161000	18.36
	Locknut	42898	0.0012	103000	161000	3.75
	**Nut	3058	0.0003	62000	73000	23.87
	**Floating Piston	6243	0.0005	57000	68000	10.89
	**Journal Bearing	8267	0.0003	30000	110000	13.31
	**Bumper	2365	0.0001	63100	97200	41.01

** Indication of plastic deformation, more specifically the sustained stress is larger than yield strength*
*** Indication of a high factor of safety. See to the respective section for further assessment with Failure Modes and Effects Analysis (FMEA)*

TABLE 9: Calculation Result for Stress, Displacement, and Factor of Safety

Nose Wheel Assembly:

Given the large ground reaction load, the contact patch regions can be assessed to yield the maximum deformation in the Nose Wheel Assembly per Figure 52. The result also indicates that plastic deformation (sustained stress is larger than yield strength) at the Inner Nose Wheel Half, more specifically the area near the interior bolt lugs and packing groove (Figure 51), where the Inner and Outer Nose Wheel Half are connected. The permanent deformation at this interface may potentially cause a slight leak to the tubeless tire. However, such detrimental effect can be easily identified and prevented through the routine ground inspection after an abnormal impact.

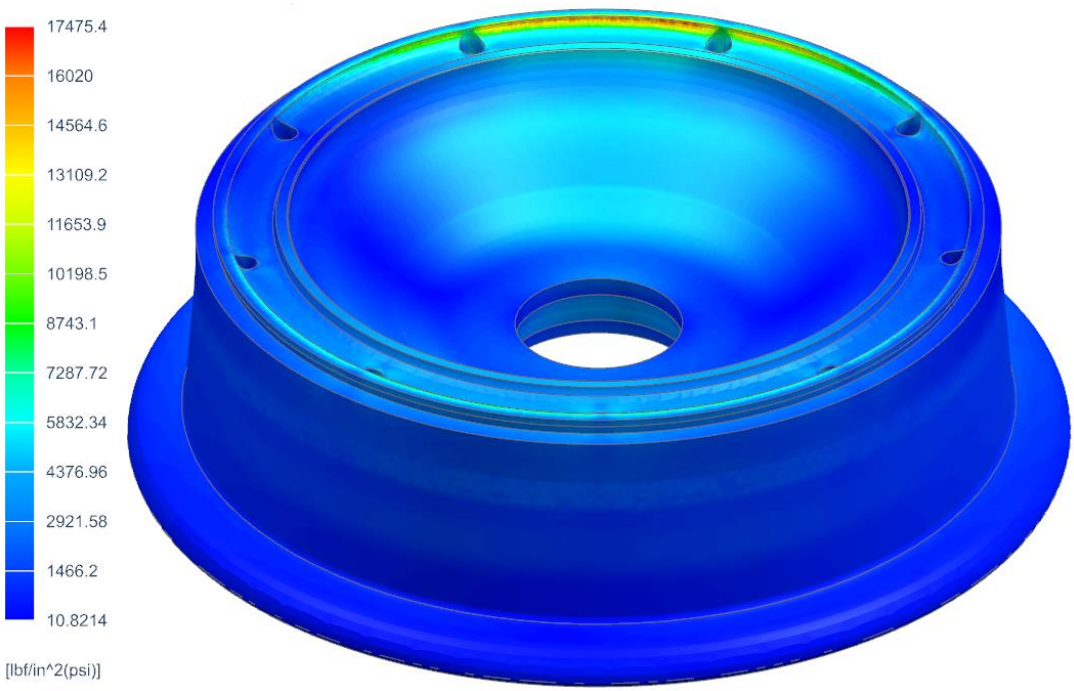

FIGURE 51: Plastic Deformation at Inner Nose Wheel Half

Subsequently, the maximum stress can be detected at the inner diameter of the Cone Bearing, where the majority of the ground reaction load transfer into the Axle and other components.

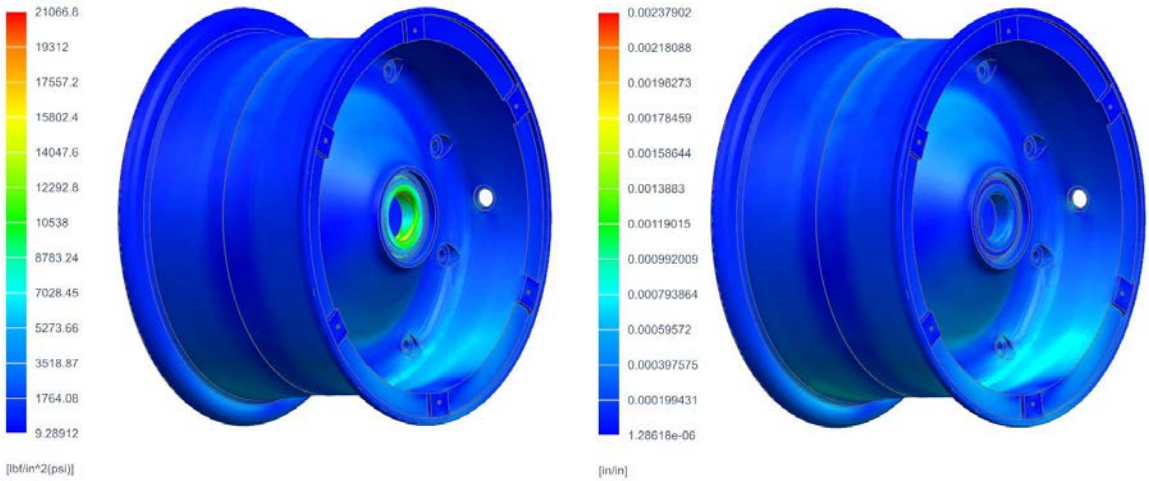

(A) **(B)**

PN	Time Step (ms)	Von Mises Stress (psi)	Strain (in/in)
Nose Wheel Assembly	15	8798	0.0010
	30	15201	0.0017
	45	18956	0.0022
	60	21067	0.0024

FIGURE 52: Stress (A) and Deformation (B) of Nose Wheel Assembly

Axle:

Due to the rigid connections with the Fork Assembly at the axle ends, the Axle is predominantly loaded in bending at the connected interface with the Nose Wheel Assembly, more specifically the contacted areas with the Cone Bearings. Figure 53 further validates this assessment by indicating that the maximum stress and deformation of the Axle happens in these areas.

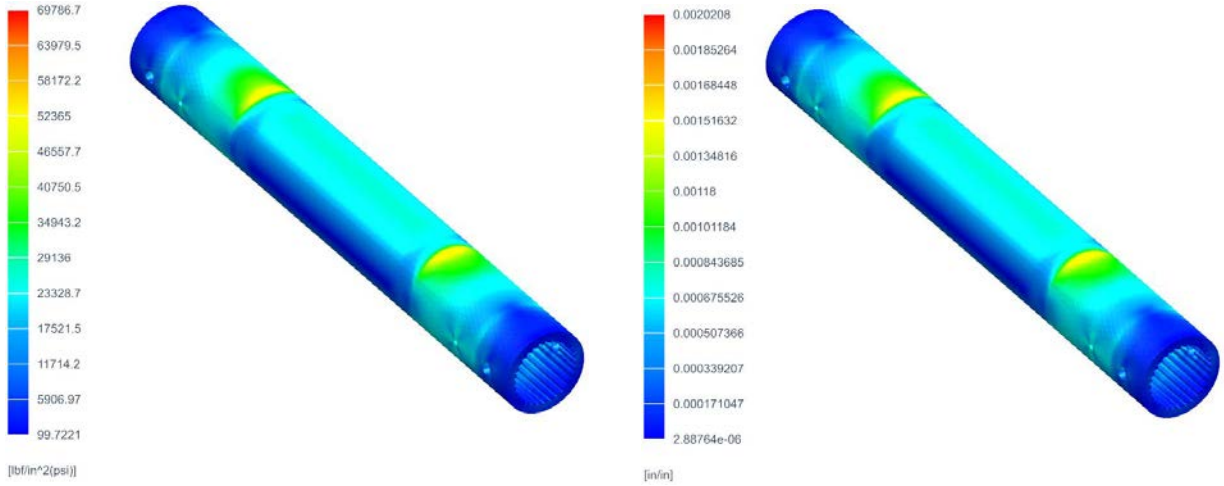

(A) **(B)**

PN	Time Step (ms)	Von Mises Stress (psi)	Strain (in/in)
Axle	15	29341	0.0009
	30	50470	0.0015
	45	62882	0.0018
	60	69787	0.0020

FIGURE 53: Stress (A) and Deformation (B) of Axle

Fork Assembly:

Due to the restriction in both radial and vertical direction from the Piston Tube, it can be assessed that the maximum stress of the Fork Assembly occurs at the Upper Bushing and nearby areas per Figure 53. Concurrently, the maximum deformation of the Fork Assembly can be detected near the upper shoulder and neck sections of the Fork.

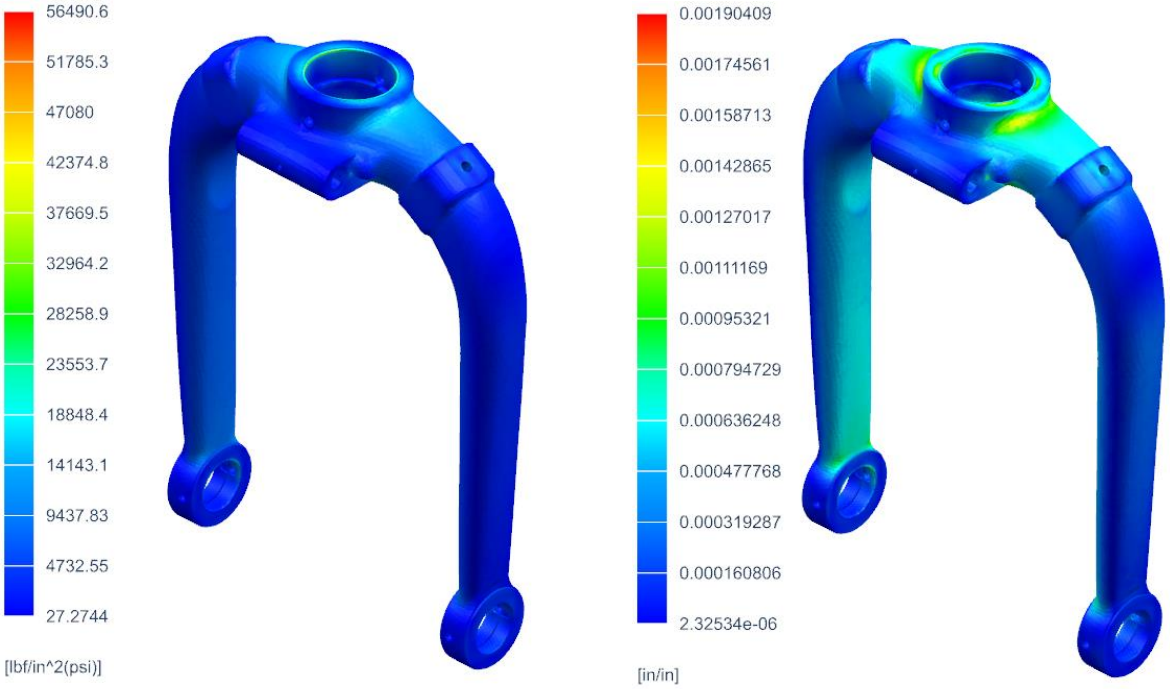

(A) **(B)**

PN	Time Step (ms)	Von Mises Stress (psi)	Strain (in/in)
Fork Assembly	15	23547	0.0008
	30	40751	0.0014
	45	50664	0.0017
	60	56491	0.0019

FIGURE 54: Stress (A) and Deformation (B) of Fork Assembly

Piston Tube:

Similar behavior in stress and deformation can be detected on Piston Tube at its mating interface with the Upper Bushing in the Fork Assembly (Figure 53). This observation further reinforces that the ground reaction load is properly transferred across the lower mass of the landing gear system given the restriction at the Piston Tube's top end per the initial assumption in Section 5.1.

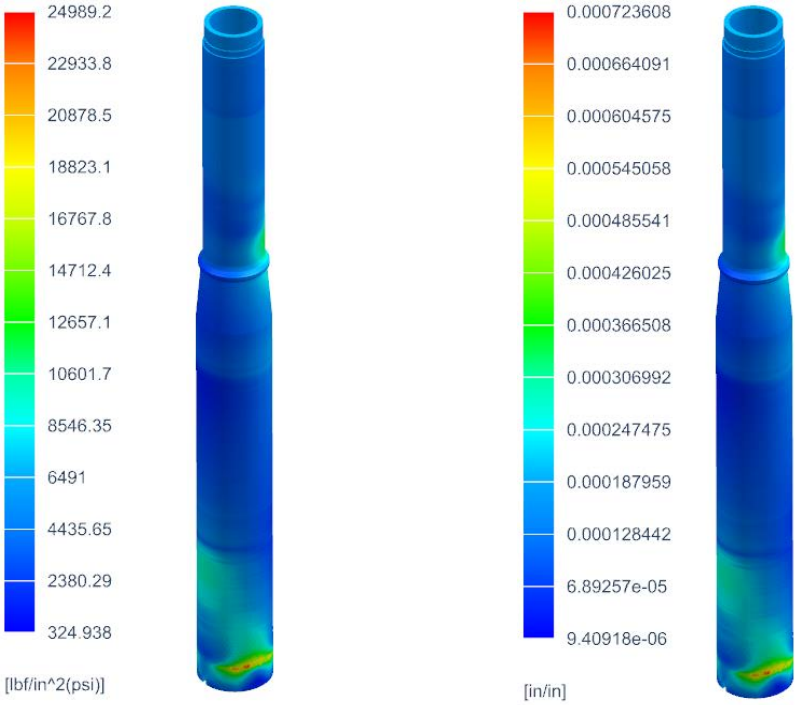

(A) **(B)**

PN	Time Step (ms)	Von Mises Stress (psi)	Strain (in/in)
Piston Tube	15	10454	0.0003
	30	18050	0.0005
	45	22422	0.0006
	60	24989	0.0007

FIGURE 55: Stress (A) and Deformation (B) of Piston Tube

Nut:

Given the structural support from Piston Tube and the pneumatic load at the upper chamber within the Cylinder, the maximum stress and deformation of the Nut can be detected at the threading area with Piston Tube and the top extruded slots, where a significant reduction of cross-sectional area happens (Figure 56).

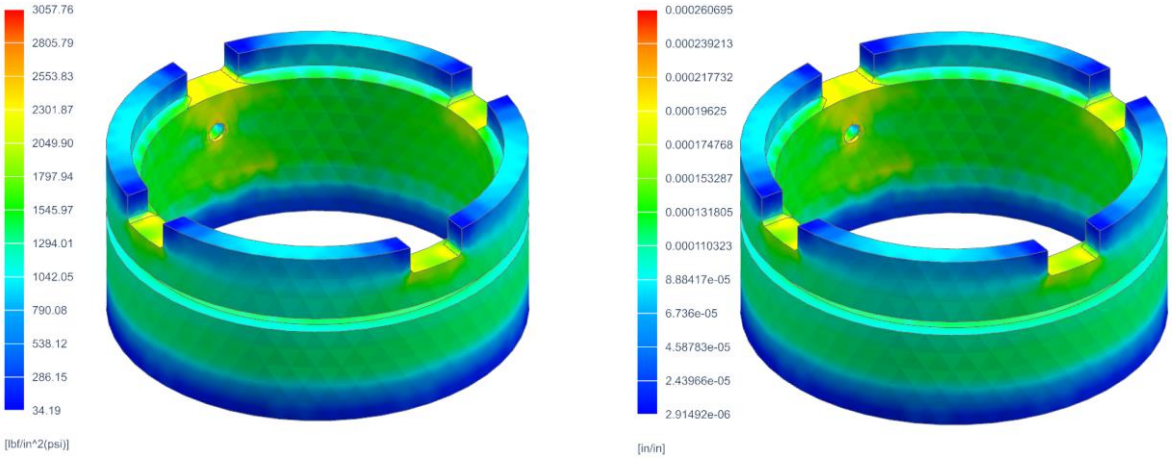

(A) **(B)**

PN	Time Step (ms)	Von Mises Stress (psi)	Strain (in/in)
Nut	15	2783	0.0002
	30	2825	0.0002
	45	2896	0.0003
	60	3058	0.0003

FIGURE 56: Stress (A) and Deformation (B) of Nut

Locknut:

By acting as a locking mechanism between the Piston Tube and the Fork Assembly, the maximum stress and deformation of the Locknut can be detected at the mounting holes and threading area with the Piston Tube (Figure 56). This observation further reinforces that the ground reaction load is properly transferred across all rigid connections within the Fork Assembly/Piston Tube/Lock Nut contact interface.

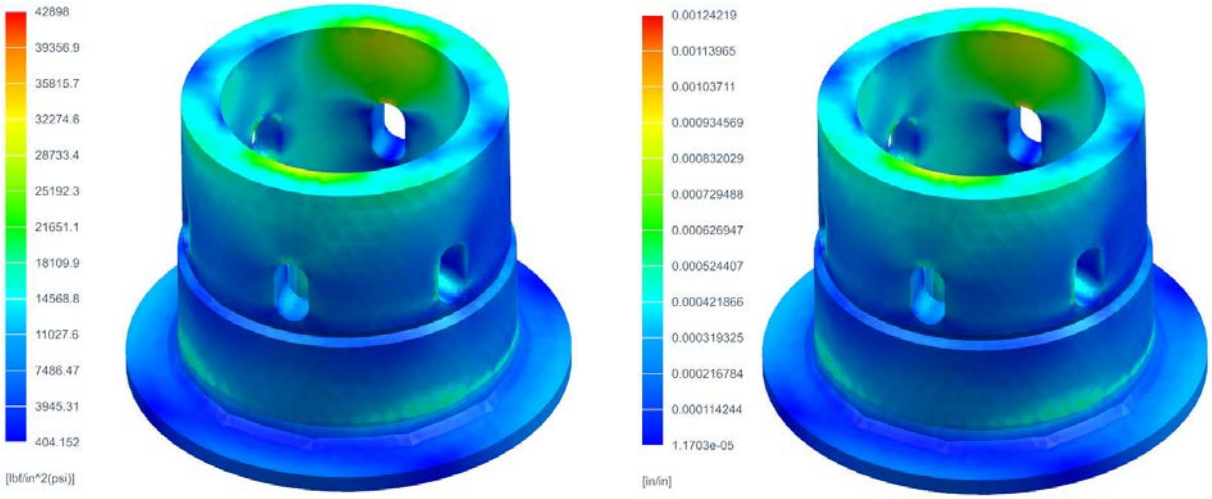

(A) **(B)**

PN	Time Step (ms)	Von Mises Stress (psi)	Strain (in/in)
Locknut	15	17879	0.0005
	30	30946	0.0009
	45	38479	0.0011
	60	42898	0.0012

FIGURE 57: Stress (A) and Deformation (B) of Locknut

Stack-up of Floating Piston, Bumper, and Shoulder:

The result in Figure 58, 59, and 60 indicates that the Floating Piston/Bumper/Shoulder stack-up only experience low stress and have a high factor of safety. This falls in line with their respective failure modes, which are corrosion, wear, and heat damages rather than structural failures like cracking. The dampening effect from the bumper can also be detected based on the differences in stress and deformation within the Bumper's steel rings.

For the Floating Piston, the maximum stress and deformation occur at the contact area with Cylinder Assembly due to the normal contact forces. As for the Bumper and Shoulder, the maximum stress and deformation occur at their respective contact interface with their mating components within the stack-up.

This observation further reinforces that the impact forces are properly transferred from the lower mass of the landing gear system, more specifically the Piston Tube, to through the stack-up and transfer to the upper mass, more specifically the Cylinder Assembly.

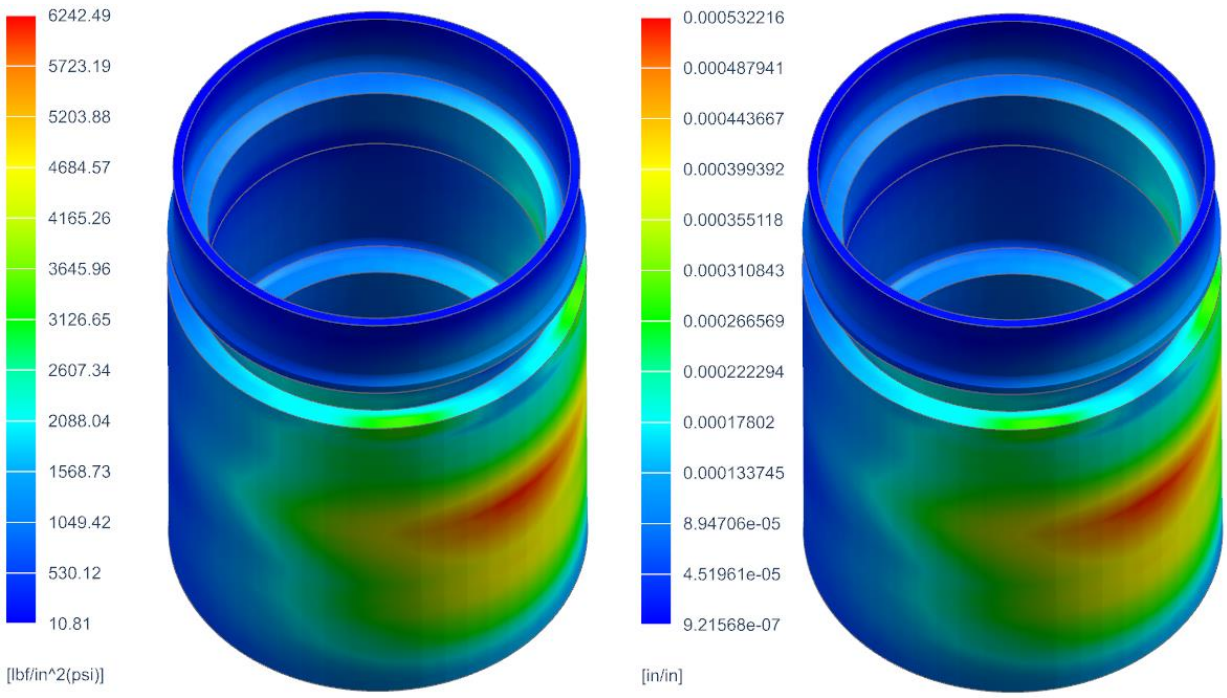

(A) **(B)**

PN	Time Step (ms)	Von Mises Stress (psi)	Strain (in/in)
Floating Piston	15	3231	0.0003
	30	4866	0.0004
	45	5761	0.0005
	60	6243	0.0005

FIGURE 58: Stress (A) and Deformation (B) of Floating Piston

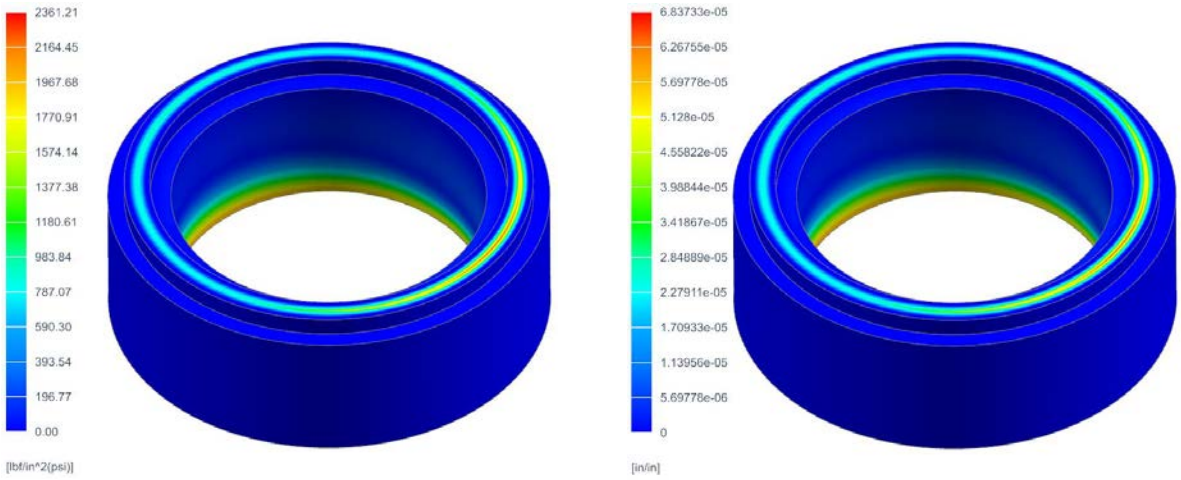

(A) **(B)**

PN	Time Step (ms)	Von Mises Stress (psi)	Strain (in/in)
Bumper	15	1941	0.0001
	30	2192	0.0001
	45	2318	0.0001
	60	2361	0.0001

FIGURE 59: Stress (A) and Deformation (B) of Bumper

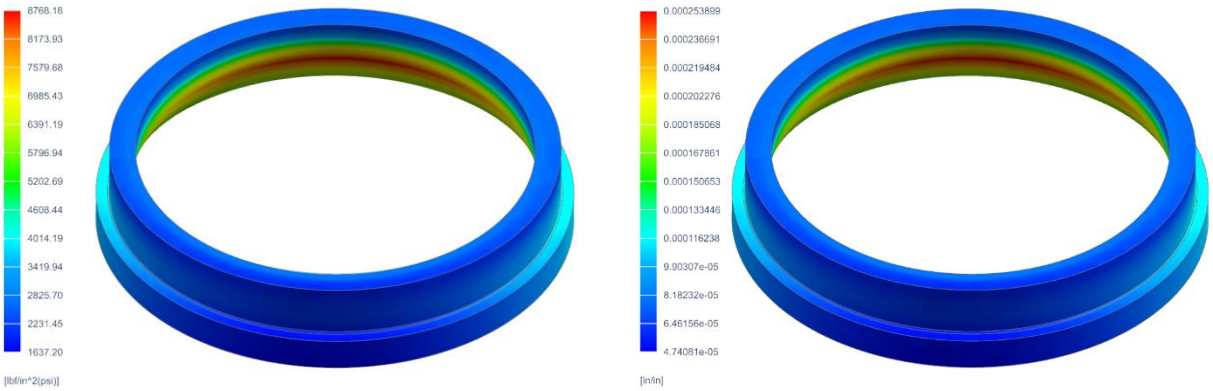

(A) **(B)**

PN	Time Step (ms)	Von Mises Stress (psi)	Strain (in/in)
Shoulder	15	5643	0.0001
	30	7274	0.0002
	45	8198	0.0002
	60	8768	0.0003

FIGURE 60: Stress (A) and Deformation (B) of Shoulder

Cylinder Assembly:

Acting as the main connection to the aircraft fuselage, the Cylinder Assembly is predominantly loaded at the mounting protrusion and the bolt holes. This is due to the large compression force caused by the lower mass of the landing gear system under the impact. Figure 61 further validates this assessment by indicating that the maximum stress and deformation of the Cylinder happens in these areas.

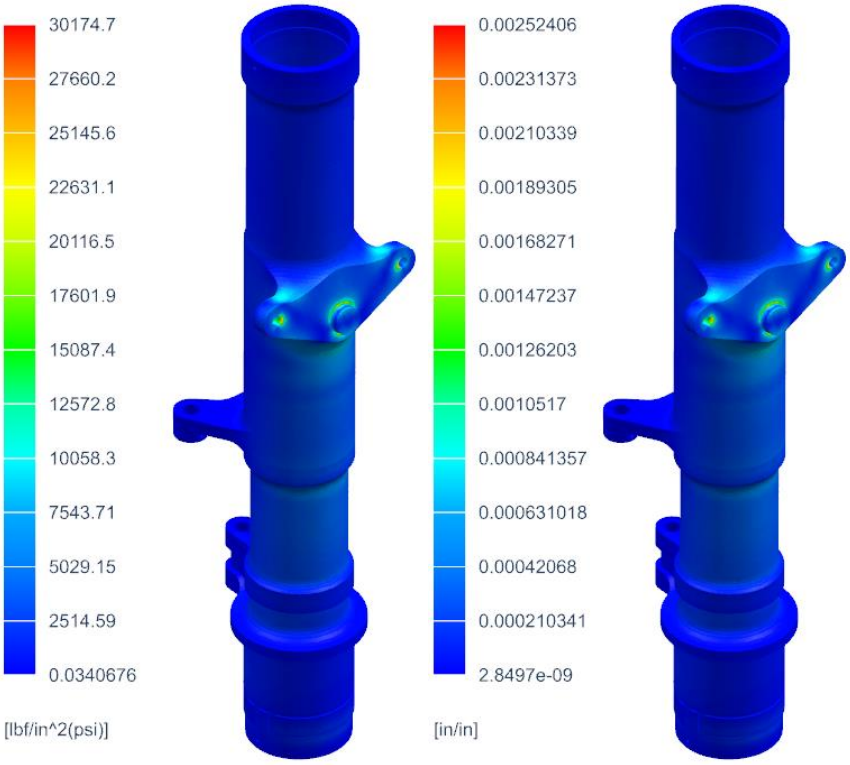

(A) **(B)**

PN	Time Step (ms)	Von Mises Stress (psi)	Strain (in/in)
Cylinder	15	15068	0.0013
	30	23570	0.0020
	45	28078	0.0023
	60	30175	0.0025

FIGURE 61: Stress (A) and Deformation (B) of Cylinder

The effect of upper normal contact force can be detected in the lower portion of the Sleeve, where the Floating Piston slides against due to the large deflection of the lower mass, given the concentrated high stress and deformation (Figure 62). The result also indicates that the Sleeve only experiences low stress and has a high factor of safety. This is further reinforced due to the primary function of the Sleeve, which provides protection to the cylinder pneumatic area against corrosion, wear, and heat damages.

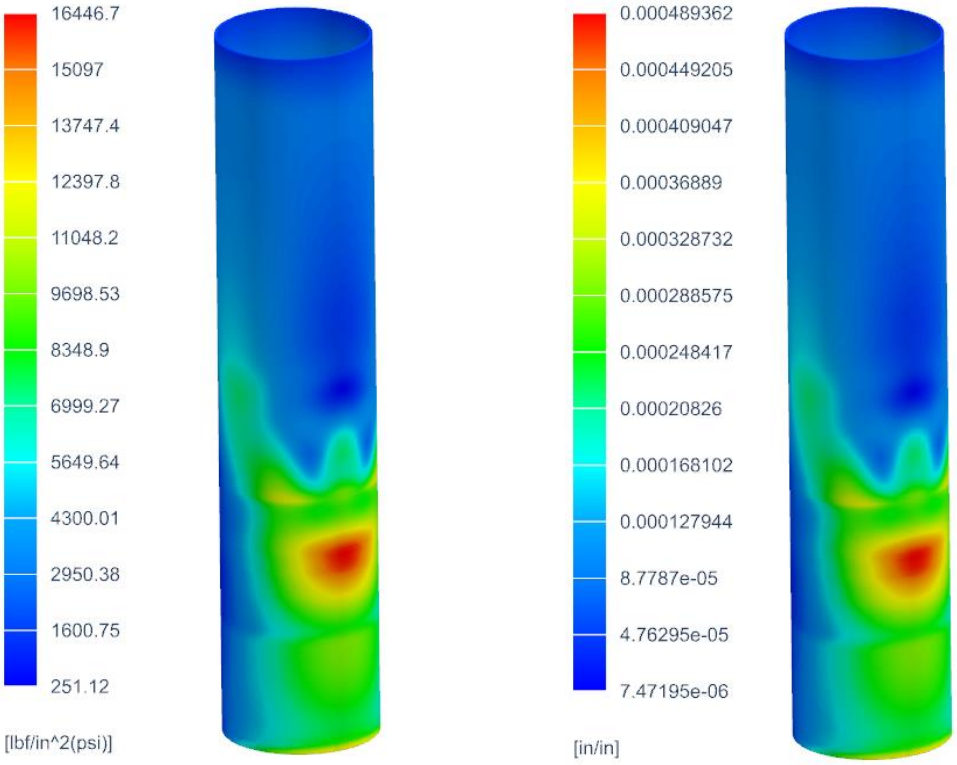

(A) **(B)**

PN	Time Step (ms)	Von Mises Stress (psi)	Strain (in/in)
Sleeve	15	8465	0.0003
	30	12742	0.0004
	45	15106	0.0004
	60	16447	0.0005

FIGURE 62: Stress (A) and Deformation (B) Sleeve

Journal Bearing:

The maximum stress and deformation of the Journal Bearing can be detected at its lower portion, where the Piston Tube slides against due to the large deflection of the lower mass. This further validates the effect of lower normal contact force from the Piston Tube to the upper mass. The result also indicates that the impact forces are properly transferred from the lower mass of the landing gear system to the surrounding structures. Similar to the Sleeve, the Journal Bearing only experiences low stress and has a high factor of safety given its primary function, which provides protection to the cylinder lower portion against corrosion and wear damages.

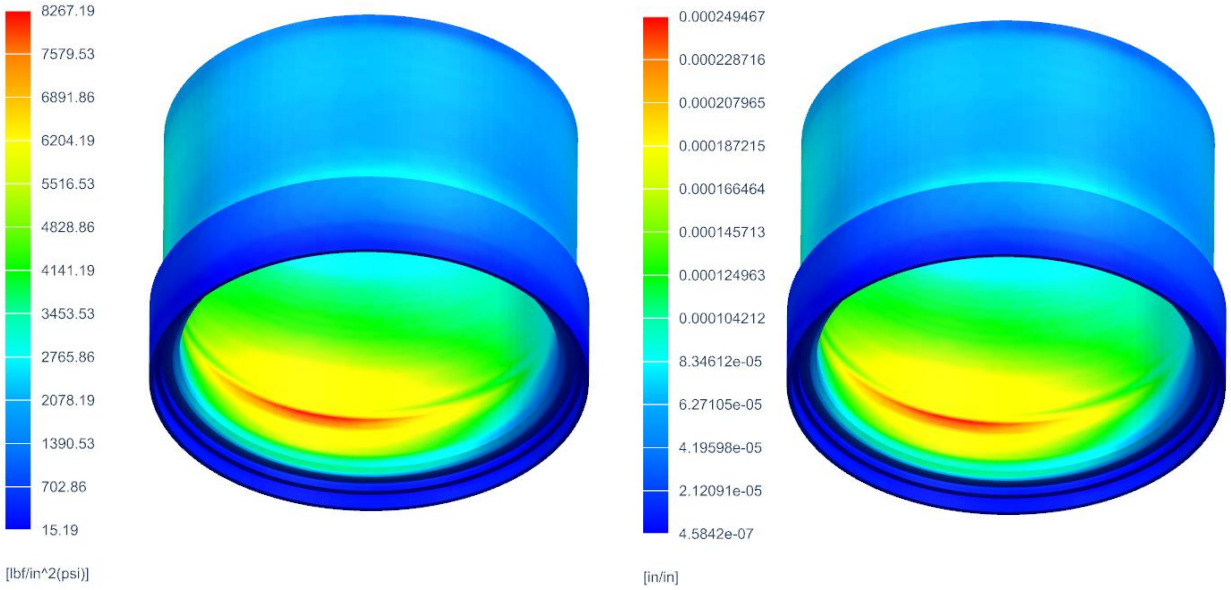

(A) **(B)**

PN	Time Step (ms)	Von Mises Stress (psi)	Strain (in/in)
Journal Bearing	15	3592	0.0001
	30	6053	0.0002
	45	7451	0.0002
	60	8267	0.0003

FIGURE 63: Stress (A) and Deformation (B) of Journal Bearing

7.0 Conclusions and Continuation Considerations

With the formulation of a methodology to assess the maximum impact loading condition for a landing gear system has been achieved, the satisfaction of this thesis's objective has also been obtained. Herein, the analysis methodology for determination of stress and deformation behavior of the Twin Otter nose landing gear herein are reproducible for other similar landing gear systems. It is recommended that during the early stage of design, the following steps be taken:

1. The interaction of each component within the landing gear must be identified and studied
2. The theoretical analysis of the worst-case loading scenario occurring when the shock absorber is fully compressed must be properly derived and satisfied the FAA regulations and engineering requirements
3. Assumptions, boundary conditions, constraints, and loads must be clearly substantiated and determined for appropriate modeling setup

A comprehensive summary of the analysis methodology can then be standardized and formulated to provide a guiding instruction for analyzing and optimizing the open geometry of other landing gear systems. This will also help establish an adequate FEM, which is conformed to the industrial/FAA's standards and that can be utilized in determining the stress and deformation behavior of the landing gear during landing for both small and large aircrafts. Engineers and scientists can then utilize the analysis methodology outlined herein to help determine if the subjected designs have complied with the FAA's airworthiness regulations and requirements

prior to performing shock absorption testing. Design alterations can also be made prior to manufacturing and testing, which will significantly reduce the cost and time of development.

For ease of implementing this analysis methodology to other landing gears system, the block diagram in Figure 64 (completed section - in blue) can be utilized. Overall, the methodology places a heavy emphasis on two major areas: establishment of loading condition and airworthiness validation.

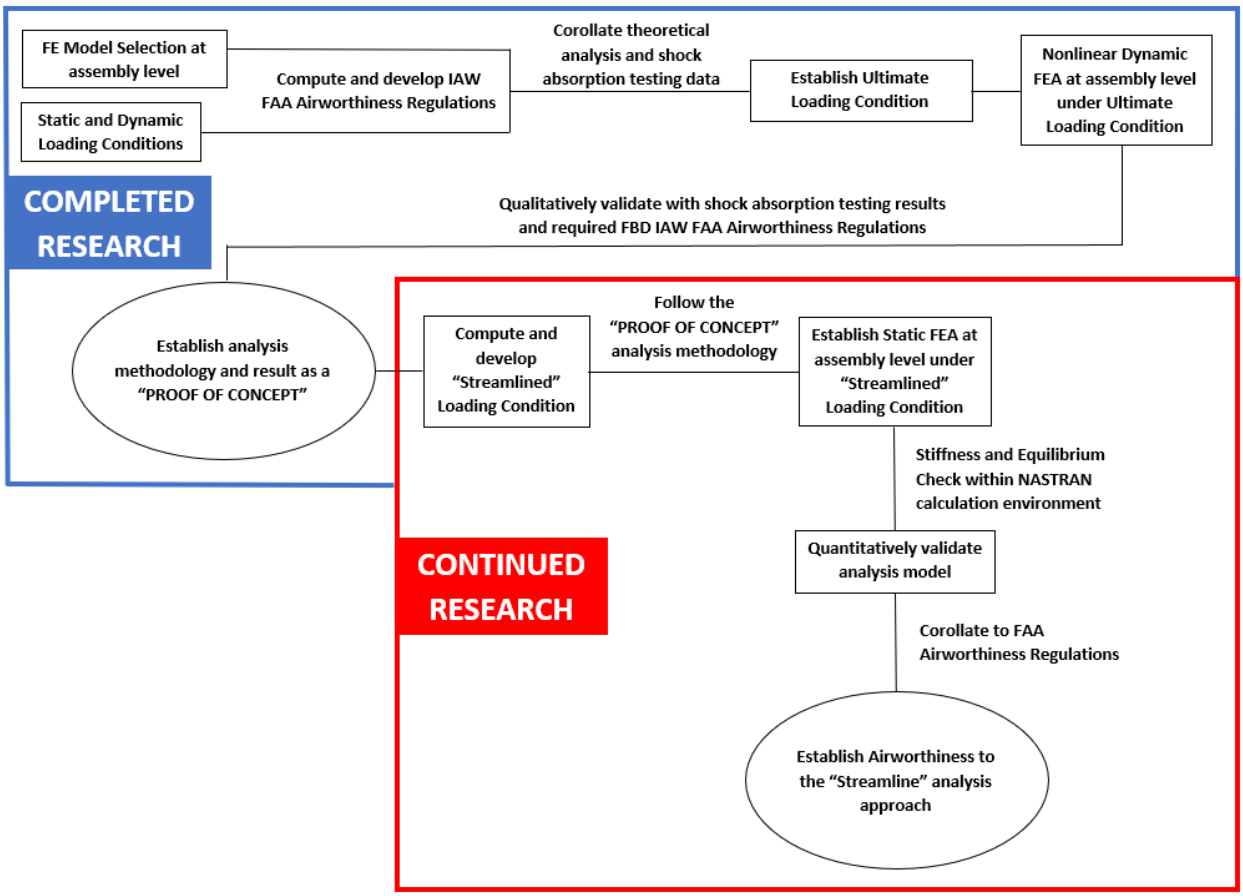

FIGURE 64: Block Diagram

As reference in Section 2.0, most of the earlier work found related to this research originates from Thoai Nguyen's study [2], John C. Stearns' investigation [3], and Benjamin Milwitzky and Francis E. Cook's report [4]. By utilizing such foundation as a basis of knowledge,

the comprehensive analysis methodology herein can then summarize all previous technical discussions and introduce the additional research criteria and considerations. Those criteria and considerations, in turn, further expand and advance this research applicability to the aerospace industry and can be outlined as follows:

- Proper modeling selection must be appropriately implemented
- The nonlinearity nature of material must be appropriately address and substantiated
- All loading and boundary conditions must be thoroughly investigated and developed IAW FAA Airworthiness Regulations
- The Finite Element Method must be appropriately established and understand, most specifically on nonlinearity determination and meshing selection
- Validation method must be introduced and satisfied FAA Airworthiness Regulations

As previously mentioned in Section 4.9.4, 4.10.1, and 4.10.2, the obtained FEA results in this thesis specifically corollate to a condition where testing has been performed. Additionally, the validation procedure detailed in Section 6.3 is only a qualitative method, which is recommended by the FAA to provide a mean to assess the sensitivity of the FEA results against the expected behavior of a real structure under the conservation loading condition. By further correlating them with the empirical results in Table 3, the FEA results in Section 6.0 can be determined as reasonably accurate and the methodology herein can be established as a proof of concept for the loading and boundary conditions. This methodology can then be implemented for all general cases in the preliminary design stage, where testing data is not readily available.

In some cases, the study herein may still be too computational complex and expensive given the required level of details in the overall analysis with contact conditions and constitutive model of Hyperelastic. Additionally, the validation process still relies too heavily on the testing data, which is also not available in most cases. This results in a further desire for a simpler analysis with a quantitative validation procedure as discussed in Section 6.3. The validation process can then be independently performed with no need for the correlation with testing results. The overall finite element method can then be further streamlined for a more preliminary analysis that is applicable for most landing gear systems in the very early designing cycle.

A derivative Nonlinear Static Analysis condition of the current Finite Model can then be derived to incorporate the mentioned validation process above. The continuation of this research shall be performed as highlighted within the block diagram in Figure 64 (continued section - in red) with the following conditions:

Condition	Comment
Vertical Reaction Load	5317.26 lbs per the estimated limit drop condition IAW CAR 3.243, 3.352. Correlated to a Bead Seat and Rim Flange pressure of 625.34 psi See Section 4.3 for more info
Pneumatic Load	1454.60 psi per the estimated fully compressed state (semi-crash landing). See Section 4.10.1 for more info
Hydraulic Load	2650.13 psi per the estimated fully compressed state (semi-crash landing). See Section 4.10.2 for more info
Quantitative Validation	As discussed in Section 6.3, a quantitative validation process can be performed by verifying that equilibrium in forces between OLOAD and SPCFORCE. A detailed NASA Contractor Report with Lockheed Engineering [25] can also be utilized as general guidance for the acceptance criteria

TABLE 10: Elements Descriptions

References

[1] "The Oleo Story," OLEO International, [Online]. Available: https://www.oleo.co.uk/about/story. [Accessed 2019].

[2] T. D. Nguyen, "Finite Element Analysis of a Nose Landing Gear During Landing," *UNF Theses and Dissertations,* p. 215, 2010.

[3] J. C. Stearns, "An Investigation of Stress and Displacement Distribution in an Aluminum Alloy Automobile Rim," The Graduate Faculty of the University of Akron, 2000.

[4] B. Milwitzky and F. E. Cook, "Report 1154: Analysis of Landing-Gear Behavior," National Advisory Committee for Aeronautics, 1953.

[5] W. W. Brixius, "Traction Prediction Equations for Bias Ply Tires," American Society of Agricultural Engineers - Paper No. 87-162, Michigan, 1987.

[6] Aircraft Tire Data Book, Goodyear Aviation, 2002.

[7] S. T. Chai and W. H. Mason, "Landing Gear Integration in Aircraft Conceptual Design," Multidisciplinary Analysis and Design Center for Advanced Vehicles, Virgina Polytechnic Institute and State University Blacksburg, 1996.

[8] N. S. Currey, Aircraft Landing Gear Design: Principles and Practices, American Institute of Aeronautics and Astronautics, 1988.

[9] S. E. Benzley, E. Perry, K. Merkley and B. Clark, "A Comparision of All Hexagonal and All Tetrahedral Finite Element Meshes for Elastic and Elasto-plastic Analysis," Bringham Young University, 1995.

[10] M. A. Hassan, A. Abouel-Kasem, M. A. El-Sharief and F. Yusof, "Evaluation of the Material Constants of Nitrile Butadeine Rubbers (NBR) with Different Carbon Black (CB): FE-Simulation and Experimental," Faculty of Engineering Assiut University - Mechanical Engineering Department, 2009.

[11] M. Shahzad, A. Kamran, M. Z. Siddiqui and M. Farhan, "Mechanical Characterization and FE Modelling of a Hyperelastic Material," Advance Material Research Directorate, Space and Upper Atmosphere Research Commission - Institute of Space Technology, 2015.

[12] Civil Air Regulations Part 3 - Airplane Airworthiness; Normal, Ultility, and Acrobatic Catergories, Washington, D.C: Civil Aeronautics Board, 1956.

[13] Type Certificate Data Sheet No. A9EA Revision No. 20, Department of Transportation - Federal Aviation Administration, 2016.

[14] DHC 6 - Twin Otter (Series 400) Weight and Balance Manual PSM 1-64-8, Viking Air, 2018.

[15] KAron Design Guide, Kaman Aerospace.

[16] NX Nastran 10 - Advance Nonlinear Theory and Modeling Guide, Siemens, 2014.

[17] Element Library Reference, Siemens.

[18] V. R. L. P. Bahadursha, "Tearing of Styrene Butadiene Rubber using Finite Element Analysis," The Graduate Faculty of the University of Akron, 2015.

[19] "FEMAP V10.1 & NX Nastran 6.1 Solid Elements Tutorial u/p 27-Nodes," Iberisa, [Online]. Available: http://iberisa.com/soporte/femap/nolinealavanzado/brick27nodos.htm. [Accessed 2019].

[20] "Mesh Quality Checks," Dassault Systemes - Solidworks, [Online]. Available: http://help.solidworks.com/2016/english/solidworks/cworks/c_mesh_quality_checks.htm. [Accessed 2019].

[21] "Finite Element Aspect Ratio Influence in Concrete Foundation Models," StructurePoint, [Online]. Available: https://www.structurepoint.org/publication/pdf/Finite-Element-Aspect-Ratio-Influence-In-Concrete-Foundation-Models.pdf. [Accessed 2019].

[22] Siemens Corporate Technology, "Nastran Element Quality Checks," Siemens, [Online]. Available: http://www2.me.rochester.edu/courses/ME204/nx_help/index.html#uid:xid452984_v1. [Accessed 2019].

[23] "Mesh Control Definitions and General Enhancements," Siemens, [Online]. Available: http://www2.me.rochester.edu/courses/ME204/nx_help/index.html#uid:xid597367. [Accessed 2019].

[24] P. Safarian, "Finite Element Modeling and Analysis Validation," Federal Aviation Administration (FAA), Washington.

[25] A. E. Stockwell, "NASA Contractor Report 4675: A Verification Procedure for MSC/NASTRAN Finite Elements Models," National Aeronautics and Space Administration (NASA), Virginia, 1995.

Appendix A: FAA Approved Drop Test Report

THIS PAGE INTENTIONALLY LEFT BLANK

Section 2: Required Testing

Per the test plan, Removed, the following testing was required:

Applicable Regulation	Test Condition	Configuration	Required Load (lbs)	Pass/Fail Criteria
CAR 3.255	Static Vertical and Forward Load	PMA Design Nose Fork	4113 Vertical 1645 Forward	No Failure No Permanent Set
CAR 3.256	Static Vertical and Side Load	PMA Design Nose Fork	4113 Vertical 2879 Side	No Failure No Permanent Set
CAR 3.254	Static Vertical and Aft Load	PMA Design Nose Fork	4113 Vertical 3290 Drag	No Failure No Permanent Set
CAR 3.351-3.354	Limit Dynamic Drop Test 18.7" Vertical Drop	PMA Design Nose Fork	1326*	No Failure No Permanent Set Comparison to OEM Fork
CAR 3.243, 3.351-3.354	Limit Dynamic Drop Test 18.7" Vertical Drop	OEM Fork	1326*	No Failure No Permanent Set
CAR 3.352 (b) and 3.355	Reserve Energy Dynamic Drop Test 26.9" Vertical Drop	PMA Design Nose Fork	1229*	No Failure No Permanent Set

* Note: Based on total deflection (d) value of 13.1". Actual Value found to be lower and PMA Design fork was tested to higher load values.

1. Forward, Side and Aft Load Testing

   Application of the forward, side and aft load components were completed by means of a ramp. A greased sliding plate was used to minimize the impact of friction on the applied horizontal load. The ramp angle calculation was taken from the test plan and is shown below:

The vertical and horizontal loads were applied simultaneously, increasing both continuously. The maximum applied vertical load was recorded and is shown in the test results for all conditions. The tire zero point, initial tire contact, was checked before and after each test condition to ensure that no permanent set occurred. The test condition was held for a minimum of 5 seconds and photos were taken of each condition.

2. Limit Dynamic Drop Testing

Comparison testing was completed per the approved test plan to verify no change in the dynamic characteristics of the shock strut assembly between the OEM fork and the PMA Design fork. In addition, the total deflection value (d) was recalculated based on actual test results and the PMA Design fork was retested at the increase drop weight to verify the limit load factor per CAR 3.354. The testing in all cases was performed at a drop height of 18.7", the maximum required. The limit drop weight was calculated as follows:

$$W_e = W_N * \left(\frac{h + (1 - L) * d}{h + d} \right)$$

Where:

W_n = 1828 lbs

h = 18.7"

d = 13.11" (used for initial estimate and comparison testing)

d = 8.95" (used for additional testing on PMA Design fork)

L = 0.667

$$W_e = (1826\,lbs) \times [\frac{18.7\text{in} + (1 - 0.667) \times 13.11\text{in}}{18.7\text{in} + 13.11\text{in}}] = 1326\,lbs$$ Comparison Testing

$$W_e = (1826\,lbs) \times [\frac{18.7\text{in} + (1 - 0.667) \times 8.5\text{in}}{18.7\text{in} + 8.5\text{in}}] = 1445\,lbs$$ Additional Testing on PMA fork

3. Reserve Energy Dynamic Drop Testing

Proof of strength testing was completed per CAR 3.355 for the PMA Design fork only.

$$W_e = W \frac{h}{h + d}$$

$$W_e = (1826\,lbs) \times [\frac{26.9\text{in}}{26.9\text{in} + 9.0\text{in}}] = 1368\,lbs$$

Section 4: Instrumentation

	Position Transducer (carriage)	Load Cell	Digital Readout	Accelerometer	ADC
Manufacturer	MTS	Transducer Techniques	Transducer Techniques	Measurement Specialties	Measurement Computing
Part Number	EP2A-048	SWO-10K	SSI	15200B	USB-1608G 151440B-01L
Serial Number	90442935	274198	281193	NA	1729917
Range	48 inches	10000 lbs.	Variable	Variable (10-70g)	0-10 volts (adjustable)
Output	0 – 10 VDC	2.36 mV/V at 10000 lbs	Visual	RS-485	NA
Resolution	.0024	+/- 2.5 lbs	Based on Load Cell	16-bit	16-bit

All data for the dynamic drop testing was recorded at 1000 samples per second and recorded via the 16-bit ADC to a laptop computer. Static testing was completed by visually checking the SSI load cell display and holding the applied load for at least five seconds. Calibrations are provided in Appendix A.

Completed Test Matrix

Twin Otter Nose Gear Drop Test Requirements and Results

Run	Configuration	CAR Requirement	Applied Load (lbs)	Carriage Height (inches)	Tire Pressure/Strut Pressure (psi)	Maximum Deflection (d in Inches)	Maximum Recorded Load Factor (nj)	Impact Velocity (ft/sec)
1	OEM Nose Gear Assembly	NA, Build up test	1335	0.0	32/95	7.80	1.8	2.3
2	OEM Nose Gear Assembly	NA, Build up test	1335	5.2	32/95	8.00	2.06	5.2
3	OEM Nose Gear Assembly	NA, Build up test	1335	10.0	32/95	8.16	2.94	7.2
4	OEM Nose Gear Assembly	NA, Build up test	1335	15.1	32/95	8.47	3.69	8.7
5	OEM Nose Gear Assembly	limit test	1335	19.3	32/95	8.95	4.28	9.9
6	PMA Design Nose Gear Assembly	NA, Build up test	1335	0.1	32/95	8.14	NA	2.2
7	PMA Design Nose Gear Assembly	NA, Build up test	1335	5.0	32/95	8.30	NA	5.4
8	PMA Design Nose Gear Assembly	NA, Build up test	1335	10.2	32/95	8.54	2.98	7.4
9	PMA Design Nose Gear Assembly	NA, Build up test	1335	15.0	32/95	8.84	3.7	8.2
10	PMA Design Nose Gear Assembly	limit comparison	1335	19.1	32/95	9.07	4.26	9.7
11	PMA Design Nose Gear Assembly	limit comparison	1335	19.0	32/95	9.10	4.28	9.8
12	PMA Design Nose Gear Assembly	limit test	1486	19.5	32/95	9.10	4.3	9.9
13	PMA Design Nose Gear Assembly	limit test	1486	19.2	32/95	9.90	4	9.9
14	PMA Design Nose Gear Assembly	limit test	1486	19.2	32/95	9.91	4.04	9.9
15	PMA Design Nose Gear Assembly	Static Fwd	4190	NA	32/95	NA	NA	NA
16	PMA Design Nose Gear Assembly	Static Side	4216	NA	32/95	NA	NA	NA
17	PMA Design Nose Gear Assembly	Static Drag	4209	NA	32/95	NA	NA	NA
18	PMA Design Nose Gear Assembly	NA, Build up test	1376	5.0	32/95	8.6	2.0	4.6
19	PMA Design Nose Gear Assembly	Reserve Energy	1376	27.8	32/95	-10.06	5.3	11.8

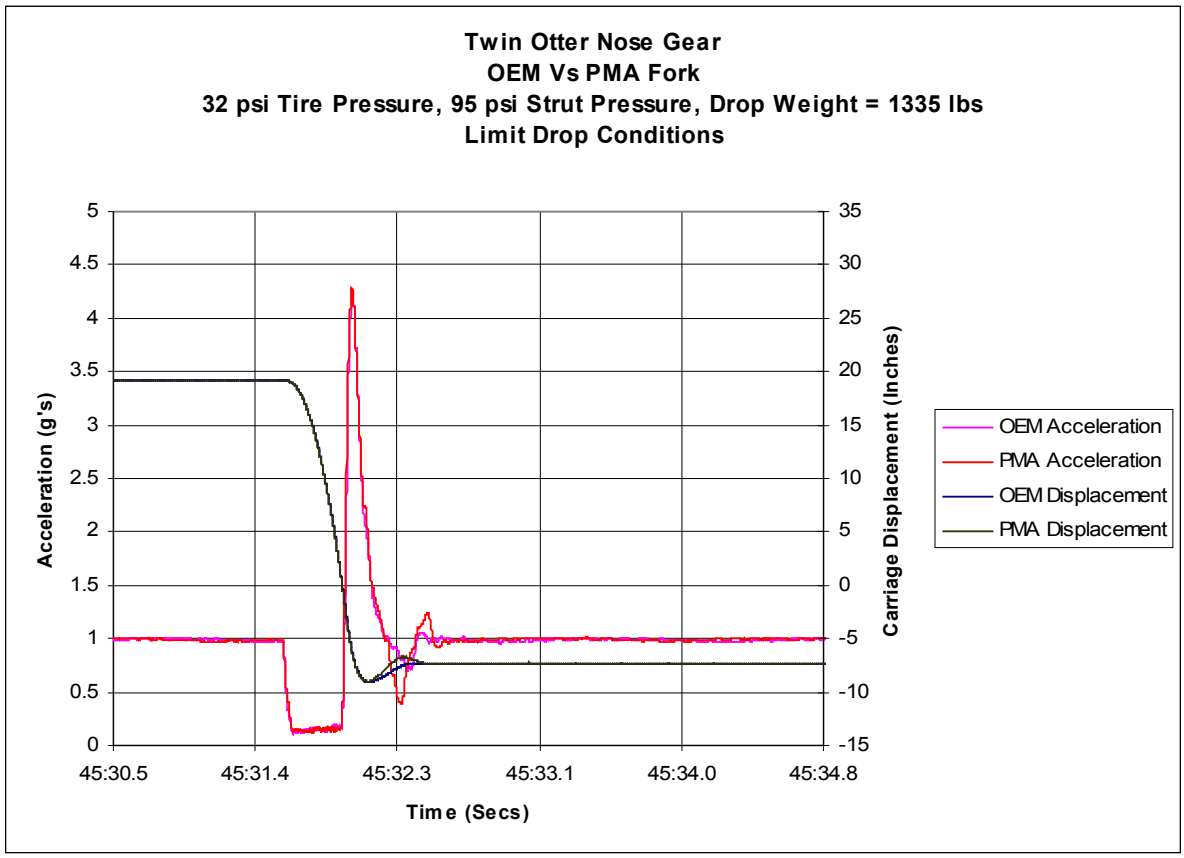
Twin Otter Nose Gear
OEM Vs PMA Fork
32 psi Tire Pressure, 95 psi Strut Pressure, Drop Weight = 1335 lbs
Limit Drop Conditions
Acceleration (g's)
Carriage Displacement (Inches)
Time (Secs)
5
4.5
4
3.5
3
2.5
2
1.5
1
0.5
0
35
30
25
20
15
10
5
0
-5
-10
-15
45:30.5
45:31.4
45:32.3
45:33.1
45:34.0
45:34.8
OEM Acceleration
PMA Acceleration
OEM Displacement
PMA Displacement

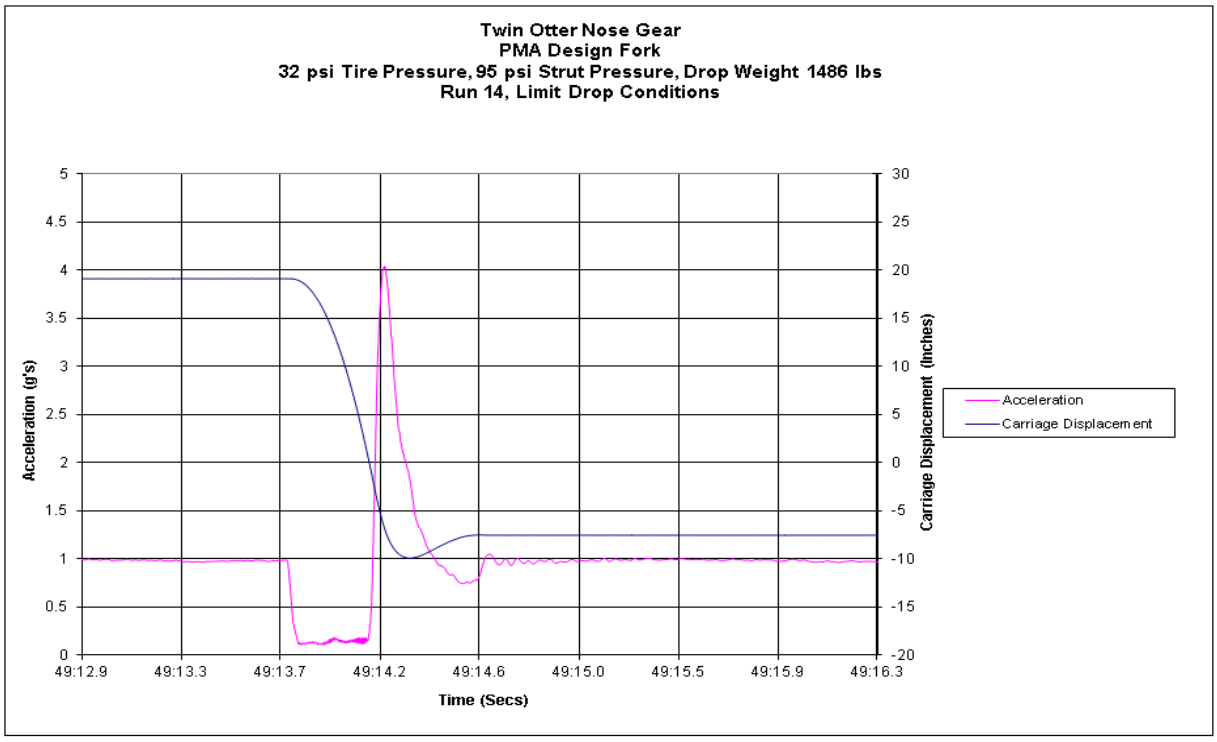
Twin Otter Nose Gear
PMA Design Fork
32 psi Tire Pressure, 95 psi Strut Pressure, Drop Weight 1486 lbs
Run 14, Limit Drop Conditions
Acceleration (g's)
Carriage Displacement (Inches)
Time (Secs)
Acceleration
Carriage Displacement
5
4.5
4
3.5
3
2.5
2
1.5
1
0.5
0
30
25
20
15
10
5
0
-5
-10
-15
-20
49:12.9
49:13.3
49:13.7
49:14.2
49:14.6
49:15.0
49:15.5
49:15.9
49:16.3

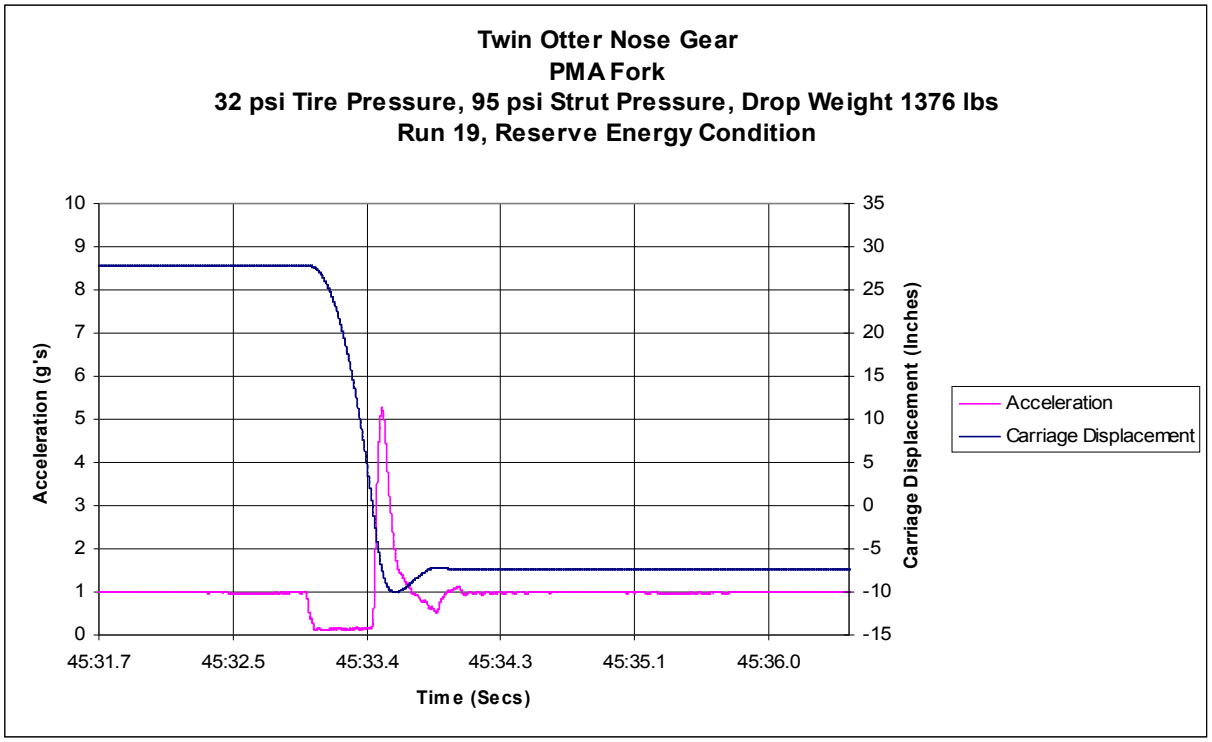
Twin Otter Nose Gear
PMA Fork
32 psi Tire Pressure, 95 psi Strut Pressure, Drop Weight 1376 lbs
Run 19, Reserve Energy Condition
Acceleration (g's)
Carriage Displacement (Inches)
Time (Secs)
Acceleration
Carriage Displacement
10
9
8
7
6
5
4
3
2
1
0
35
30
25
20
15
10
5
0
-5
-10
-15
45:31.7
45:32.5
45:33.4
45:34.3
45:35.1
45:36.0

Section 6: Test Photos

Figure 2: Test Installation

Figure 3: Shock Strut Data Plate

Figure 4: Tire and Wheel Assembly

Figure 5: PMA Fork, Fwd Load Condition

Figure 6: PMA Fork, Side Load Testing

Figure 7: PMA Fork, Aft Load Testing

Appendix B: FAA Approved Pull Test Report

THIS PAGE INTENTIONALLY LEFT BLANK

Sample 001

Version PV7.60/MV2.07 Test code: 61004
Serial Number: 80SIC1072
Tension General Purpose
Number of Specimens: 4 / 5
Sample type: DURO A 50 50 50 50 50
Method used: ASTM D 412
User text: AB
Loadcell: 1000N 100kgf 200lbf (Range: 10000 psi)
Extension measured by: high extensometer (Gauge Length 1.0000 in)
Stage 1 speed: 20.00 in/min
Recalculate extension: Disabled

Specimen details

	Width in	Thickness in	Area in²	Range lbf	Utilisation %
Specimen 1	0.2500	0.0820	0.0205	200	102.5
Specimen 2	0.2500	0.0800	0.0200	200	100.00
Specimen 3	0.2500	0.0820	0.0205	200	102.5
Specimen 4	0.2500	0.0840	0.0210	200	105.0

Specimen results

	Peak Stress psi	Peak Strain %	Mod @ 50% psi	Mod @ 100% psi	Mod @ 200% psi	Mod @ 300% psi
Specimen 1	1409.1	614.37	119.83	155.30	252.36	394.60
Specimen 2	1230.5	604.63	122.49	158.85	253.53	393.83
Specimen 3	1383.8	593.50	125.18	165.01	272.45	427.73
Specimen 4	1226.2	591.63	119.59	155.20	251.25	391.08

Multi-specimen results

	Peak Stress psi	Peak Strain %	Mod @ 50% psi	Mod @ 100% psi	Mod @ 200% psi	Mod @ 300% psi
Median	1307.2	599.07	121.16	157.08	252.94	394.22
Average	1312.4	601.03	121.77	158.59	257.40	401.81
Range	182.87	22.736	5.593	9.806	21.196	36.647
Std. dev.	97.602	10.580	2.625	4.602	10.077	17.345

Ignore highest & lowest results: Disabled

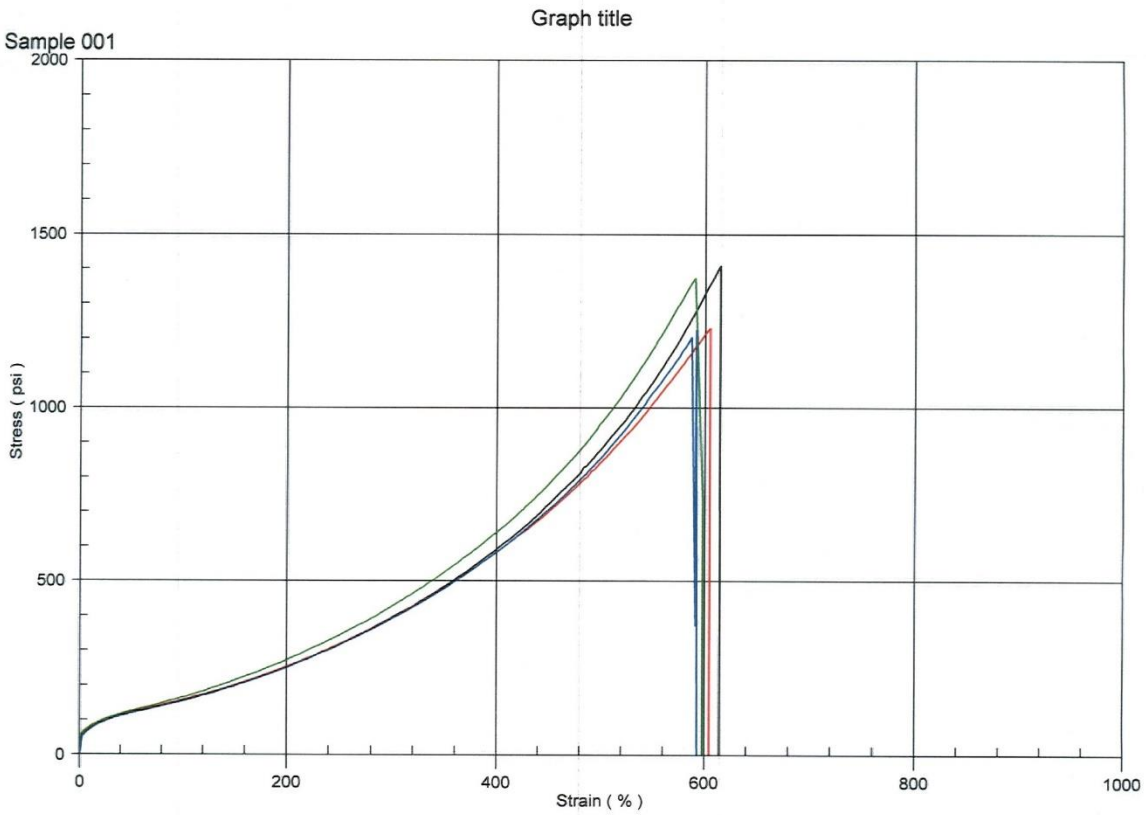

Appendix C: FAA Approved Certification Basis

THIS SECTION INTENTIONALLY EXCLUDED DUE TO PROPRIETARY INFO